2012

Numerical study of downhole heat exchanger concept in geothermal energy extraction from saturated and fractured reservoirs

Yin Feng
Louisiana State University and Agricultural and Mechanical College

NUMERICAL STUDY OF DOWNHOLE HEAT EXCHANGER CONCEPT IN GEOTHERMAL ENERGY EXTRACTION FROM SATURATED AND FRACTURED RESERVOIRS

A Dissertation

Submitted to the Graduate Faculty of the
Louisiana State University and
Agricultural and Mechanical College
in partial fulfillment of the
requirements for the degree of
Doctor of Philosophy

in

The Craft & Hawkins Department of Petroleum Engineering

by
Yin Feng
B.S., Dalian University of Technology, 2004
M.S., University of Louisiana at Lafayette, 2007
August 2012

Acknowledgments

First, I would like to thank my adviser Prof. Mayank Tyagi. In the last four years, he taught me how to become a researcher, provided me with interesting topics and also shared his experience and knowledge with me. I also thank all my committee members: Prof. Christopher D. White, Prof. Juan Lorenzo, Prof. Jeffrey Hanor, Prof. Arash Taleghani and Prof. Shawn Walker, for the valuable discussions and suggestions. I would like to extend thanks to UCoMS, Cactus and Geothermal Groups for both technical and financial support. Finally, I'd like to thank my family and friends for giving me a lot of care, support and help.

Table of Contents

List of Tables

List of Figures

Abstract

Geothermal energy has gained a lot of attention recently due to several favorable aspects such as ubiquitously distributed, renewable, low emission resources while leveraging the advances in the associated technologies such as directional drilling and low enthalpy power generation plant. However, there are still many challenges such as the high initial capital cost of drilling and surface facilities, environmental risk of seismicity due to the induced disequilibrium in the formation, and sustainability of project over designed operational life. Traditional downhole heat exchangers (DHE) could potentially reduce the capital cost and the risk of seismicity, but they are unable to maintain a sustainable geothermal energy production over the operational life due to the rapid cooling down of formation in the vicinity of the wellbore. In this study, a novel DHE design is introduced to enhance the energy production rate as well as sustainability for mainly two types of geothermal reservoirs: saturated geothermal reservoirs and enhanced/engineered geothermal systems (EGS).

Modeling of DHE is based on the concept of thermal resistance. A geothermal reservoir simulator is built reusing components of an existing blackoil simulator by adding thermal energy transport equations and fracture representation (discrete fracture network). Several verification and validation tests are carried out. Parametric studies are presented for various configurations of DHE and thermodynamic analysis is carried out for the binary power plant cycle. In addition, the geothermal reservoirs Camerina A and Raton Basin are presented as case studies for saturated geothermal reservoir and EGS, respectively. In saturated geothermal reservoirs, the performance of DHE is improved significantly by exploiting forced convection. For EGS, the overall heat extraction rate is also enhanced by adding DHE.

Chapter 1
Introduction

1.1 Overview of Geothermal Energy

Geothermal energy is the heat energy stored in the earth. At the beginning of recorded history, it was used only for cooking and bathing. Until 1904 when electricity was first produced from geothermal steam at the Larderello field in Italy, geothermal energy was accepted by various industries for commercial purposes (DiPippo, 2008).

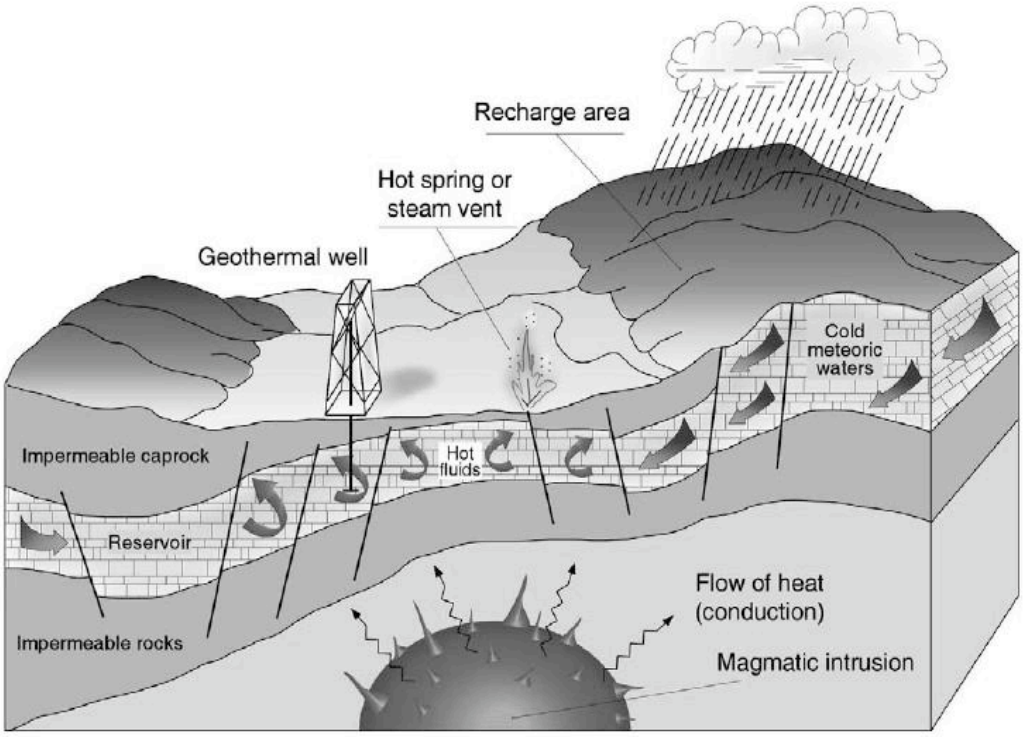

Figure 1.1: Schematic of an ideal hydrothermal reservoir (Barbier, 2002).

Figure 1.1 shows an ideal hydrothermal reservoirs with following five features (Barbier, 2002).

1) A large heat source to ensure that the thermal energy is sufficient to support exploitation over long enough time period to make it economic.

2) A permeable reservoir to ensure that the fluid is able to move and carry thermal energy

from hotter parts of the formation.

3) Sufficient fluid supply to maintain the production of thermal energy from the formation.

4) Isolation provided by the surrounding impervious rock to ensure no loss of geofluids to other formation layers.

5) A reliable recharge mechanism to avoid eventual depletion of reservoir over sustained production period.

Hydrothermal reservoirs are the most common economic geothermal resources and can be classified as water-dominated and vapor-dominated, where the latter one usually conveys a higher energy per unit fluid mass as reported by Barbier (1998) (Figure 1.1). Alternatively, we can drill deeper to impermeable rocks which may contain more heat. By hydraulic fracturing, a fracture network can be generated in the impermeable rocks. The injected working fluid can extract heat while moving through the engineered fracture system. This type of geothermal reservoir is called engineered/enhanced geothermal system (EGS). For a comprehensive review of geothermal energy resources engineering, readers are directed to excellent books by Huenges (2010) and Grant & Bixley (2011)

1.2 Various Geothermal Resources

Based on the presence of geofluid and permeability of the resource, geothermal resources are classified into two categories: Saturated Geothermal Reservoirs and Hot Dry Rock (known as Enhanced Geothermal Systems).

Saturated Geothermal Reservoirs

Previously mentioned hydrothermal reservoir is an example of saturated geothermal reservoirs. However, it also includes geopressured geothermal brines (pressurized aquifers with high temperature and dissolved methane), from which, three forms of energy can be produced (Griggs, 2004).

a. Mechanical energy: high pressure at wellhead can be used to generate electricity.

b. Thermal energy: high temperature fluid can be used in heating, thermal recovery or electricity generation.

c. Chemical energy: this energy comes from burning the dissolved methane gas.

Some of the best known geopressured geothermal reservoirs are located along the northern Gulf of Mexico. During the drilling for oil and gas in the sedimentary coastal areas of Texas and Louisiana, fluids have been encountered with pressures exceeding values compared to hydrostatic and approaching lithostatic. According to Bebout (1981), the weight of the solid overburden doubles the pressure gradient to approach the lithostatic value of 1.0 psi/ft instead of the hydrostatic value 0.465 psi/ft.

Enhanced Geothermal Systems (EGS)/Hot Dry Rock (HDR)

Noting that most of the heat stored in the reservoirs having high temperatures also lack formation fluid and have low permeability, the U.S. Department of Energy defined the concept of EGS to explore geothermal resources in these zones which are also called as HDR. Early on, HDR was not economically successful. With the improvement of technology, this concept tends to be commercially mature (MIT, 2006).

In EGS, because of low permeability and the absence of fluid, hydraulic fracturing must to be carried out to generate a large fractured reservoir. Once the reservoir reaches desired volume and permeability, other wells will be drilled to the reservoir and a closed loop well system is constructed. During production, the cold fluid is pumped down from injector and returns to the surface through producers after picking up heat from the hot reservoir. Figure 1.2 shows the schematic of a conceptual two-well EGS in hot dry rock formation. There are numerous well known HDR projects worldwide, such as Fenton Hill in USA, Hijiori in Japan, and Soultz in France.

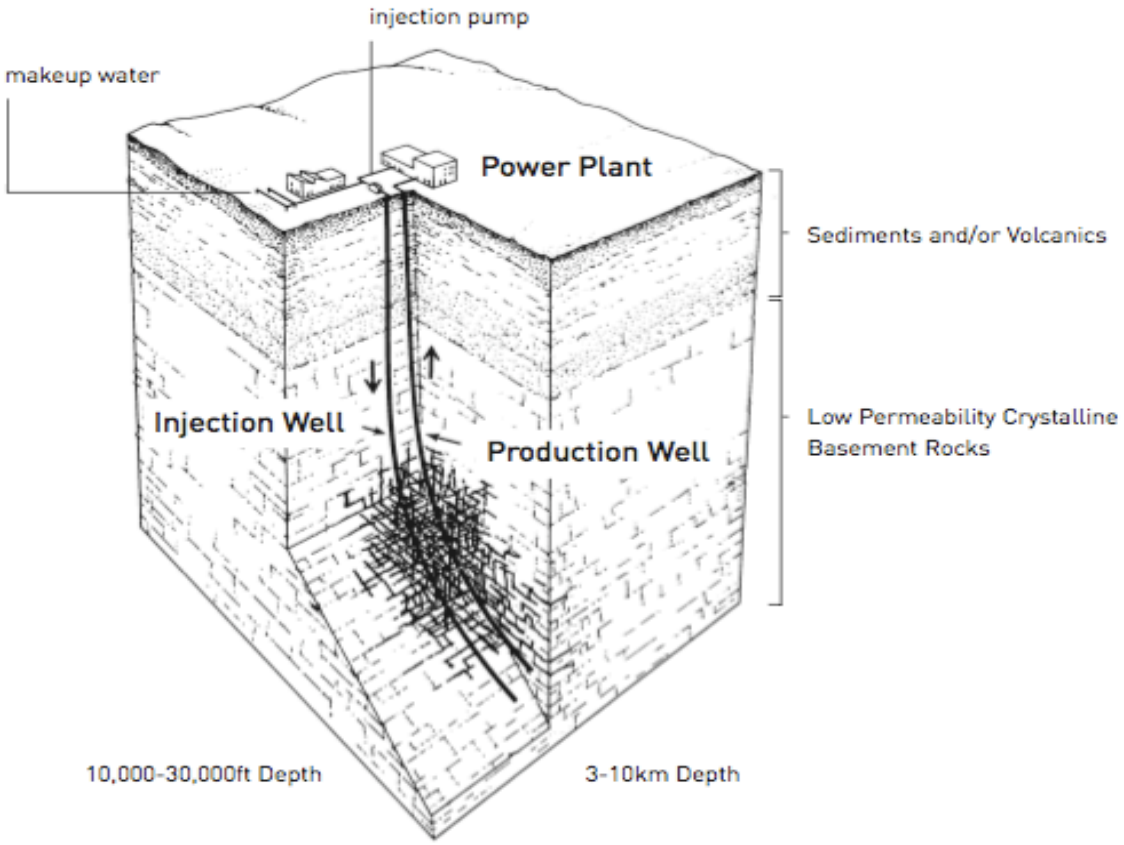

Figure 1.2: Schematic of a two-well EGS with geofluid circulating in a low permeability formation (MIT Report, 2006).

1.3 Attractive Features of Geothermal Energy

Geothermal energy is becoming more and more attractive as a result of following advantages.

Enormous Potential

Since the current technical limit for drilling depth is greater than 10 km, we use the depth of 10 km to define the total geothermal resource base. The table below demonstrates the estimated geothermal energy potential for various resource categories. As indicated in Table 1.1, even for a low thermal to electricity conversion efficiency (5%), 13,000,000 EJ ($1EJ = 10^{18}J$) means 0.18×10^{18}kWh electricity. According to MIT report (2006), the recoverable portion of 13,000,000 EJ is above 200,000 EJ (5.6×10^{16}kWh), above 2,000 times of the U.S. an-

nual energy consumption (2008) and 40,000 times of U.S. residential energy consumption as reported by U.S. Energy Information Administration.

Table 1.1: Estimated U.S. geothermal energy potential to 10km drilling depth (Cutright 2009, MIT 2006).

Category of Resource	**Thermal Energy**	**Equivalent Barrels of Oil**
Hydrothermal	$2.4 \times 10^3 - 9.6 \times 10^3$	$4.13 \times 10^{11} - 1.65 \times 10^{12}$
Co-Produced Fluids	$9.44 \times 10^{-2} - 4.51 \times 10^{-1}$	$1.62 \times 10^7 - 7.76 \times 10^7$
Geopressured Systems	$7.10 \times 10^4 - 1.70 \times 10^5$	$1.22 \times 10^{13} - 2.92 \times 10^{13}$
Enhanced Geothermal Systems	$> 1.3 \times 10^7$	2.23×10^{15}
US Annual Consumption (2008)	94.14	1.81×10^{10}

Renewable

Geothermal energy is also known as a renewable resource. According to Rybach (2007), geothermal extraction is not a "mining" process since the energy produced can be recovered on the time scale similar to that required for energy removal. In contrast, for energy source such as fuel, geological times are needed for the regeneration (Rybach, 1999). As far as today's science can determine, the center of the Earth has been very hot for over 4 billion years and will continue to be hot at least for another 4 billion years in the future (Kagel et al., 2007). The internal heat of the earth is a result of decay of naturally radioactive isotopes at the rate of 860 EJ/yr, about twice the world's primary energy consumption in the year of 2003 (Rybach, 2007).

Availability

Geothermal energy is available 24 hours per day and 365 days per year. In contrast, other renewable energy such as solar and wind are influenced by season and weather.

Low Gas Emission

Geothermal energy is widely described as an environmental friendly energy source, attributed to the negligible gas emission compared to fossil-fueled power. The reduction in nitrogen and

sulfur emissions reduces the risk of acid rain, and low carbon dioxide emissions avoid contributing to global warming (Kagel et al., 2007). The following table demonstrates the carbon dioxide emission for different types of energy sources, from which, we can see the amount of carbon dioxide emission for geothermal energy is much less than that for conventional energy sources.

Table 1.2: Comparison of carbon dioxide emissions (Bloomfield, 2003).

Power Source	CO_2 Emission (lb/kWh)
Geothermal	0.2
Natural gas	1.321
Oil	1.969
Coal	2.095

Economics

To benefit the policy makers and researchers, the levelized cost of energy (LCOE) is accepted as an overall cost estimation accounting for initial capital, operation and maintenance (O&M), performance and fuel cost. Although the initial investment might be high, due to drilling and surface facilities, the levelized cost of electricity is lower for geothermal energy, compared to other resources as shown in Table 1.3. In addition, due to the market with ever increasing oil price, geothermal energy can provide an economic alternative.

Table 1.3: Levelized cost of electricity for various energy sources (Cutright, 2009).

Levelized Cost ($/MWhr)	High Case	Base Case	Low Case
Solar Photovoltaic (crystalline)	$201	$153	$119
Solar Photovoltaic (thin film)	$180	$140	$110
Fuel Cell	$117	$90	$72
Solar Thermal	$126	$90	$69
Coal	$66	$55	$46
Natural Gas	$64	$52	$40
Nuclear	$64	$62	$35
Wind	$61	$43	$29
Geothermal	**$59**	**$36**	**$22**

Leveraging Technologies

According to Cutright (2009), the advances in drilling technology makes a 10km depth possible, so that the hotter geothermal reservoirs are achievable; the advances in hydraulic fracturing allow us extracting heat from hot dry rock reservoirs; the advances in binary cycle heat exchanger make low enthalpy resources (about 100^oC) economical.

1.4 Energy Conversion Systems

Although there are many ways to utilize geothermal energy such as directly heating, thermal recovery for petroleum industries, this study focuses on electricity generation. Therefore, the energy conversion facilities called power plants are necessary. Three types of geothermal power plants are introduced as follows, where, the binary plants for low-moderate temperature resources are involved in this study for detailed description on geothermal power plants, readers are directed to an excellent book by Dipippo (2008).

Dry Steam Power Plants

As the oldest type of geothermal power plant, dry steam plants focus on very hot resources ($> 455^oF(235^oC)$), where, the steam is produced to surface, and drives a steam turbine to generate electricity directly. Then, the output low pressure steam from turbine can be reinjected back to the geothermal reservoir after passing through a condenser to be converted into water (Dipippo, 2008).

Flash Steam Power Plants

The flash steam plant is the most common type of geothermal power plant, currently. This system works for reservoirs with fluid temperature approximate high than $360^oF(182^oC)$. The hot liquid converts into vapor phase while entering flash tank due to a sudden pressure drop. The steam then drives turbine for energy conversion, and the left liquid in the tank may either be flashed again or reinjected back with the liquid after condensing (Boyle, 2004).

Binary Power Plants

Improvement in binary power plant efficiency for low-enthalpy feed, makes it possible to develop geothermal resources with temperature in the range of 200^{o}F to 300^{o}F (93^{o}C to 150^{o}C). In a binary cycle, geothermal fluid (brine) goes through heat exchanger and is reinjected back to the geothermal reservoir. In heat exchanger, the secondary working fluid (n-butane) with a low boiling point is evaporated and the vapor phase working fluid (n-butane) drives the turbine to generate electricity. After that, the vapor will come back to liquid phase in condenser and the loop continues. The binary power plants minimize the gas emission due to the closed loop operation and extend the range of potential geothermal resources (Boyle, 2004).

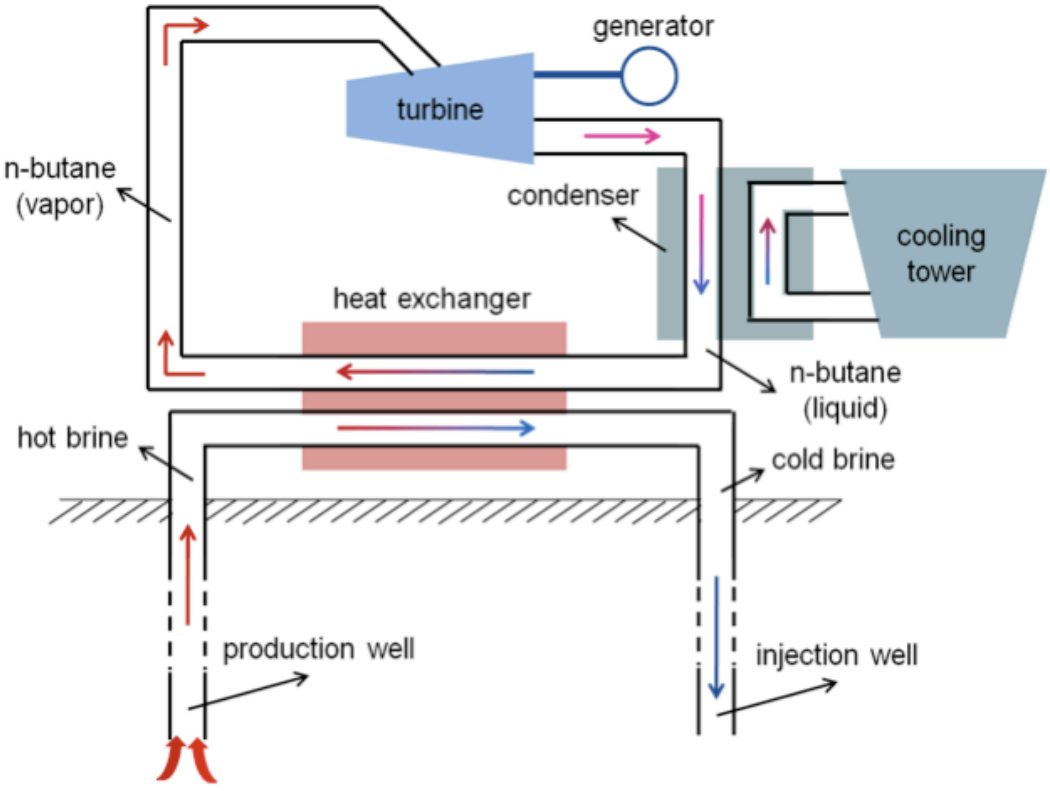

Figure 1.3: Schematic of binary power plants (Adapted from Boyle, 2004).

As seen in Figure 1.3, the heat exchanger is located on the surface for heat exchange between geofluid and working fluid. The concept of downhole heat exchanger would require placing the exchanger in the geothermal reservoirs, and as a result, no amount of geofluid need to be produced and reinjected, to or from surface facilities.

1.5 Challenges for Geothermal Energy Extraction

There are alway challenges. The huge capital investment is one of the major problems. For hydrothermal systems, according to Geothermal Technologies Market Report (2009), the investment can be $3000-$4000 per kW, where, 47% goes to the construction of power plant and 42% is for drilling.

The seismicity or subsidence may be triggered during the operations such as hydraulic fracturing and producing/injecting. The sequential thermal stress is also a potential issue (Majer, 2009). Actually, any operation breaking the equilibrium of geothermal reservoir may result in seismicity or subsidence problems.

The produced brine needs to be injected into shallow disposal wells instead of surface discharge to avoid environmental impact (John, 1998). However, the cost is considerable as estimated in Table 1.4.

Table 1.4: Drilling/completion and operation costs for geofluid disposal (Griggs, 2004).

Flow Rate (bbl/day)	Drilling/Completion Costs ($K)	Operation Costs ($K/year)
10,000	1,000	10
25,000	1,000	25
35,000	1,000	35
50,000	2,000	50
60,000	2,000	60
70,000	3,000	70

The sustainability is critical factor to ensure the success of a geothermal project. Since about one third of the project life is just for offsetting the initial investment, if a project can not sustain to the designated life, the investor may not even earn the capital back. It is more serious for an EGS project as a result of cold fluid injection. The rapid cooling down of EGS reservoir makes it more challenging to maintain sustainability. Therefore, the overall EGS lifetime can be divided into several decade, and the questions becomes how fast the thermal recovery can be, after production stops (Rybach, 2007). It is assumed that most of the energy will be recovered over the timescale similar to production. However, the extended lifetime may not be acceptable by economic interest.

1.6 Improvement in Downhole Heat Exchanger Design

A downhole heat exchanger (DHE) is designed to move the heat extraction process into the geothermal reservoir.

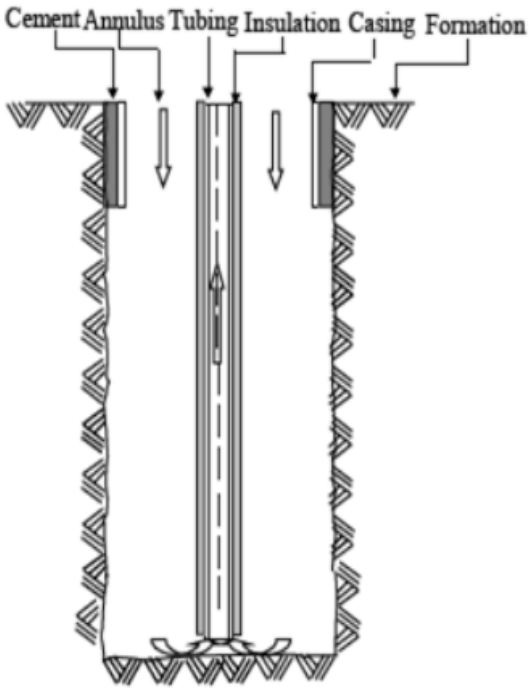

Figure 1.4: Schematic of a convectional downhole heat exchanger (Nalla et al., 2004).

As shown in Figure 1.4, the working fluid is injected through annulus, and returns to wellhead from tubing after being heated. Tubing is insulated to avoid heat loss from the working fluid inside the tubing to the one in the annulus. By applying DHE, geofluid disposal and the related issues can be eliminated. Consequentially, the cost for the disposal well is removed, and as a result of no geofluid withdraw, it may potentially relieve the seismicity and subsidence issues.

However, the mediocre heat extraction performance limits its applications (Nalla et al., 2004). This drawback results from the rapid cooling down in the vicinity of wellbore, and conduction or natural convection (if applicable) cannot bring heat to wellbore efficiently. Therefore, lots of studies were carried out for the purpose of improving the DHE performance.

Alkhasov et al. (2000) presented a borehole heat exchanger with a feature of two counter-circulation (Figure 1.5). This design consists of several parts including tubing, middle annulus (between tubing and insulated inner casing), and outside annulus (between insulated inner casing and outer casing). Thermal water is injected through tubing and the secondary fluid is injected from outside annulus and returns to surface from middle annulus.

There are several studies aiming to improve the performance of DHE by taking advantage of natural convection, such as Wang et al. (2009), who described an implementation of DHE for EGS Reservoirs. The most interesting points in his study are the proposed single-well EGS configuration and a downhole thermosiphon, a device taking advantage of gravity difference between working fluid in annulus and tubing. This design takes advantage of natural convection in fractures to enhance the heat extraction efficiency.

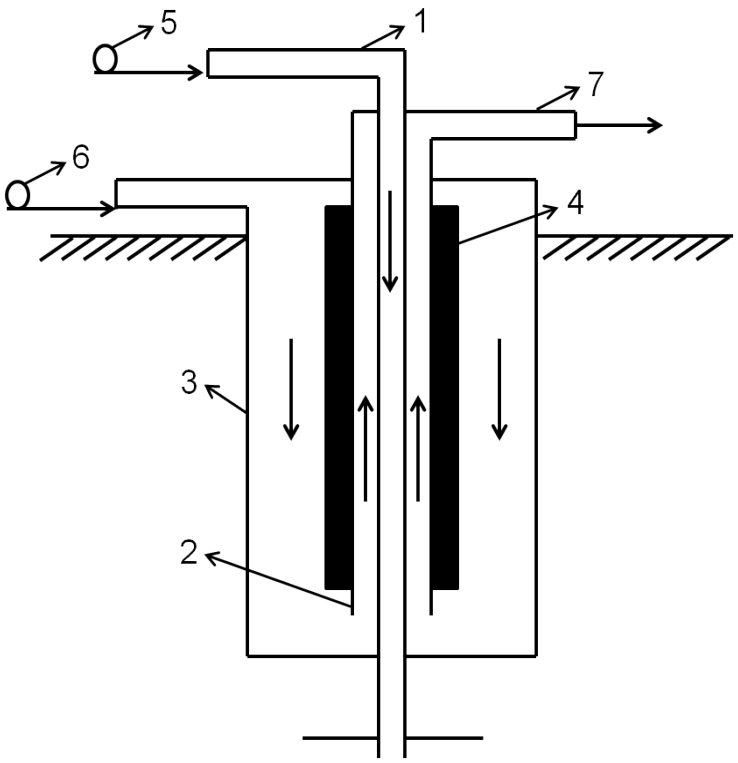

Figure 1.5: Construction of downhole heat exchanger with two counter-circulation system. 1, injection well; 2, inner annulus; 3, outer annulus; 4, insulation; 5, pump for thermal water; 6, pump for working fluid; 7, pipeline for production. (Alkhasov et al., 2000).

1.7 Study Objectives

This study aims to introduce the innovative DHE designs into both saturated and EGS reservoirs to improve the heat extraction efficiency and sustainability. Hypotheses are that 1) the novel DHE for saturated geothermal resources can enhance thermal drainage volume and maintain a sustainable development over project life; 2) the application of DHE in EGS reservoirs can enhance the heat extraction efficiency and sustainability.

Chapter 2
Tools for Geothermal Reservoir Simulation

In this chapter, thermal simulator features for flow and heat transport in hydrothermal reservoirs and HDR will be reviewed. Mathematical models related to this study are introduced and several verification & validation cases are included. For more details on the theory and numerical methods, readers are referred to Kolditz et al. (2012).

2.1 Hydrothermal/HDR Simulators

2.1.1 Hydrothermal Reservoir Simulators

Commercial simulators widely used that can model processes relevant to hydrothermal reservoirs are STAR, TOUGH2 and FEHM.

The simulator "STAR" developed by Maxwell Technologies of San Diego, California has been used in various areas including hydrothermal, natural gas and thermal recovery (Pritchett, 1995).This simulator is designed based on finite difference method and contains features like tracer module, deposition/dissolution, and non-condensible gas. "permeable matrix" option is provided for modeling the pressure and temperature transients between fractures and matrix rock.

The general purpose simulator TOUGH2 is developed at Lawrence Berkeley National Laboratory of the U.S. Department of Energy (DOE) for multi-phase, multi-component fluid and heat flow in porous media and fractures and is currently used in geothermal reservoir simulation, nuclear waste disposal, environmental assessment and remediation, and unsaturated and saturated zone hydrology (Pruess, 2011). An important contribution of TOUGH2 is the Multiple Interactive Continua method (Pruess, 1985) which allows sequential partitioning of

the rock matrix and pressure/temperature transients between matrix rock and injected fluid can be estimated.

FEHM (Finite Element Heat and Mass Transfer) was developed at Los Alamos National Laboratory for hydrothermal, oil and gas reservoirs, nuclear waste isolation and groundwater modeling, as well as for the HDR project at Fenton Hill reservoir (Bower, 1998). The simulator is based on finite element method and concentrates on simulating non-isothermal, multi-phase, multi-component flow in porous media models.

2.1.2 HDR Simulators

Although some hydrothermal simulators can also model complex fracture systems, these simulators have rarely been used in modeling engineered fracture network systems. HDR simulators can handle the dynamic aspects of fractures better. However, HDR simulators may lose certain other features such as multi-phase flow capabilities (Sanyal, 2000). Some of the simulators developed for HDR systems will be introduced in the following sections.

FRACTure was developed based on discrete fracture, finite element method for hydraulic, thermal and mechanical behavior in fractured media (Kohl and Hopkirk, 1995). The simulator describes fluid flow through a permeable matrix rock and discrete fractures. Fracture openings are liked to rock stress. The usage covers a variety of geological areas such as space heating, tracer propagation, non-laminar hydraulic behavior, and heat extraction during aquifer utilization. In addition, it has been employed by Soultz HDR reservoir to simulate flow in a dominant fracture including a turbulent flow model.

GEOTH3D was used in Hihiori, Ogachi, and Fenton Hill reservoirs by taking advantage of microseismic data to determine permeability distribution (Yamamoto et al., 1997). GEOTH3D solves mass and energy transport on the basis of Darcy's Law using the finite difference

method. It uses microseismic data during stimulation to define non-uniform porous media model in proportion to the microseismic intensity. Compared to discrete fracture, porous media models cannot capture the sharp temperature gradients and cooling in fractures.

FRACSIM-3D is a fracture network model which has been applied to Hijiori and Soultz reservoir (Sanyal, 2000). Compared to other simulators, FRACSIM-3D focuses to improve following aspects: 1) fracture shear and dilation; 2) thermoelasticity; and 3) chemical dissolution and precipitation. Thus, it can be used for both stimulation analyses (shear dilation) as well as reservoir operations. In addition, the inclusion of chemical dissolution and deposition reaction aids in getting better estimates of the operational reservoir life.

The finite element method based simulator Geocrack2D/3D was developed at Kansas State University and has been used in Fenton Hill and Hijiori reservoirs (Sanyal, 2000). This simulator is based on discrete fracture approach and fully couples fluid flow, heat transfer and rock mechanics equations in the fracture flow. Fracture aperture is described as a function of stress and fluid flow that is calculated by the laminar flow cubic law.

2.2 Methodology

2.2.1 Building Blocks of a Thermal Reservoir Simulator

Process of developing a geothermal reservoir is similar to that of oil/gas reservoir in many ways, such as producing reservoir fluid to the surface. However, the major difference is that a geothermal project pursues heat as product, instead of the fluid produced which only servers as a medium to carry heat. It is noted that, coupling the energy transport equation is also important in several petroleum engineering applications, such as thermal recovery, thermal cracking, and chemical reactions. It was logical for this research to start with an in-house IMPES (IMplicit Pressure Explicit Saturation) parallel BlackOil simulator (El-Khamra, 2009), and extend it further by including equations of state, energy transport equations, fracture

representation and DHE models. BlackOil simulator is developed inside the problem solving environment called Cactus framework.

Cactus Framework

Cactus is an open source problem solving environment designed for scientists and engineers. Its modular structure easily enables parallel computation across different architectures and collaborative code development between inter disciplinal groups (http://www.cactuscode.org). The name Cactus comes from the software design of a central core ("flesh") that connects to application modules ("thorns") through an extensible interface. Thorns can implement custom developed scientific or engineering applications.

For our parallel BlackOil simulator (El-Khamra, 2009), there are three main thorns:
BlackOilBase: This thorn contains the main grid function definitions and parameters. It accumulates all fundamental and dependent variables, as well as physical parameters into one thorn that other components can inherit from.

IDBlackOil: Inherits the basic grid functions (water/oil saturation, water/oil pressure etc.) from BlackOilBase and initializes those variables.

BlackOilEvolve: This thorn implements the IMPES algorithm to solve the black oil system using three-dimensional Cartesian grids and inheriting the physical variables and shares physical parameters. It makes call to PETSc solver library to solve the corresponding systems of linear algebraic equations.

PETSc

PETSc, is a suite of data structures and routines for the scalable solution of scientific applications modeled by partial differential equations (http://www.mcs.anl.gov/petsc/petsc-as). In the solution loop, pressure equations are solved by calling PETSc libraries.

Queenbee/LONI

The Louisiana Optical Network Initiative (LONI) is a state-of-the-art, fiber optics network that runs throughout Louisiana (http://www.loni.org). Queen Bee, as the core supercomputer of LONI, is a 50.7 TFlops Peak Performance, 668 compute node cluster running Red Hat Enterprise Linux version 4 operating system. Each node contains dual Quad Core Xeon 64-bit processors operating at a core frequency of 2.33 GHz.

See Appendix A for the parallel performance of the simulator.

2.2.2 Heat Transfer in Porous Media

The energy conservation for isotropic porous medium with negligible radiative effects and viscous dissipation, can be written as the following partial differential equations for solid phase and fluid phase, respectively (Nield and Bejan, 1998).

$$(1-\phi)(\rho c)_s \frac{\partial T_s}{\partial t} = (1-\phi)\nabla \cdot (k_s \nabla T_s) + (1-\phi) q_s^{'''} + h(T_f - T_s) \tag{2.1}$$

$$\phi(\rho c)_f \frac{\partial T_f}{\partial t} + (\rho c_p)_f v \cdot \nabla T = \phi \nabla \cdot (k_f \nabla T_f) + \phi q_f^{'''} + h(T_s - T_f) \tag{2.2}$$

where, the subscripts s and f refer to the solid and fluid phases, c is the specific heat of solid, k is thermal conductivity and $q^{'''}$ is the heat production per unit volume, h is a heat transfer conefficient.

For local thermal equilibrium system, it can be further simplified by setting $T_s = T_f = T$, and Eq. (2.1) plus Eq. (2.2) gives:

$$(\rho c)_m \frac{\partial T}{\partial t} + (\rho c_p)_f v \cdot \nabla T = \nabla \cdot (k_m \nabla T) + q'''_m \tag{2.3}$$

where,

$$(\rho c)_m = (1-\phi)(\rho c)_s + \phi(\rho c)_f \tag{2.4}$$

$$k_m = (1-\phi)k_s + \phi k_f \tag{2.5}$$

$$q'''_m = (1-\phi)q'''_s + \phi q'''_f \tag{2.6}$$

In this study, velocities at the six faces in a control volume are calculated from flowing equations, and then, the energy equation is solved explicitly.

Following equations describe density changes with temperature and pressure approximately. However, there are more detailed correlations available for brine properties for a range of conditions, such as Rowe & Chou (1970), McCain (1991), and Batzle & Wang (1992).

$$\rho_f = \rho_{ref}[1 - \beta(T - T_{ref})] \tag{2.7}$$

$$\rho_f = \rho_{ref}[1 - C(P - P_{ref})] \tag{2.8}$$

where, β and C represent thermal expansion coefficient and compressibility, respectively.

2.2.3 Fracture Representation

According to Bear (1993), the flow in fracture is typically modeled by three methods: Single Continuum Model, Dual Continuum Model, and Discrete Fracture Network (DFN).

Single Continuum Model

This model considers flow and transport only in the open, connected fractures of the rock mass. Pruess et al. (1986) presented a model for a single equivalent model in unsaturated fractured rock in which hydraulic conductivity was taken as a sum of hydraulic conductivity from the porous media and the fracture. Pruess et al. (1990) found that this approach

was unacceptable in the presence of rapid flow transients, large fracture spacings, or with a very low permeability rock matrix. Svensson (2001) proposed and evaluated a method to represent fracture network as grid cell conductivities in a continuum model. The method was developed for a sparsely fractured rock with a conductivity field that is dominated by major fractures and fracture zones.

Dual Continuum Model

The dual continuum model was proposed by Barenblatt et al. (1960) and later extened by Warren and Root (1963). This approach models the fractured rock as two overlapping continua in a hydraulic interaction, where a matrix accounts for most of the porosity (storage), but little of the permeability, and a highly permeable fracture continuum with negligible storage. Fluid flows along the fracture system and the matrix only has fluid flow at the interface with fracture system. For the scale where discrete fracture is not efficient, this method could model fractures without a complex geometry and a hugh number of gridblocks. However, it cannot accurately predict the flow pathway, as a result of explicit description of the fractures' geometries.

Kazemi et al. (1976) and Rossen (1977) extended Warren and Root's work to two-phase flow. This model can account for relative permeability, gravity, imbibition, and variation in formation propertires. Thomas et al. (1983) developed a three-phase version of the dual porosity model to simulate the flow of water, oil, and gas in fractured systems. Ray et al. (1996) developed a two dimensional model to describe water flow and reactive chemical transport in spatially-variable macroporous media. Dershowitz et al. (2000) combined a discrete fracture network model with a dual porosity concept to account for the matrix contribution. Karimi-Frad et al. (2006) developed an upscaling technique to construct generalized dual porosity models from detailed fracture characterizations.

Discrete Fracture Network

Discrete Fracture Network models are based on the assumption that fluid flow behavior can be predicted from fracture geometry and transmissivity data. Witherspoon et al. (1980) disscussed the validity of cubic law for fluid flow in a deformable rock fracture. Barbosa (1990) investigated the discontinuous characteristic of water flow through rock masses based on the discrete fracture concept and proposed a hydro-mechanical model. Karimi-Frad (2004) presented a simplified discrete fracture model using unstructured control volume finite-difference technique. The model handles fracture-fracture, matrix-fracture, and matrix-matrix connections. McClure and Horne (2010) described an investigation on the factors that affect the way that the stimulation propagates through formation, in which, complex discretized networks were generated stochastically. Juliusson and Horne (2010) carried out a simulation study of tracer and thermal transport in fractured geothermal reservoirs.

In this study, DFN method is employed and the fractures in the 3-D domain are represented as a 2-D planes with certain aperture widths. This section focuses on the implementation of DFN in a rock matrix. The numerical schemes and methods for solving energy conservation are similar to flow equations, especially, for EGS/HDR reservoir, where the heat transfer in matrix is dominated by conduction. Mathematical descriptions of fracture-fracture and matrix-fracture connections are introduced as follows.

Fracture-Fracture Connection

The fracture network consists of serial fractures which can be further divided into a number of elements. Since the connectivity of each element in a fracture network can not be described using logical index, connectivity list is required for seeking neighboring elements. By applying

material balance to each element, a system of equations can be obtained as Eq. (2.9).

$$\begin{aligned}
&\sum_{j=1}^{N_{neighbor}} T_{ij}(P_i - P_j) = 0, i = 1 \\
&\sum_{j=1}^{N_{neighbor}} T_{ij}(P_i - P_j) = 0, i = 2 \\
&\cdots\cdots\cdots \\
&\sum_{j=1}^{N_{neighbor}} T_{ij}(P_i - P_j) = 0, i = N_{element}
\end{aligned} \tag{2.9}$$

where, T is transmissibility at the face of each element, i and j are element and neighbor index, respectively, $N_{element}$ and $N_{neighbor}$ represent total element number and number of neighbors for each element.

Transmissibility is determined by rock properties, fluid properties and geometry which can be written as $T_G \times (\frac{k_r}{\mu})$, where the mobility term $(\frac{k_r}{\mu})$ is evaluated on upstream scheme. As shown in Figure 2.1, an intermediate control volume (C_0) is introduced into system for flow redirection. The volume is very small compared to the adjacent control volumes. As a result, computational effort enhances due to more unknowns and smaller size. Hence, the star-delta transformation proposed by Karimi-Fard (2004) is employed to account for the control volume at the fracture intersection implicitly.

$$T_{G12} = \frac{\alpha_1 \alpha_2}{\alpha_1 + \alpha_2}, \text{with } \alpha_i = \frac{A_i k_i}{||\overrightarrow{d_i}||} \tag{2.10}$$

The above equation can be extended into multiple intersecting fractures using star-delta transformation and further generalized following correlation for intersection of n-connected control volumes:

$$T_{Gij} = \frac{\alpha_i \alpha_j}{\sum_{k=1}^{n} \alpha_k} \tag{2.11}$$

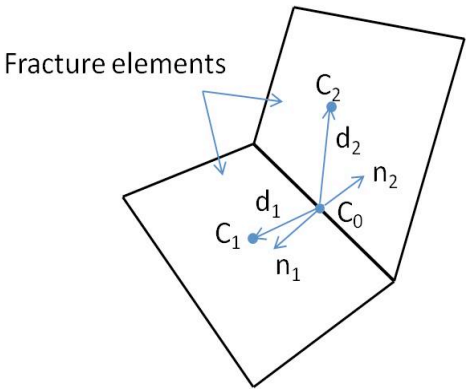

Figure 2.1: Schematic of fracture element connection in DFN (Adapted from Karimi-Fard, 2004).

Matrix-Fracture Connection

Matrix gridblocks connected to fractures contribute more neighbor elements for each fracture control volume. The corresponding mass balance equation for each fracture element i is evaluated as:

$$\sum_{j=1}^{N_{neighbor}} T_{ij}(P_i - P_j) + T_{mf1}(P_i - P_{m1}) + T_{mf2}(P_i - P_{m2}) = 0 \tag{2.12}$$

where, T_{mf} is the transmissibility between matrix and fracture, which is assumed to be the harmonic mean of the fracture-fracture transmissibility (T_{ff}) and matrix-matrix transmissibility (T_{mm}). However, due to the fact that $T_{ff} >> T_{mm}$, we have $T_{mf} \approx T_{mm}$.

To make this fracture representation on a structured mesh system as required by Cactus framework, a treatment is used for the inclined fracture representation. Li and Lee (2008) extended the approach proposed by Lee et al. (2001) and presented a method to calculate transport parameters between fracture network and porous medium within each gridblock. Similar to the definition of wellbore productivity index (PI) (Peaceman, 1978), the concept

of transport index (TI) is used and thus, Eq. 2.12 is organized as (Li and Lee, 2008):

$$\sum_{j=1}^{N_{neighbor}} T_{ij}(P_i - P_j) \quad + \quad TI(P_i - P_{mi}) = 0 \tag{2.13}$$

where, index i, j and mi indicate fracture elements, neighbors and matrix gridblock containing element i, respectively.

Under the assumption of linearly distributed pressure around a fracture, the procedure to calculate transport index between matrix and fracture is proposed as:

Average normal distance from fracture: $\langle d \rangle = \frac{\int x \cdot n dS}{S}$

Flux from matrix to fracture: $q_{mf} = \frac{Akk_r}{\mu}(\frac{(P_{mi}-P_i)n \cdot n}{<d>})$

Transport Index: $TI = \frac{Akk_r}{\mu <d>}$

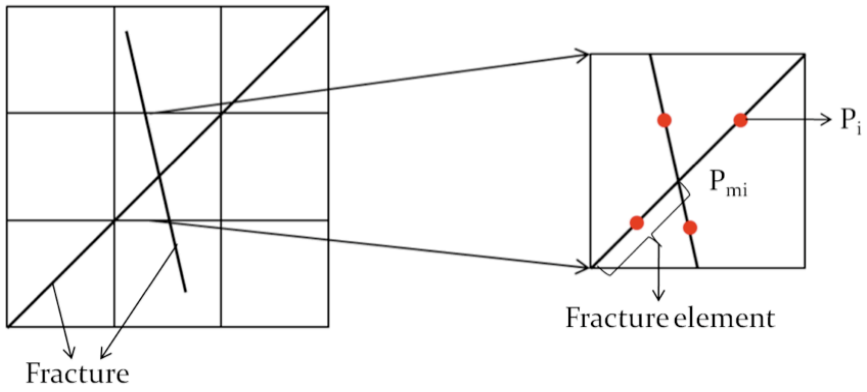

Figure 2.2: Sketch of a gridblock containing parts of two intersecting fractures.

Figure 2.2 describes the discretization of two connected fractures. The dot represents each fracture element in a certain gridblock. From this figure, we can see that for each fracture element, there is one corresponding gridblock. However, for a given gridblock, the amount of fracture elements contained can be none or multiple. In another words, the gridblock is effected by multiply fracture elements and superposition technique is taken for equation assembling.

2.2.4 Coupling with IMPES Method

IMPES (Implicit Pressure Explicit Saturation) is a standard method for solving the coupled two phase flow equation by separating the calculation of pressure and saturation with couple of advantages such as simple to set, efficient to implement and less computational effort. In this study, the two point flux approximation is used to solve pressure implicitly, which results in the following form of the system of equations.

$$AP = R \tag{2.14}$$

where, A stands for the coefficient matrix with transmissibility; P is the matrix and fracture pressure for solving; R is right hand side source term.

Figure 2.3 shows the matrix structure for Eq. (2.14). A_{mm} and A_{ff} represent transmissibility for matrix gridblock and fracture elements. A_{mf} and A_{ff}^T are transmissibility at matrix-fracture interface.

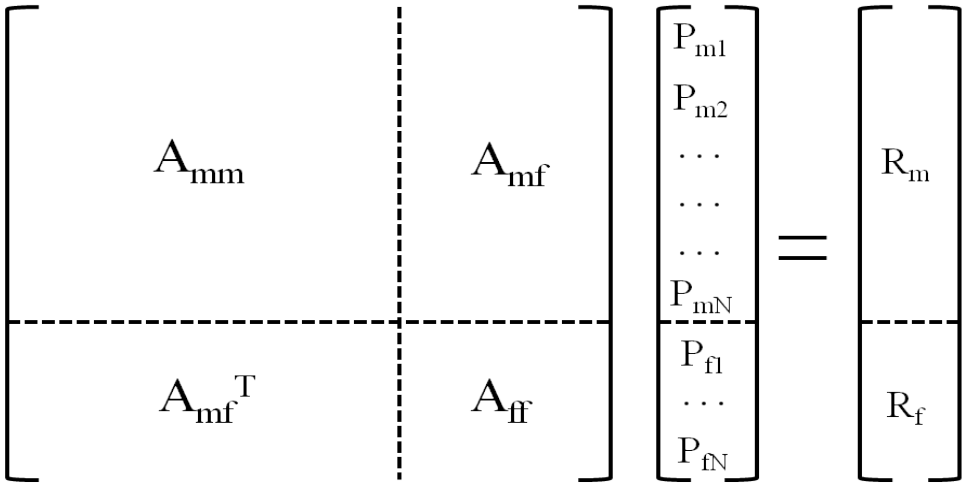

Figure 2.3: Matrix structure of Eq. (2.14) where subscripts m and f stand for matrix and fracture, respectively.

2.3 Verification and Validation Cases

Several verification and validation cases are conducted to qualify the predictive capacity of the geothermal simulator,by solving the relevant processes including natural convection and waterflooding in fractured porous media and comparing against published results.

2.3.1 Convection in Porous Media

Natural convection is a mode of heat transport in which the fluid motion is generated only by density differences due to temperature gradients. In natural convection, fluid surrounding a heat source receives heat, becomes less dense and rises. The surrounding cooler fluid then moves to replace it. This cooler fluid can then gain heat and this cyclic process can continue.

The ratio of the natural convection to the conduction is given by a dimensionless group, Rayleigh number ($Ra = \frac{\rho g \beta x^3 (\Delta T)}{\mu \alpha_m}$). In porous media, the Rayleigh number expression also accounts for the medium permeability and is also known as the Rayleigh-Darcy number ($Ra_D = \frac{\rho g \beta K H (\Delta T)}{\mu \alpha_m}$ where the thermal diffusivity $\alpha = \frac{k_m}{(\rho c_p)_f}$, K is permeability, H is characteristic length, ρ is density and β represents thermal expansion coefficient).

From dimensionless Darcy's equation (Eq. (2.15)), we can see Rayleigh-Darcy number is involved in the gravity term.

$$u + \nabla P = Ra_D \theta e \tag{2.15}$$

where, u, P, θ stand for dimensionless velocity, pressure and temperature. e is the unit vector in the gravity direction.

Case I: Uniform Heated Wall (Costa, 2006)

In the first case, left boundary is maintained at a high temperature and right boundary at a low temperature (Figure 2.4a). Top and bottom boundaries are insulated. Figure 2.4b presents the results on temperature profile left and velocity field (right) for $Ra_D = 100$. The

comparison of the isotherms as well as streamline between presented results and Costa's results is satisfactory.

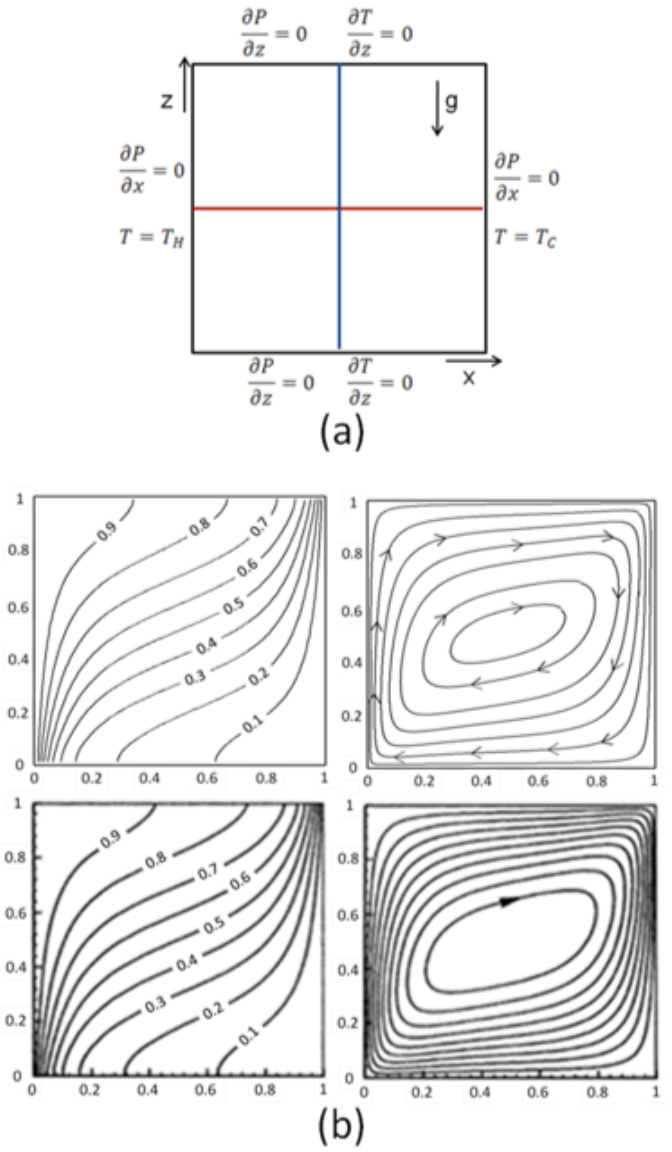

Figure 2.4: (a) Schematic of boundary conditions for Case I (Costa, 2006): left and right boundaries are subject to constant high and low temperature, respectively; (b) Comparison results on isotherms (left) and streamlines (right) [top row: this study; bottom row: Costa (2006)].

To present the comparison results, quantitively, Figure 2.5a and Figure 2.5b show the dimensionless temperature profiles along horizontal (red) and vertical (blue) centerlines (as

shown in Figure 2.4a). The Costa's results are plotted as dots in Figure 2.5 which present an excellent agreement with the simulation results in this study.

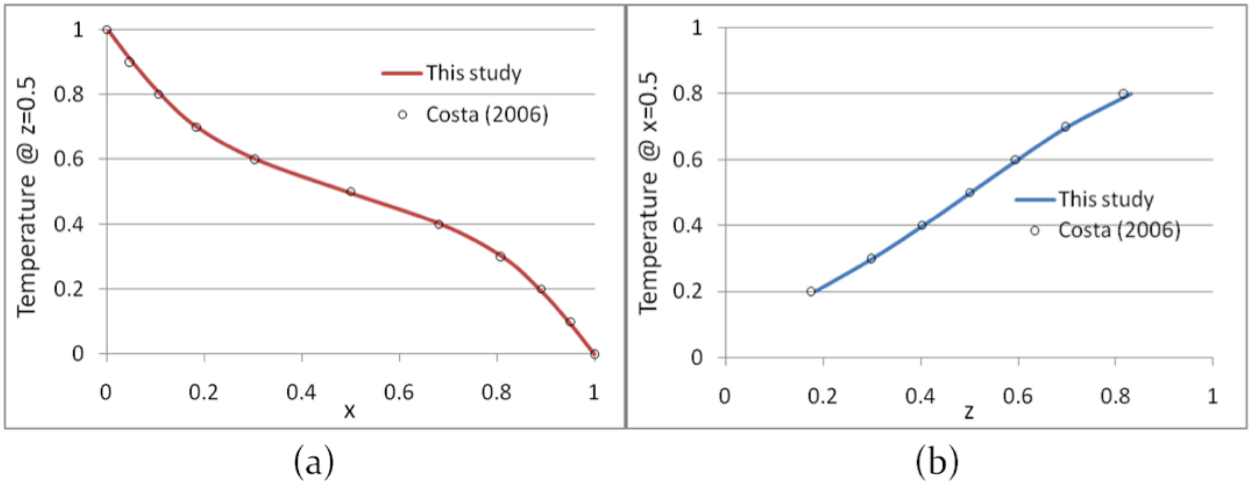

Figure 2.5: (a) Temperature profile along horizontal centerline (z=0.5); (b) Temperature profile along vertical centerline (x=0.5).

Case II: Linearly Heated Wall (Sathiyamoorthy et al., 2007)

In the second case, the bottom wall is uniformly heated with a constant temperature, the right wall is maintained at a lower temperature, the top wall is adiabatic and the left wall is linearly heated (Figure 2.6a). Figure 2.6b displays the comparison of results in this study to Sathiyamoorthy et al. (2007) with $Ra_D = 100$ and the corresponding quantitive comparison is shown in Figure 2.7. Actually, solving a problem with linearly heated wall is meaningful, because this boundary condition just reflects the concept of thermal gradient for a realistic geothermal model.

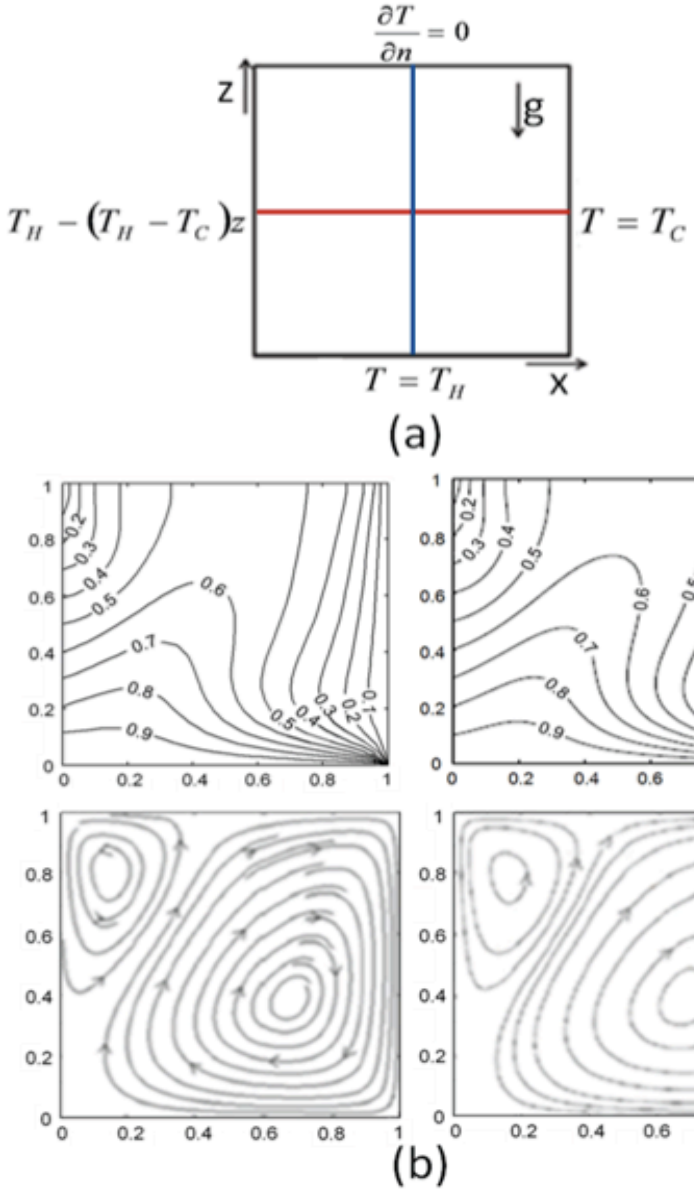

Figure 2.6: (a) Schematic of boundary conditions for Case II (Sathiyamoorthy et al., 2007) (b) Comparison of isotherms (top) and streamline (bottom) [left column: this study; right column: Sathiyamoorthy et al. (2007)].

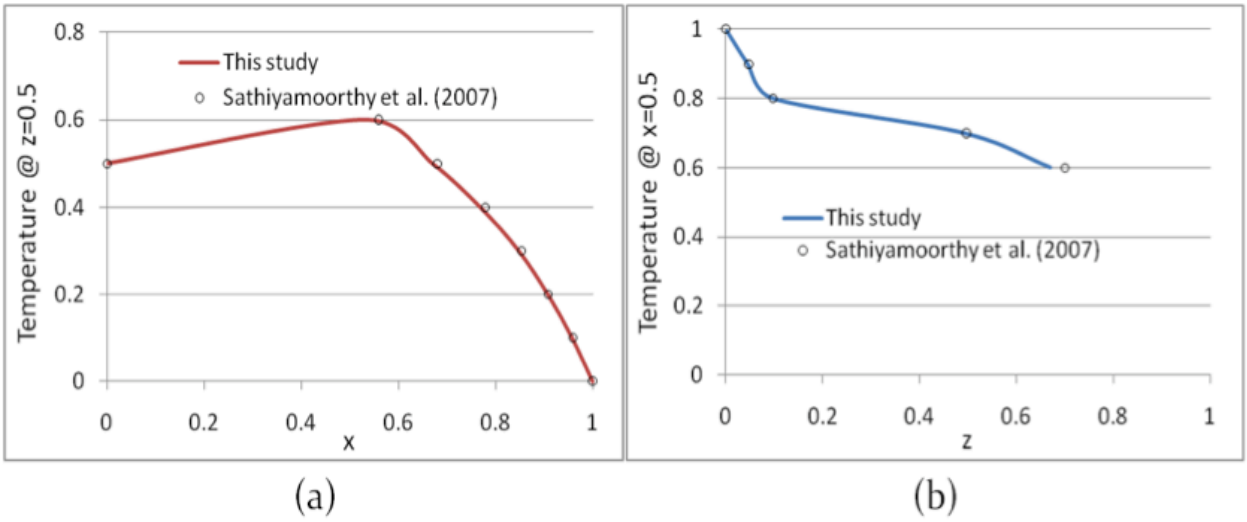

Figure 2.7: (a) Temperature profile along horizontal centerline (z=0.5); (b) Temperature profile along vertical centerline (x=0.5).

Case III: Dipping System (Baez and Nicolas, 2007)

The third case presents the natural convection phenomena in dipping systems with boundary conditions illustrated in Figure 2.8.

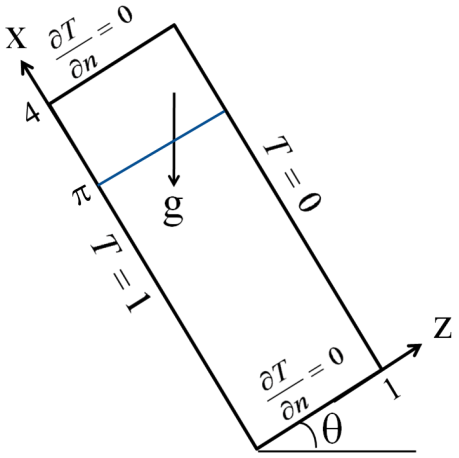

Figure 2.8: Boundary conditions for a dipping system.

Figure 2.9 indicates the comparison of this study to Baez and Nicolas's results where $Ra_D = 100$ with various dip angles. In this case, the temperature profile is along a straight line ($x = \pi$) with resultant plots shown in Figure 2.10.

For a realistic geothermal model, a wide range of dip angles may dramatically affect temperature pattern and overall heat extraction efficiency. The comparison results demonstrate the excellent capacity of the geothermal simulator in solving mass and heat transport in dipping systems.

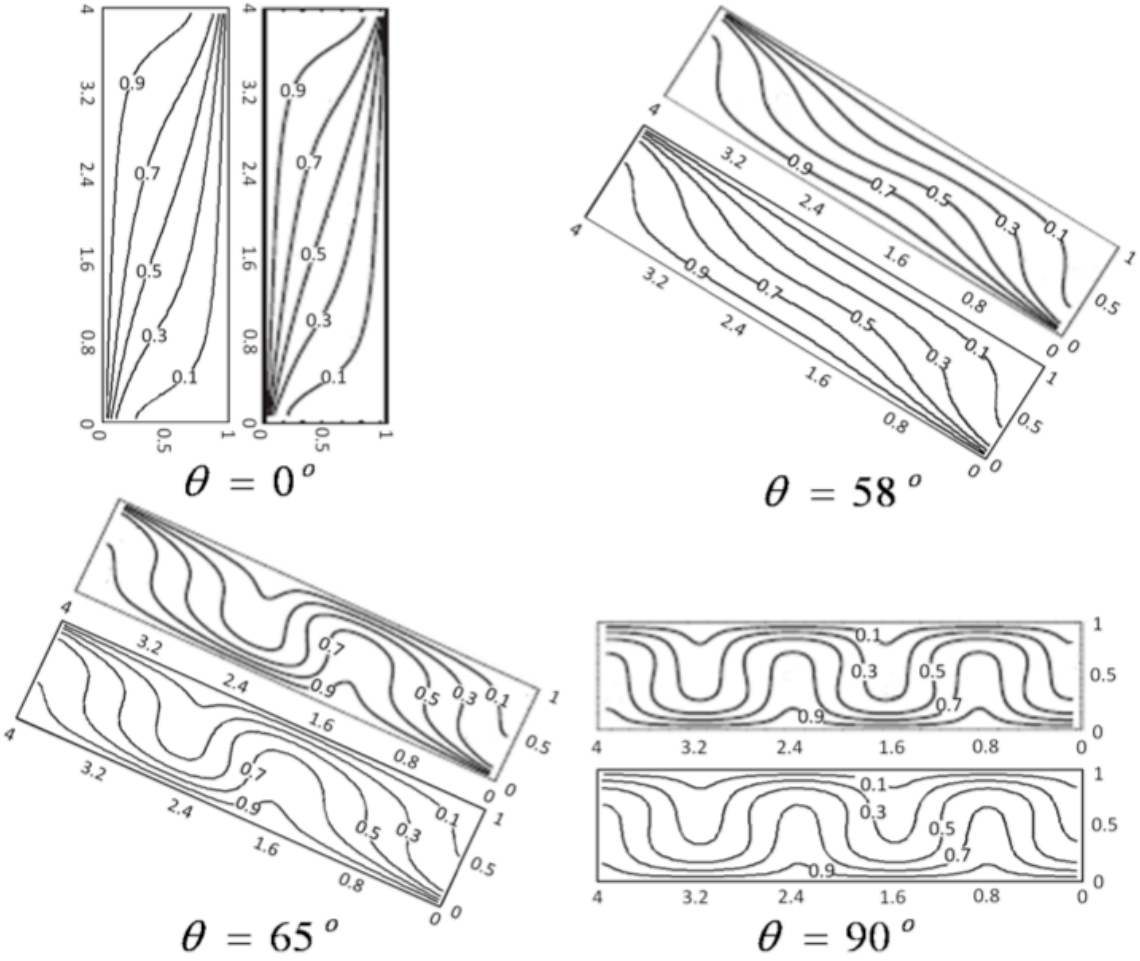

Figure 2.9: Comparison of isotherms at various dip angles [left/bottom: this study; right/top: Baez and Nicolas (2007)].

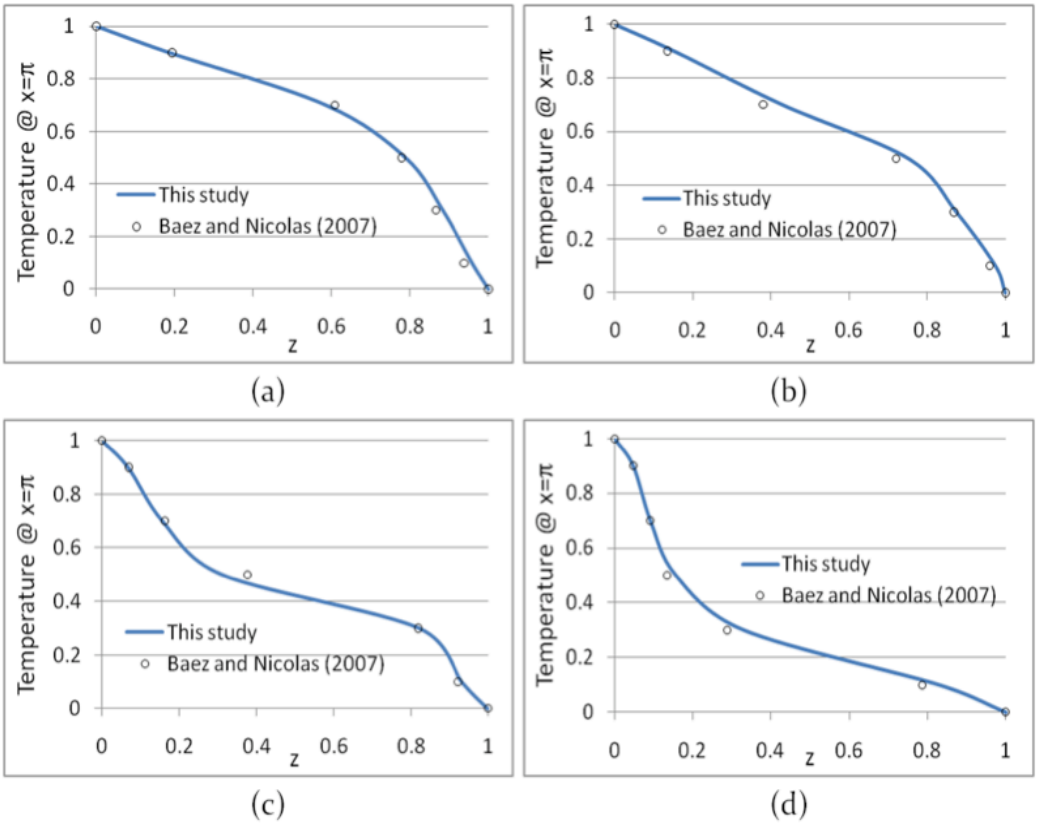

Figure 2.10: Temperature profiles along $x = \pi$ with various dip angles: (a) 0^o; (b) 58^o; (c) 65^o; (d) 90^o

2.3.2 Fracture Network Modeling

Two waterflooding cases are included here, one for single fracture at variable orientations and the other for fracture network connection.

Case I: Single fracture at variable orientations

In this case, the verification and validation are tested by comparing with the results presented by Karimi-Fard (2003). In the system, a singe fracture in the matrix block is considered. Waterflooding simulation is carried out for three various fracture orientations. The aperture and length of fracture are 0.1 mm and 0.9 m, respectively. The porosity and permeability of the matrix are 20% and 1 md, respectively. The system is initially saturated with oil and water is injected from the bottom left corner at a rate of 0.01 PV/D. Liquid is produced

from the top right corner. A linear variation of relative permeability is specified and capillary pressure is assumed to be negligible. The comparison results with different orientations for a single fracture to Karimi-Fard et at. (2003) are shown in Figure 2.11.

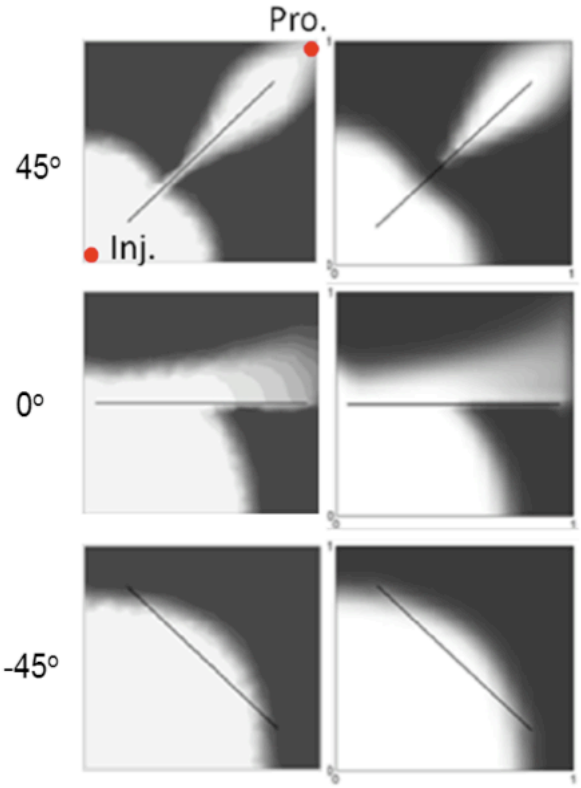

Figure 2.11: Comparison of computed results (right column) with Karimi-Fard et al. (2003) (left column) for different fracture orientations [from top row to bottom row: 45^o, 0^o, -45^o].

As seen in the figure, the comparison presents a satisfactory result. The orientation of fracture dramatically alter the saturation pattern for an invading phase. In the first row of Figure 2.11, water approaches producer rapidly, since the fracture is parallel to the direction of water front moving. The opposite phenomena is observed in last row of Figure 2.11, where, fracture does not affect flow pattern, since the fracture orientation is perpendicular to the direction of displacement.

Case II: Simple fracture network

In this case, the calculation is validated by comparing with the results presented by Karimi-Fard (2004). The system is set up as a simple fractured block containing horizontal and vertical fractures (Figure 2.12). Other properties are the same as in Case I.

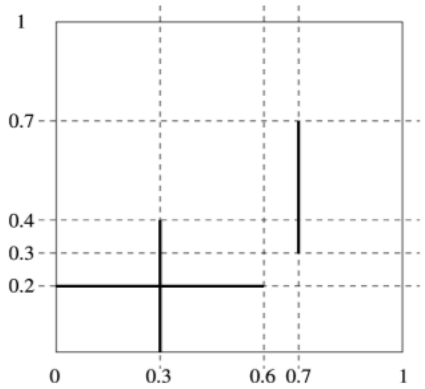

Figure 2.12: Sketch of fracture geometry for Case II (Karimi-Fard, 2004).

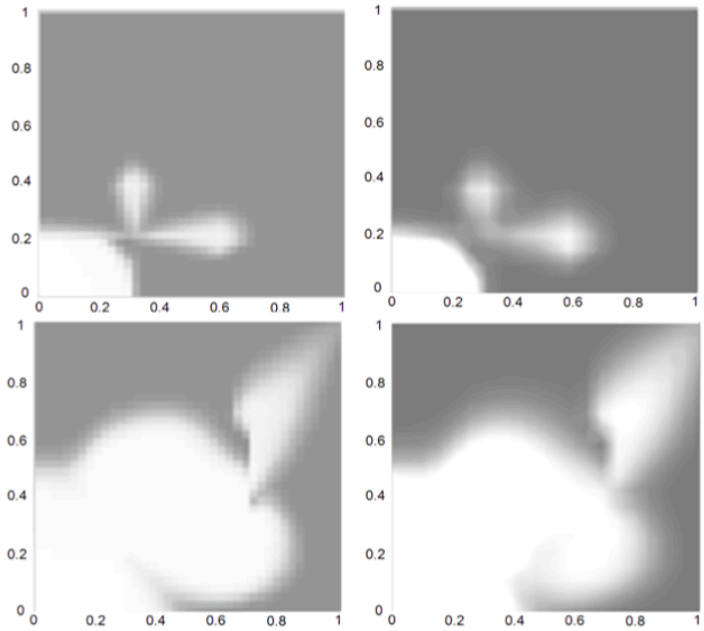

Figure 2.13: Comparison of computed results (right column) with Karimi-Fard et al. (2004) (left column) for various injected volumes [top row: PV=0.1; bottom row: PV=0.5].

The comparative results are presented in Figure 2.13. For the water injection amount of 0.1 PV, the invading phase water reaches the horizontal and one vertical fractures. Most of the injected water flows along fractures and comes back to porous media from the other ends. As the injection of water (PV=0.5), the water front reaches the producer through the third vertical fracture.

Chapter 3
Downhole Heat Exchanger (DHE)

As discussed on section 1.6, the early attempts of the DHE for geothermal energy extraction is not economical (Nalla et al., 2004). Noting the recent advances in directional drilling and well completion technologies, we propose a novel DHE design in this study. The horizontal wells can allow exchanging heat specifically at the bottomhole temperature zone of geothermal reservoir. Innovative completion techniques make a coaxial DHE possible in a horizontal section, and eventually allow the advantages of force convection inside the DHE driven by a a downhole pump.

As shown in Figure 3.1, a deviated wellbore penetrates impermeable rocks and stays within the permeable target layer. The coaxial DHE is placed inside the horizontal section wellbore which is made up of three fluid pathways (known as inside the tubing, outer annulus and inner annulus), where, two pathways provide for working fluid circulation and the third one provides for the flow of geofluid.

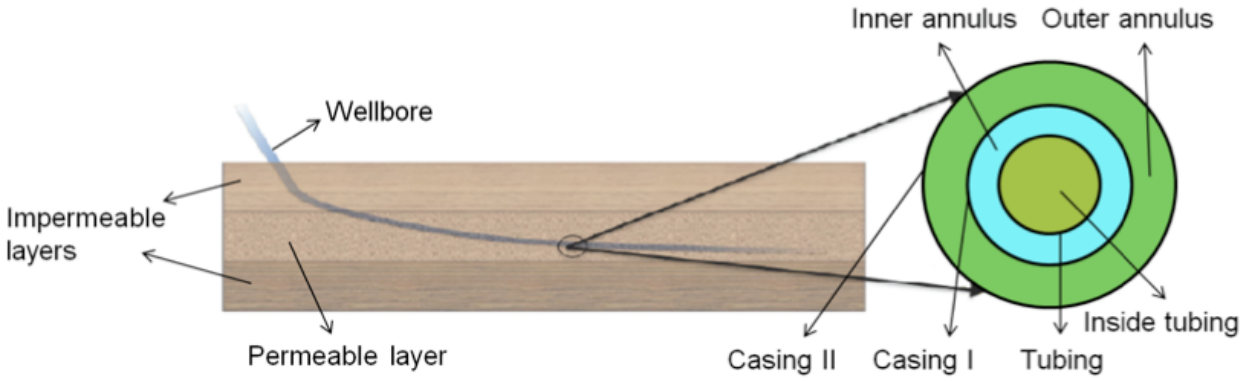

Figure 3.1: Schematic of wellbore paths and DHE cross-section (Tyagi and White, 2010).

DHE can be operated in following two configurations (Figure 3.2). In the first configuration, geofluid (brine) is injected through tubing (known as GFT) and in the second configuration,

working fluid (n-butane) is injected through tubing (known as WFT). Return path for working fluid is insulated in order to maximize the heat gained by the fluid. Brine is reinjected into further away location from the heat exchanger using a downhole pump to the DHE end.

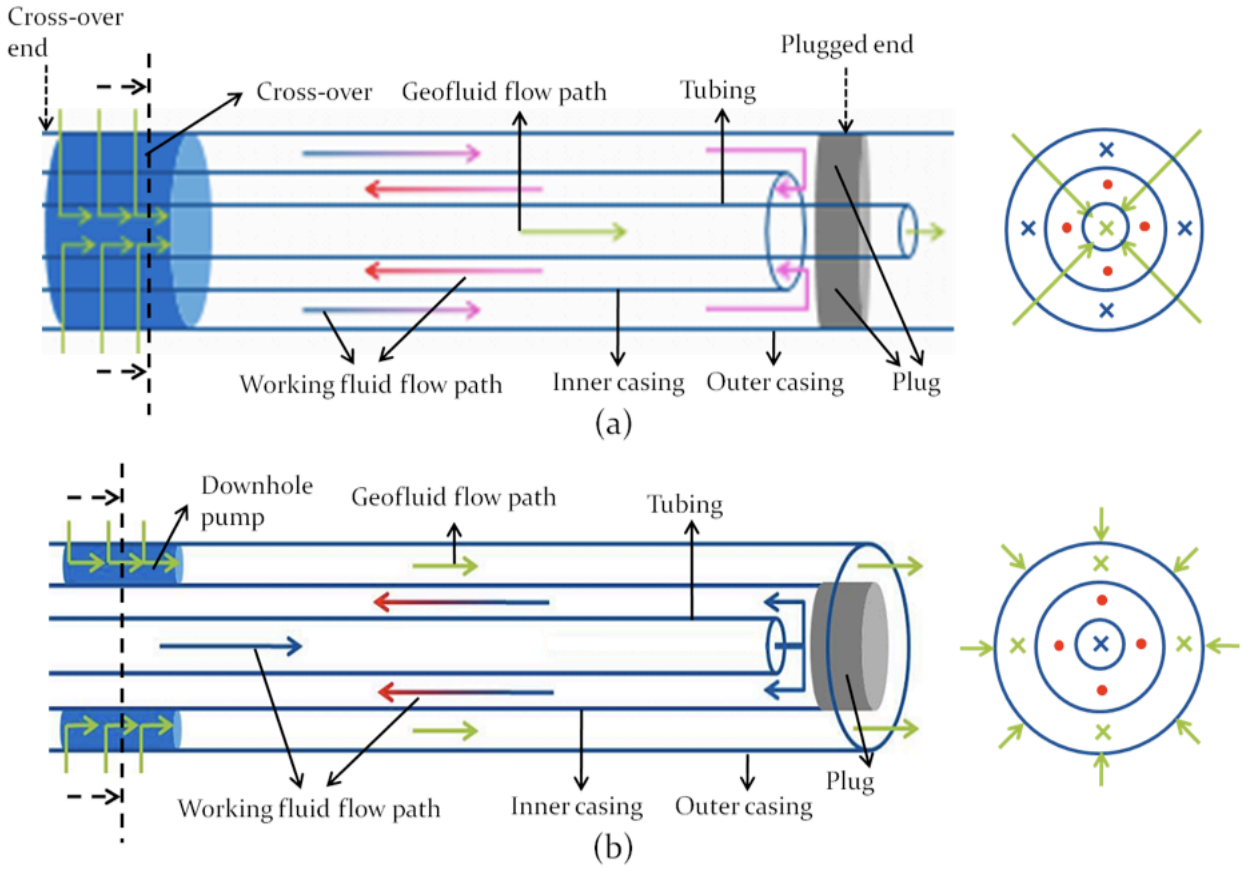

Figure 3.2: Schematics of two configurations for the DHE: a) GFT and b) WFT.

Configuration I (GFT)

As shown in Figure 3.2a, the geofluid (brine) enters tubing through a cross-over from one end of DHE and is reinjected into geothermal reservoir further away from DHE (plugged end).

Radial holes on the cross-over (Figure 3.3) allow for the geofluid to be produced from the formation and enter into the tubing while keeping it insulated from the working fluid flow path. The axial holes at different radial locations create a connected flow path for the working fluid within the coaxial casings (plugged at the end of DHE).

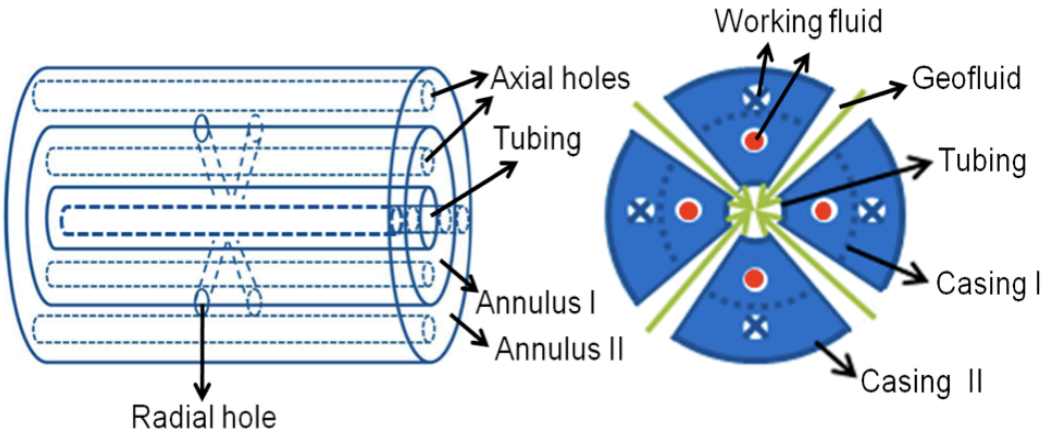

Figure 3.3: Schematic of a cross-over to provide radial/axial distribution of fluid in different flow paths of DHE.

Working fluid (n-butane) is injected through Annulus II and gains heat from the formation. During its return path along Annulus I, the working fluid is heated by the brine inside tubing. In order to avoid heat loss from the working fluid in Annulus I, the Casing I should be insulated.

Assuming convection dominated heat transfer inside tubing and annulus, the simplified governing equations for the energy balance can be summarized as following:

Tubing:

$$A_t \rho_{gf} c_{gf} \frac{\partial T_t}{\partial t} = \frac{T_{a1} - T_t}{R_{at}} - c_{gf} \dot{m}_{gf} \frac{\partial T_t}{\partial x} \tag{3.1}$$

Annulus I:

$$A_{a1} \rho_{wf} c_{wf} \frac{\partial T_{a1}}{\partial t} = \frac{T_{a2} - T_{a1}}{R_{aa}} + \frac{T_t - T_{a1}}{R_{at}} + c_{wf} \dot{m}_{wf} \frac{dT_{a1}}{dx} \tag{3.2}$$

Annulus II:

$$A_{a2} \rho_{wf} c_{wf} \frac{\partial T_{a2}}{\partial t} = \frac{T_e - T_{a2}}{R_{fa}} + \frac{T_{a1} - T_{a2}}{R_{aa}} - c_{wf} \dot{m}_{wf} \frac{dT_{a2}}{dx} \tag{3.3}$$

where, T, c, $\dot{m}$, R, A and ρ stand for temperature, specific thermal capacity, mass flow rate, thermal resistance, cross-section area, and density. The subscripts gf, wf, t, a1, and a2 represent geofluid, working fluid, tubing, annulus I and annulus II, respectively. The definitions of R_{fa} R_{aa} and R_{at} are shown in next section.

Analytical solution is derived under the following assumptions: (1) Perfect insulation of casing I; (2) steady state flow conditions (3) constant average thermal properties; (4). constant reservoir temperature T_e. For steady state, Eqs. (3.1) - (3.3) can be further simplified as:

Tubing:

$$T_{a1} = c_{gf}\dot{m}_{gf}R_{at}\frac{dT_t}{dx} + T_t \tag{3.4}$$

Annulus I:

$$c_{wf}\dot{m}_{wf}\frac{dT_{a1}}{dx} = \frac{T_{a1} - T_t}{R_{at}} \tag{3.5}$$

Annulus II:

$$c_{wf}\dot{m}_{wf}\frac{dT_{a2}}{dx} = \frac{T_e - T_{a2}}{R_{fa}} \tag{3.6}$$

Step I:

By integrating Eq. (3.6) with boundary condition of $T_{a2}(0) = T_i$, the expression of T_{a2} temperature vs. distance x is obtained as:

$$T_{a2}(x) = \frac{T_i + (e^{\frac{x}{c_{wf}\dot{m}_{wf}R_{fa}}} - 1)T_e}{e^{\frac{x}{c_w m_w R_{fa}}}} \tag{3.7}$$

and,

$$T_L = \frac{T_i + (e^{\frac{L}{c_{wf}\dot{m}_{wf}R_{fa}}} - 1)T_e}{e^{\frac{L}{c_w m_w R_{fa}}}} \tag{3.8}$$

where, L is the length of DHE and T_L is the working fluid (n-butane) temperature at the plugged end of the annulus.

Step II:

By combining Eq. (3.4) and Eq. (3.5), the expression for T_{a1} is obtained:

$$R_{at}c_{gf}\dot{m}_{gf}c_{wf}\dot{m}_{wf}T_{a1}^{''} + (c_{wf}\dot{m}_{wf} - c_{gf}\dot{m}_{gf})T_{a1}^{'} = 0 \tag{3.9}$$

with following two boundary conditions at plugged end and cross-over end, respectively:

$$T_{a1}(L) = T_L$$

$$T_t(0) = T_e$$

For Eq. (3.9), analytical solution is obtained as:

$$T_{a1} = C_1 + C_2 e^{rx} \tag{3.10}$$

where,

$$r = \frac{c_{gf}\dot{m}_{gf} - c_{wf}\dot{m}_{wf}}{c_{gf}\dot{m}_{gf}c_{wf}\dot{m}_{wf}R_{at}}$$

and, integration constants are:

$$C_1 = T_L - C_2 e^{rL}$$

$$C_2 = \frac{T_L - T_e}{R_{at}c_{wf}\dot{m}_{wf}r + e^{rL} - 1}$$

Thus, the temperature at the outlet of DHE is

$$T_{out} = T_{a1}(0) = C_1 + C_2 \tag{3.11}$$

Configuration II (WFT)

As indicated in Figure 3.2b, geofluid (brine) circulates through Annulus II driven by a downhole pump. The working fluid (n-butane) is injected into DHE from tubing and returns through Annulus I. Tubing is insulated to avoid heat loss from working fluid (n-butane) in Annulus I to the flow path in the tubing. The governing equations can be derived similar to the previous configuration.

Tubing:

$$A_t \rho_{wf} c_{wf} \frac{\partial T_t}{\partial t} = \frac{T_{a1} - T_t}{R_{at}} - c_{wf} \dot{m}_{wf} \frac{\partial T_t}{\partial x} \tag{3.12}$$

Annulus I:

$$A_{a1} \rho_{wf} c_{wf} \frac{\partial T_{a1}}{\partial t} = \frac{T_{a2} - T_{a1}}{R_{aa}} + \frac{T_t - T_{a1}}{R_{at}} + c_{wf} \dot{m}_{wf} \frac{dT_{a1}}{dx} \tag{3.13}$$

Annulus II:

$$A_{a2} \rho_{gf} c_{gf} \frac{\partial T_{a2}}{\partial t} = \frac{T_e - T_{a2}}{R_{fa}} + \frac{T_{a1} - T_{a2}}{R_{aa}} - c_{gf} \dot{m}_{gf} \frac{dT_{a2}}{dx} \tag{3.14}$$

Based on the same assumptions, the analytical solution is derived as follows.

Annulus I:

$$c_{wf} \dot{m}_{wf} \frac{dT_{a1}}{dx} = \frac{T_{a1} - T_{a2}}{R_{aa}} \tag{3.15}$$

Annulus II:

$$c_{gf} \dot{m}_{gf} \frac{dT_{a2}}{dx} = \frac{T_e - T_{a2}}{R_{fa}} + \frac{T_{a1} - T_{a2}}{R_{aa}} \tag{3.16}$$

By combining above two equations, we have a second-order ODE (notice that $B^2 - 4AC$ is always greater than zero for positive mass flow rates).

$$A T_{a1}^{''} + B T_{a1}^{'} + C T_{a1} + T_e = 0 \tag{3.17}$$

where,

$$A = R_{aa} R_{fa} c_{gf} \dot{m}_{gf} c_{wf} \dot{m}_{wf}$$

$$B = R_{fa} c_{wf} \dot{m}_{wf} + R_{aa} c_{wf} \dot{m}_{wf} - R_{fa} c_{gf} \dot{m}_{gf}$$

$$C = -1$$

with two boundary conditions:

$$T_{a1}(L) = T_i$$

$$T_{a2}(0) = T_e$$

For above equation, analytical solution is achieved by assuming constant thermal properties and applying two boundary conditions.

$$T_{a1} = C_1 e^{r_1 x} + C_2 e^{r_2 x} + T_e \tag{3.18}$$

where,

$$r_1 = \frac{-B + \sqrt{B^2 - 4AC}}{2A}$$

$$r_2 = \frac{-B - \sqrt{B^2 - 4AC}}{2A}$$

and, integrate constants are:

$$C_1 = \alpha(\frac{T_i - T_e}{\alpha e^{r_1 L} + e^{r_2 L}})$$

$$C_2 = \frac{T_i - T_e}{\alpha e^{r_1 L} + e^{r_2 L}}$$

$$\alpha = (\frac{1 - R_{aa} c_{wf} \dot{m}_{wf} r_2}{R_{aa} c_{wf} \dot{m}_{wf} r_1 - 1})$$

For this configuration, the temperature at the outlet of DHE is

$$T_{out} = T_{a1}(0) = C_1 + C_2 + T_e \tag{3.19}$$

3.1 Thermal Resistance Concept to Model Convection Effect

Introducing the concept of thermal resistance (Bauer, et al., 2010) into this study, the overall thermal resistance can be divided into three components (Figure 3.4): tubing-annulus I (R_{at}), annulus I-annulus II (R_{aa}), and annulus II-formation (R_{af}).

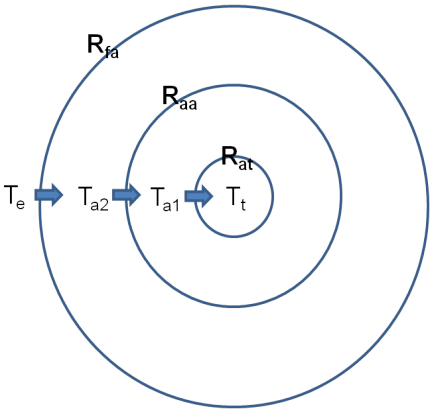

Figure 3.4: Schematic of the DHE to highlight various thermal resistances.

Thermal Resistance between Tubing-Annulus I (R_{at}):

The thermal resistance between tubing and annulus I is further divided into three serially connected processes: inside tubing, on the tubing, and in annulus I. On the tubing, the heat transfer is purely conductive. In tubing and annulus I, both conduction and convection are considered, and the thermal resistances are the results of parallel connection of both conductive and convective effects. Following equation presents the overall thermal resistance.

$$R_{at} = \frac{1}{\frac{1}{R_{cond,t}} + \frac{1}{R_{conv,t}}} + R_{cond,tubing} + \frac{1}{\frac{1}{R_{cond,a1}} + \frac{1}{R_{conv,a1}}} \tag{3.20}$$

where, the subscripts t, tubing, a1, cond, and conv represent inside tubing, tubing, annulus I, conduction and convection.

Due to high rate of pipe flow, the overall heat transfer is dominated by convection effect. In another words, comparing to R_{conv}, R_{cond} is larger enough for flow in tubing and annulus I. So, the above equation can be simplified as:

$$R_{at} = R_{conv,t} + R_{cond,tubing} + R_{conv,a1} \tag{3.21}$$

where,

$$R_{conv,t} = \frac{1}{\pi d_{ti} h_t} = \frac{1}{\pi d_{ti} \frac{Nu_t k_t}{d_{ti}}} = \frac{1}{\pi N u_t k_t}$$
$$R_{cond,tubing} = \int_{rti}^{rto} \frac{1}{2\pi r k_{tubing}} dr = \frac{ln(r_{to}/r_{ti})}{2\pi k_{tubing}}$$
$$R_{conv,a1} = \frac{1}{\pi d_{to} h_{a1}} = \frac{1}{\pi d_{to} \frac{Nu_{a1} k_{a1}}{d_{c1i} - d_{to}}} = \frac{1}{\pi N u_{a1} k_{a1}} \frac{d_{c1i} - d_{to}}{d_{to}}$$

Thermal Resistance between Annulus I-Annulus II (R_{aa}):

Similar to tubing-annulus I, we have following equations.

$$R_{aa} = R_{conv,a1} + R_{cond,c1} + R_{conv,a2} \tag{3.22}$$

where,

$$R_{conv,a1} = \frac{1}{\pi d_{c1i} h_{a1}} = \frac{1}{\pi d_{c1i} \frac{Nu_{a1} k_{a1}}{d_{c1i} - d_{to}}} = \frac{1}{\pi N u_{a1} k_{a1}} \frac{d_{c1i} - d_{to}}{d_{c1i}}$$
$$R_{cond,c1} = \frac{ln(r_{c1o}/r_{c1i})}{2\pi k_{c1}}$$
$$R_{conv,a2} = \frac{1}{\pi d_{c1o} h_{a2}} = \frac{1}{\pi d_{c1o} \frac{Nu_{a2} k_{a2}}{d_{c2i} - d_{c1o}}} = \frac{1}{\pi N u_{a2} k_{a2}} \frac{d_{c2i} - d_{c1o}}{d_{c1o}}$$

Thermal Resistance between Annulus II-Formation (R_{af}):

A significant difference for annulus II-formation is that the heat transfer from formation to casing II may not be dominated by convection due to the low flow rate in porous media. So, the resultant thermal resistance (R_{af}) includes conduction effects.

$$R_{fa} = R_{conv,a2} + R_{cond,c2} + \frac{1}{\frac{1}{R_{cond,2}} + \frac{1}{R_{conv,e}}} \tag{3.23}$$

where,

$$R_{conv,a2} = \frac{1}{\pi d_{c2i} h_{a2}} = \frac{1}{\pi d_{c2i} \frac{Nu_{a2} k_{a2}}{d_{c2i} - d_{c1o}}} = \frac{1}{\pi N u_{a2} k_{a2}} \frac{d_{c2i} - d_{c1o}}{d_{c2i}}$$

$$R_{cond,c2} = \frac{ln(r_{c2o}/r_{c2i})}{2\pi k_{c2}}$$

$$R_{cond,e} = \frac{ln(r_e/r_{c2o})}{2\pi k_e}$$

$$R_{conv,e} = \frac{1}{\pi d_{c2o} h_{a2}} = \frac{1}{\pi d_{c2o} \frac{Nu_e k_e}{d_e - d_{c2o}}} = \frac{1}{\pi N u_e k_e} \frac{d_e - d_{c2o}}{d_{c2o}}$$

Nu, standing for Nusselt number, presents the ratio of convective to conductive across the boundary ($\frac{hL}{k_f}$). It can be solved using following correlation for appropriate conditions.

Gnielinski correlation:

$Nu = \frac{(f/8)(Re-1000)Pr}{1+12.7(f/8)^{0.5}(Pr^{2/3}-1)}$

for $0.5 \leq Pr \leq 2000, 3000 \leq Re \leq 5 \times 10^6$

Dittus-Boelter correlation:

$Nu = 0.023 Re^{0.8} Pr^n$

for $0.7 \leq Pr \leq 160, 10000 \leq Re$

where, n=0.4 for heating of fluid and 0.3 for cooling, f is friction factor, Re is Reynolds number describing ration of inertial forces to viscous forces ($\frac{\rho v L}{\mu}$), and Prandtl number, Pr, represents the ratio of kinematic viscosity to thermal diffusivity ($\frac{c_p \mu}{k}$).

As mentioned, the novel DHE design could increase heat extraction rate by enlarging the thermal drainage volume in the geothermal reservoir. However, focusing on DHE, there is another advantage on the aspect of thermal resistance. For the conventional DHE, R_{af} determines the overall heat extraction, because all of the energy will be transfered from formation to working fluid in DHE though R_{af}. Contrarily, in the presented DHE design, part of heat is transfered over R_{af}, and others flow through either R_{at} for GFT configuration or R_{aa} for

WFT configuration. And in this study, the thermal resistances R_{at} and R_{aa} are calculated as 16 and 28 times less than R_{af}. Therefore, the novel DHE design increases overall heat transfer coefficient as well.

3.2 Comparison of Overall Heat Extraction Rates for Configuration I & II

Parameters used for the calculation are summarized in Table 3.1, and the results are shown in the Figure 3.5.

Table 3.1: Baseline parameters used for sensitivity study.

Formation Parameters	
rock density	$2700 kg/m^3$
heat conductivity	$1.9 W/m^oC$
temperature	300^oF
DHE Geometry	
length (baseline)	$1000 ft$
casing II OD/ID	$8.625/7.625 in$
casing I OD/ID	$6.625/6.0474 in$
tubing OD/ID	$5/4.276 in$
heat conductivity	$45 W/m^oC$
n-Butane Properties	
density	$582 kg/m^3$
heat conductivity	$0.107 W/m^oC$
specific thermal capacity	$2763 J/(kg^oC)$
viscosity	$0.17 cp$
injection temperature	90^oF
mass flow rate	$5.25 kg/s$
Brine Properties	
density	$1000 kg/m^3$
heat conductivity	$0.519 W/m^oC$
specific thermal capacity	$3182 J/(kg^oC)$
viscosity	$0.11 cp$
Total water circulation rate	$2.34 kg/s$

As shown in Figure 3.5, the temperature at DHE outlet (cross-over end) of Configuration I (236^oF) is lower compared to the exit temperature of Configuration II (251^oF). This implies a lower heat extraction efficiency for GFT configuration. Further, for the first configuration

(GFT), heat extracted from the rock and geofluid are 54% and 46%, respectively. However, for the WFT configuration, the corresponding percentages are 37.5% and 62.5%. This phenomena results in a lower geofluid reinjection temperature of 104^oF, compared to the 169^oF for the GFT configuration. Therefore, a longer DHE may be preferred for the WFT configuration when applied in a real geothermal reservoir, so that the cooler brine can be fully heated before returning to producer.

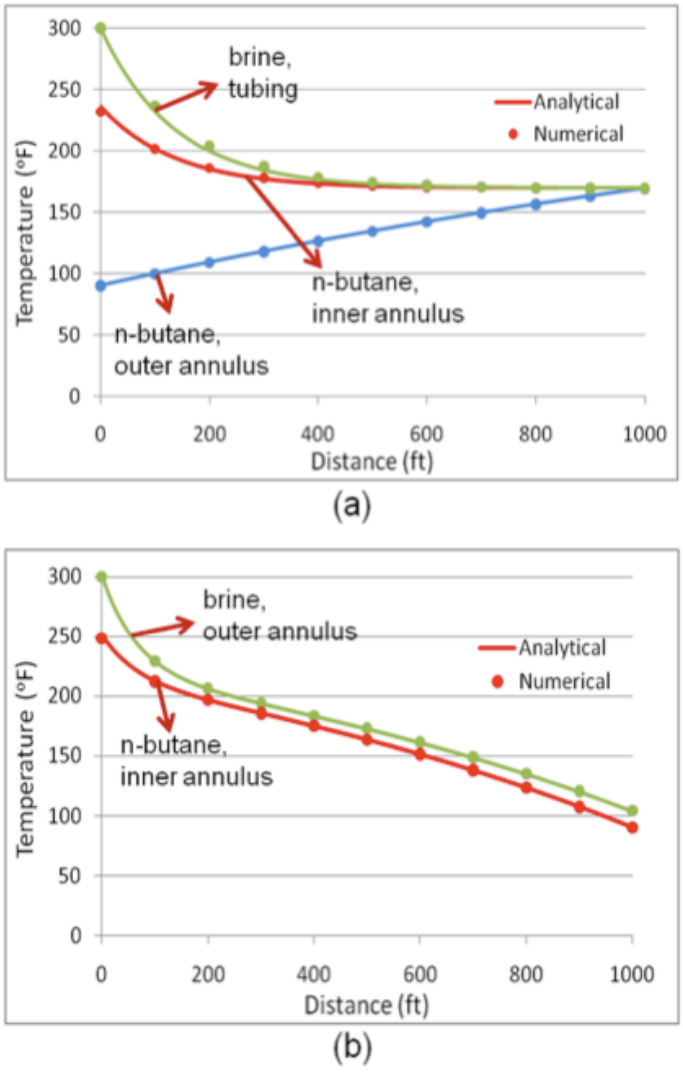

Figure 3.5: Temperature variation along flow path in DHE for different configurations: (a) GFT; (b) WFT.

3.3 Parametric Sensitivity Study

Several sensitivity studies were carried out to analyze the performance of DHE. The baseline parameters used are shown in Table 3.1. The operating conditions in Table 3.1 are chosen to match the requirement of commercially available ORC engines such as ORMAT (http://www.ormat.com) and UTRC (http://www.utrc.utc.com). Parameters that are varied in this study are: heat exchanger length, working fluid flow rate, and geofluid flow rate.

(1) DHE Length

The working fluid temperature in the DHE is sensitive to the length of DHE, because a longer DHE provides a larger heat exchange area. As shown in Figure 3.6, as the heat exchanger length increasing from 500ft to 2000ft. the outlet working fluid temperature is increasing from 215^{o}F to 255^{o}F for the first configuration, and from 223^{o}F to 277^{o}F for the second configuration.

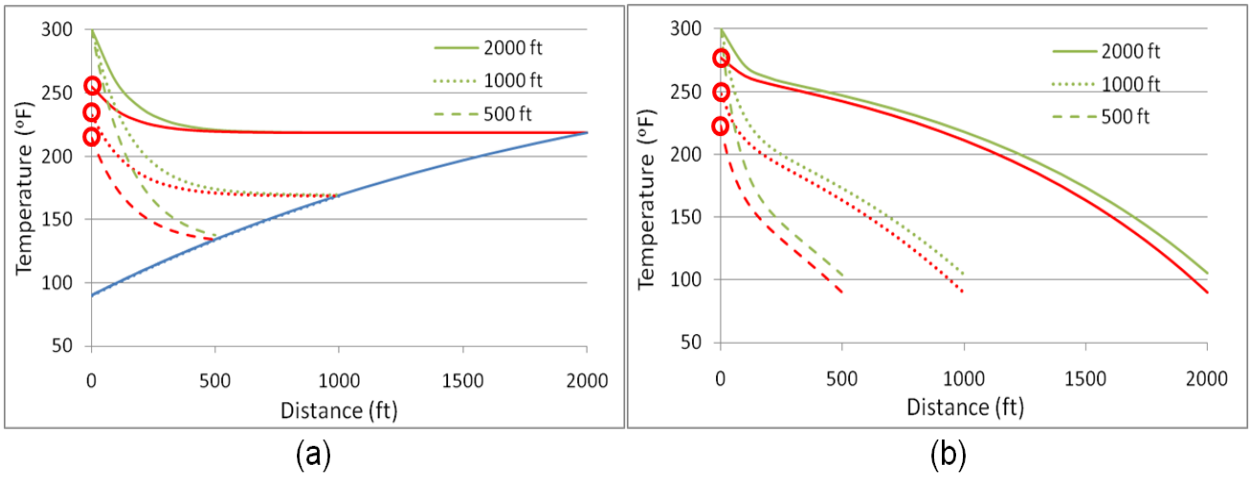

Figure 3.6: Temperature variation along flow path in DHE for different heat exchanger lengths [2000ft, 1000ft and 500ft] : (a) Configuration I (GFT); (b) Configuration II (WFT).

(2) Working Fluid Mass Flow Rate

The amount of heat extracted by the working fluid in the DHE can be calculated as $\dot{m}_{wf}c_{wf}(T_{wf}^{out} - T_{wf}^{in})$. Therefore, for a given injection temperature, the decreasing outlet

temperature alone dose not determine the overall exchanged heat.

As noted in Figure 3.7, as the mass flow rate increased from 2.63kg/s to 10.5kg/s, the outlet working fluid temperature decreased from 291^{o}F to 174^{o}F for the first configuration, and from 298^{o}F to 178^{o}F for the second configuration. However, with increasing mass flow rate, the amount of heat extracted by working fluid increased from 0.82MW to 1.36MW and from 0.84MW to 1.43MW for first and second configuration, respectively.

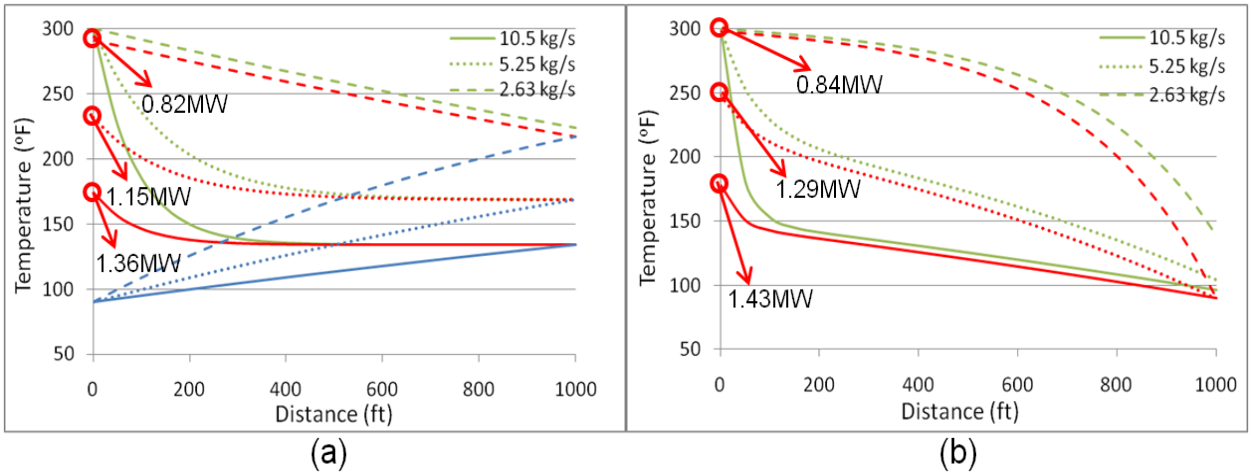

Figure 3.7: Temperature variation along flow path in DHE for different working fluid (n-butane) mass flow rates [10.5kg/s, 5.25kg/s and 2.63kg/s]: a) Configuration I (GFT); b) Configuration II (WFT).

(3) Geofluid Mass Flow Rate

Higher geofluid mass flow rate will increase the overall heat extraction rate by enhancing heat transfer efficiency and amount of heat in the system. However, the electricity consumed to drive the downhole pump could be a major problem, especially for the poorly permeable geothermal reservoirs.

As indicated in Figure 3.8, as water mass flow rate increased from 1.17kg/s to 4.68kg/s, the outlet working fluid temperature (heat extraction rate) is increasing from 199^{o}F (0.89MW)

to 284^{o}F (1.58MW) for the first configuration and from 207^{o}F (0.95MW) to 294^{o}F (1.66MW) for the second configuration.

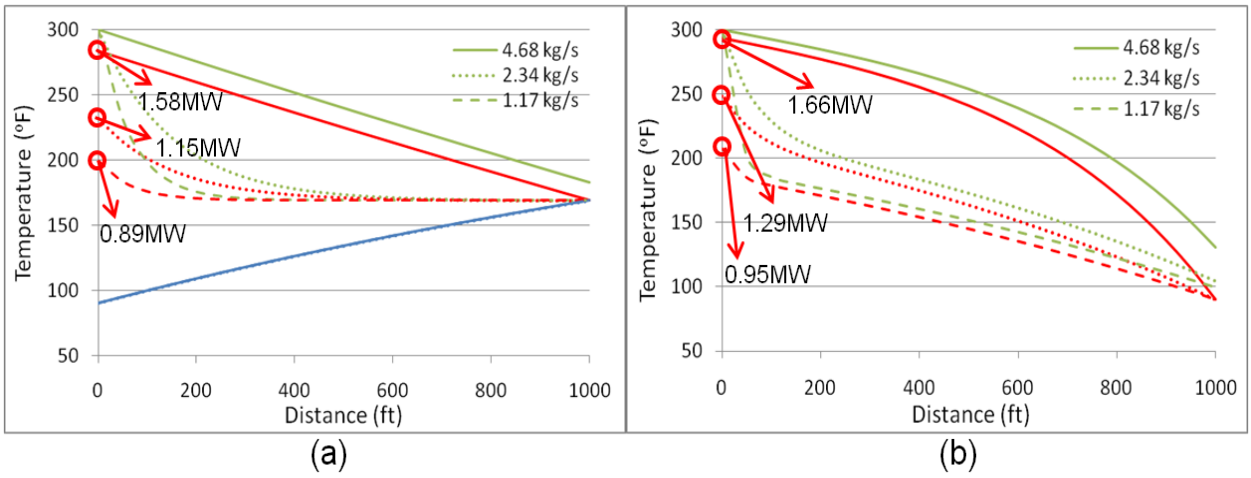

Figure 3.8: Temperature variation along flow path in DHE for different geofluid (brine) mass flow rates [4.68kg/s, 2.34kg/s and 1.17kg/s]: a) Configuration I (GFT); b) Configuration II (WFT).

3.4 Thermodynamic Analysis for the ORC with DHE

A binary power plant, which is proved to be more efficient for low or medium temperature resources (Dipippo, 2008), is employed coupling with the DHE (Figure 3.9). The working fluid is n-Butane and the thermodynamic cycle is also known as Organic Rankine Cycle (ORC). The second configuration is taken as an example implementation, even though the precess is pretty similar to the first one.

As shown in Figure 3.9, working fluid is injected through annulus II from surface in liquid phase. During moving in DHE, it remains liquid phase due to high pressure. As elevating in the vertical section, once the pressure drops below vapor pressure at a certain depth, the phase change occurs and n-butane becomes vapor which would drive the turbine to generate electricity. After that, the working fluid comes back to liquid phase in condenser and then is reinjected into DHE.

Since no any fluid produced or injected through the vertical section of tubing, this part is designed to be cut off leaving only the horizontal section for circulating geofluid, as a result, the cost on thousands of feet tubing is avoid.

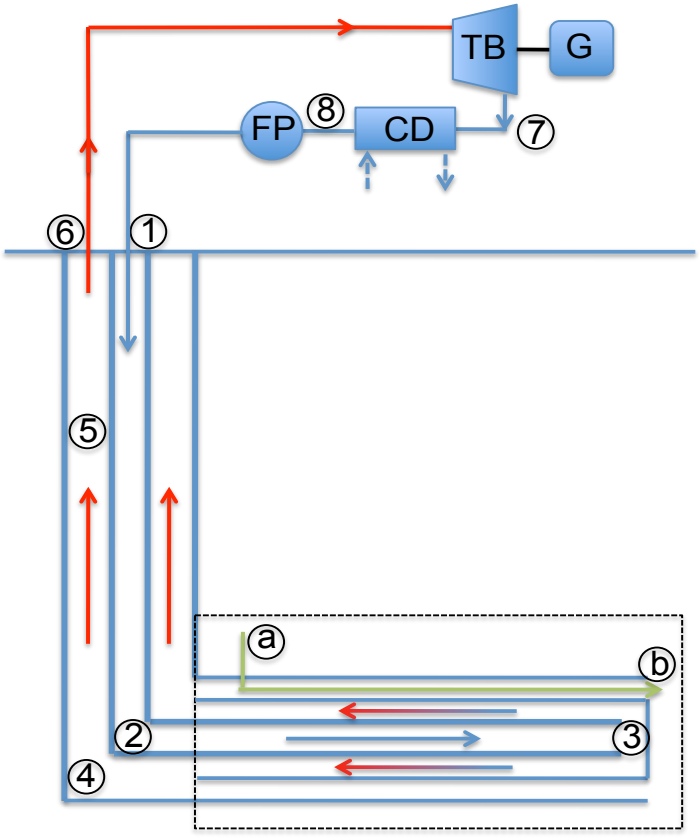

Figure 3.9: Schematic of a binary cycle linked with the presented DHE (FP-feed pump, TB-turbine, CD-condenser, numbers 1-8 represent state numbers).

For thermodynamic analysis, properties including pressure (P), temperature (T), specific enthalpy (h) and specific entropy (s) at each state number can be determined by any given two properties. The thermodynamic properties are solved based on a thermodynamic property chart and following assumptions: 1) the power plant is considered under steady state condition. 2) pressure drops through surface pipeline and condenser are negligible. 3) kinetic and potential energy at surface facilities are negligible. 4) Fresh water thermodynamic chart was used for geofluid thermodynamic analysis.

Some useful equations for the calculations are listed as follows.

$$\dot{Q} + \dot{W} = \sum \dot{m}_{out} h_{out} - \sum \dot{m}_{in} h_{in} \tag{3.24}$$

$$\dot{E}_{heat} + \dot{W} = \sum \dot{E}_{out} - \sum \dot{E}_{in} + \dot{I} \tag{3.25}$$

where, the subscripts *in* and *out* stand for the inlet and outlet states, $\dot{Q}$ and $\dot{W}$ are the input net heat and work, h and $\dot{I}$ represent enthalpy and the rate of exergy destruction, respectively. $\dot{E}$ is defined as:

$$\dot{E}_{heat} = \sum (1 - \frac{T_0}{T}) \dot{Q} \tag{3.26}$$

The specific flow exergy is:

$$e = h - h_0 - T_0(s - s_0) \tag{3.27}$$

The power of the turbine in the cycle is given by:

$$\dot{W}_t = \dot{m}_{wf}(h_6 - h_7) \tag{3.28}$$

where,

$$h_7 = h_6 - \eta(h_6 - h_{7s}) \tag{3.29}$$

The power consumed by pump is:

$$\dot{W}_{fp} = \dot{m}_{wf}(h_1 - h_8) \tag{3.30}$$

with the efficiency as:

$$\eta_p = \frac{v(P_1 - P_8)}{h_1 - h_8} \tag{3.31}$$

The exergy efficiency for turbine is:

$$\eta_{ex,t} = \frac{\dot{W}_t}{\dot{E}_6 - \dot{E}_7} \tag{3.32}$$

For pump:

$$\eta_{ex,p} = \frac{\dot{E}_1 - \dot{E}_8}{\dot{W}_p} \tag{3.33}$$

Following procedures are used for the thermodynamic analysis for the ORC operated along DHE.

1) By given injection pressure P_1 and temperature T_1, s_1 and h_1 can be read from n-Butane thermodynamic property chart.

2) $T_2 = T_1$ in case of insulation or it can be estimated by wellbore heat transfer. P_2 is $P_1 + \Delta P_{hydraulic} - \Delta P_{friction}$. Based on them, s_2 and h_2 are obtained from the chart.
The frictional pressure gradient is represented by:

$$\frac{dP}{dz} = -\frac{fv^2\rho}{2g_c d} \tag{3.34}$$

where, f is the Moody friction factor (Eq. 3.35 proposed by Chen (1979)), d represents pipe diameter, v is velocity, and g_c is conversion factor ($32.17\frac{lbm-ft}{lbf-s^2}$).

$$\frac{1}{f} = \left[2log\left(\frac{\varepsilon/d}{3.7065} - \frac{5.0452}{Re}log(\Lambda)\right)\right]^2 \tag{3.35}$$

with

$$\Lambda = \frac{(\varepsilon/d)^{1.1098}}{2.8257} + \left(\frac{7.149}{Re}\right)^{0.8981} \tag{3.36}$$

where, ε is pipe roughness and Re is Reynolds number ($\frac{\rho v d}{\mu}$).

3) T_3 is calculated from DHE simulator with $P_3 = P_2 + \Delta P_{hydraulic} - \Delta P_{friction}$. s_3 and h_3 are read from thermodynamic chart.

4) Same as 3).

5) T_5 is similar to T_4 due to the insulation with P_5 equals n-butane vapor pressure at T_5 (Eq. 3.37 presented by Kay (1940)). (read for s_5 and h_5).

$$log_{10}^P = \frac{-1654.1}{T} + 1.7047log_{10}^T - 1.988 \times 10^{-5}T \tag{3.37}$$

where, P=pressure, psi and T=temperature, ^oR.

6) $P_6 = P_5 - \Delta P_{hydraulic} - \Delta P_{friction}$ and $T_6 = T_5$ (read chart for s_6 and h_6).

7s) Before solving state 7, we first assume an isentropic process where $s_{7s} = s_6$ and P_7 is specified. As a result, h_{7s} and s_{7s} can be read.

7) On the base of given turbine isentropic efficiency ($\eta_t = \frac{h_6 - h_7}{h_6 - h_{7s}}$), h_7 is solved. With specified P_7, T_7 and s_7 is achievable.

8) Based on pump isentropic efficiency ($\eta_p = \frac{h_{1s} - h_8}{h_1 - h_8} = \frac{P_1 - P_8}{\rho(h_1 - h_8)}$), h_8 is calculated by applying $P_8 = P_7 - \Delta P_{friction}$. Consequently, T_8 and s_8 is achievable.

The results are summarized in following table.

Table 3.2: Thermodynamic properties with state numbers referring to Figure 3.8

State no.	Temperature T (^oF)	Pressure P (MPa)	Enthalpy h (kJ/kg)	Entropy s (kJ/kg^{o}K)	Exergy rate $\dot{E}$ (kW)
0	25	0.1	328	5.32	0
1	32	0.4	-23	4.02	191.1
2	32	14.2	-13	3.98	306.2
3	32	14.2	-13	3.98	306.2
4	121	14.1	220	4.65	481.2
5	121	2.3	442	5.27	676.7
6	121	1.9	460	5.34	661.7
7s	58	0.3	380	5.34	241.7
7	65	0.3	392	5.37	257.8
8	32	0.3	-23.2	4.02	189.9

In the case, the turbine outlet pressure is set at 0.3 MPa to ensure that the fluid remains in vapor phase in, and a pump will be needed to increase pressure at state 8 to state 1. The power generated by turbine is 357kW. By the assumed feed pump isentropic efficiency (0.75%) and designed working fluid mass circulating rate of 5.25 kg/s, the electricity required

to drive the pump is estimated as 1.1kW. The turbine exergy efficiency is calculated to be 88% and fluid pump efficiency is near 100%. The resulting thermodynamic efficiency of DHE is 29%.

Chapter 4
Low-enthalpy Saturated Geothermal Resources

Saturated geothermal resource such as hot saline aquifer (HSA) or geopressured geothermal brines (GGB) with the above mentioned temperature range and reasonable formation permeability, are good candidate for geothermal low-enthalpy models. In this Chapter, a simplified conceptual model is studied to evaluate the effect of natural convection effect on a DHE modeled as a line sink with linear temperature variation. Further, a field case study is also provided using the parameters corresponding to "Camerina A" reservoir.

4.1 Conceptual HSA Model

During heat extraction from a permeable, saturated geothermal reservoir, the fluid flow in the porous media transports the heat by both natural as well as forced convection modes. The effect of natural convection is usually small as compared to the forced convection. However, at the time scales of late production life, natural convection might play a significant role.

To take advantage of natural convection, a downhole heat exchanger (DHE) is placed in a long lateral wellbore as a horizontal heat sink with linearly varying temperatures located at the center of the saturated aquifer layer. A sketch of conceptual geothermal reservoir is shown in Figure 4.1, and the boundary conditions for the reservoir are applied as follows.

a. All six faces of reservoir are subjected to no normal flow boundaries.

b. Top and bottom surfaces are maintained at constant heat flux corresponding to the pervailing geothermal gradient.

c. Zero heat flux is specified at the other four vertical faces.

d. Heat sink with linear temperature distribution (from 120 ^{o}F at one end to 240^{o}F at the other end) is located at the center of this reservoir.

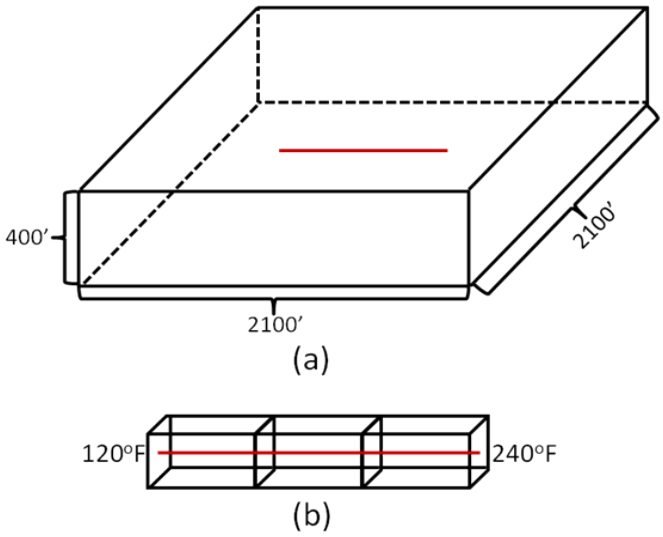

Figure 4.1: (a) Schematic of the conceptual geothermal reservoir model; (b) Boundary conditions around the DHE.

Figure 4.2 shows section of the HSA model with x-z plane parallel to the DHE axis and y-z plane perpendicular to it. D_H is the dimensionless distance from top of the model. In this figure, we can see that the shallower location of DHE extracts heat from the larger "swept" volume of the reservoir and the deeper location can only influence the heat flux around the bottom layer. Asymmetric temperature contours are result of linearly varying temperature imposed along the DHE.

The detailed results of heat production rate and cumulative heat produced are referred in Feng et al. (2011). Heat extraction rates for different DHE heights are compared in Figure 4.3. According to the comparison results, DHE located at vertical depth of $D_H = 0.25$ has the highest heat extraction rate. Noted that, the results are thermal power not electrical power. Even for the maximum thermal power provided, the estimated electrical power is about 60kW.

Figure 4.4 shows 3D streamlines colored by the temperature value. As the heat sink cools down the near wellbore reservoir region, the cooled reservoir fluid convects downward due to

the increase in density. However, the cold fluid is heated again as it approaches the bottom hot layers. Natural convection maintains this cycle of heat extraction around the DHE.

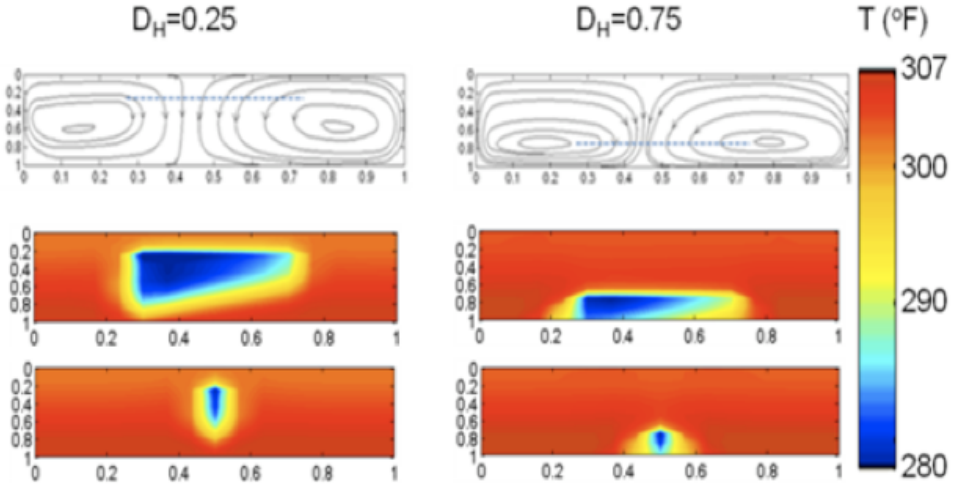

Figure 4.2: 2D Contour/streamline plots of temperature and velocity profiles [top row: streamlines at x-z plane with $D_y = 0.5$; middle row: isotherms at x-z plane with $D_y = 0.5$; bottom row: streamlines at y-z plane with $D_x = 0.5$].

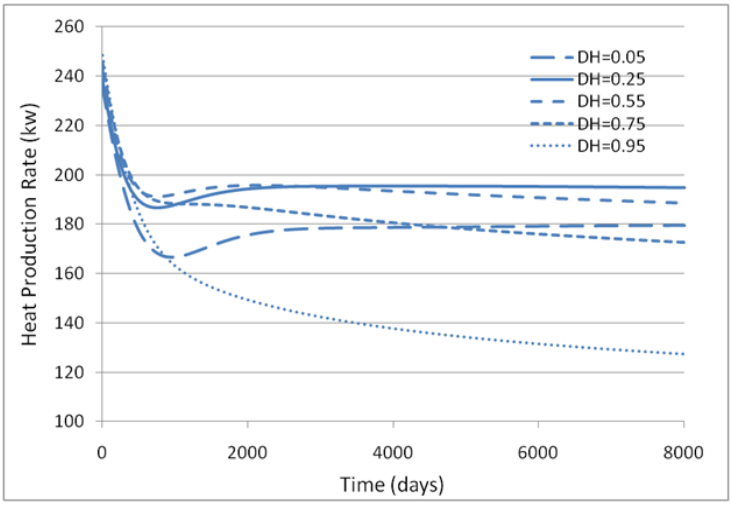

Figure 4.3: Heat extraction rates for different DHE depths (Feng et al., 2011).

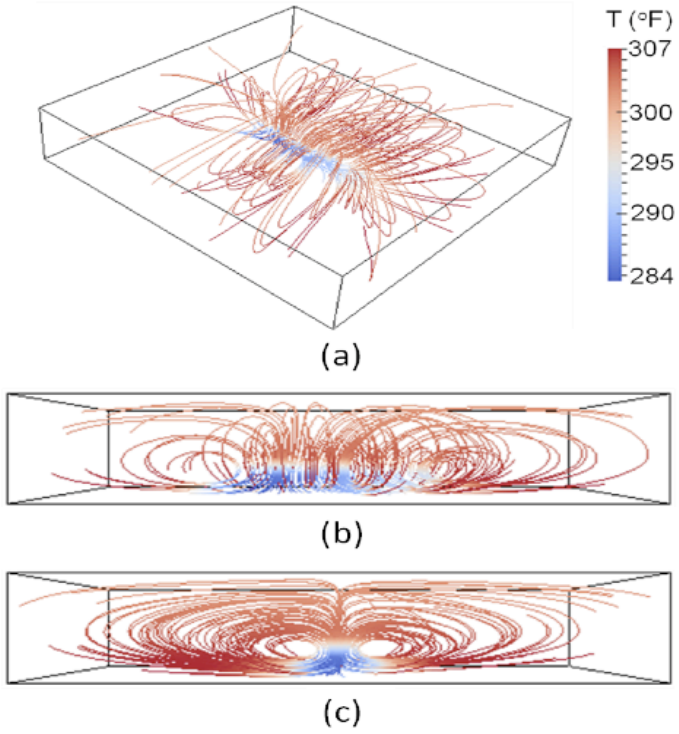

Figure 4.4: (a) Overview of 3D streamlines colored by temperature; (b) x-z plane slice show of 3D streamlines; (c) y-z plane slice show of 3D streamlines.

4.2 Field Case Study-Camerina A

According to Gray (2010), salt domes in South Louisiana may potentially be an economic resource of geothermal energy. The brine saturated Camerina A sand, near Gyuedan Salt dome in Vermillion parish, LA (Figure 4.5), is an example of saturated geothermal resources as suggested by Gray (2010). Kehle (1972) corrected formation temperatures for the Camerina A varies from 128^{o}C (262^{o}F) to 160^{o}C (320^{o}F), that implies Camerina A is defined as a low-enthalpy geothermal resource.

In Figure 4.6, the middle layer is modeled as the saturated reservoir - Camerina A. Top and bottom represent the impermeable layers where only conduction effect dominated, and are modeled to disable conjugate heat transfer between layers. Average temperature in the

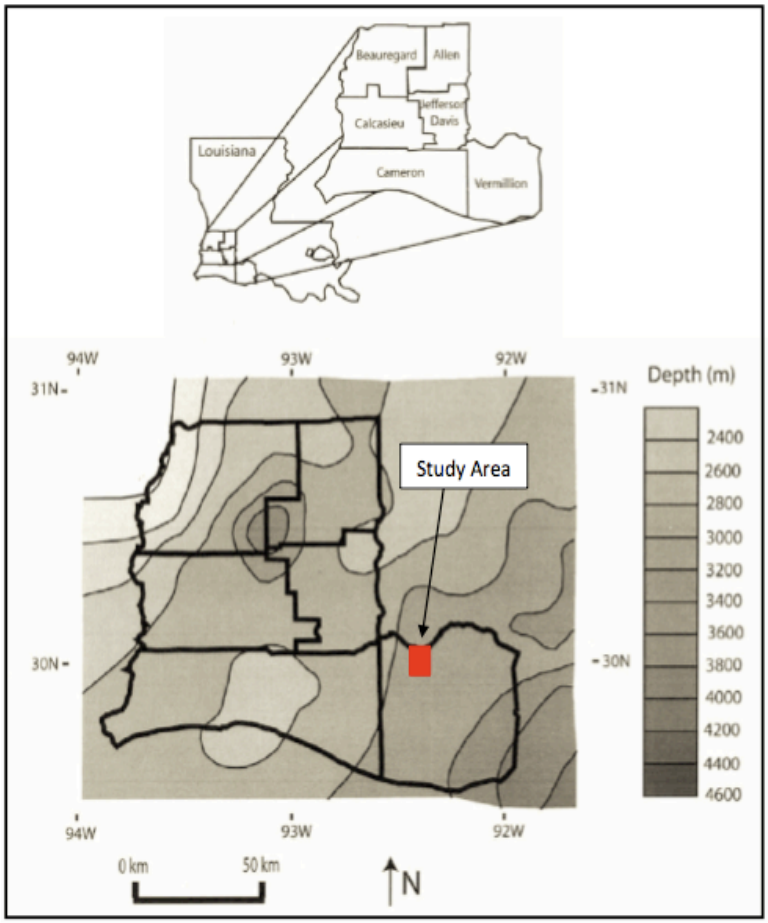

Figure 4.5: 100^{o}C isotherm map of the study area (Szalkowski and Hanor, 2003).

permeable middle layer is 142^{o}C (287^{o}F). Several parametric studies are conducted and results are summarized in following section to evaluate the performance of the DHE and the heat extraction in HSAs. The varied parameters studied here are the reinjection distance for the "spent" geofluid from DHE (Figure 4.7), effect of dip angle in HSA, and the length of DHE.

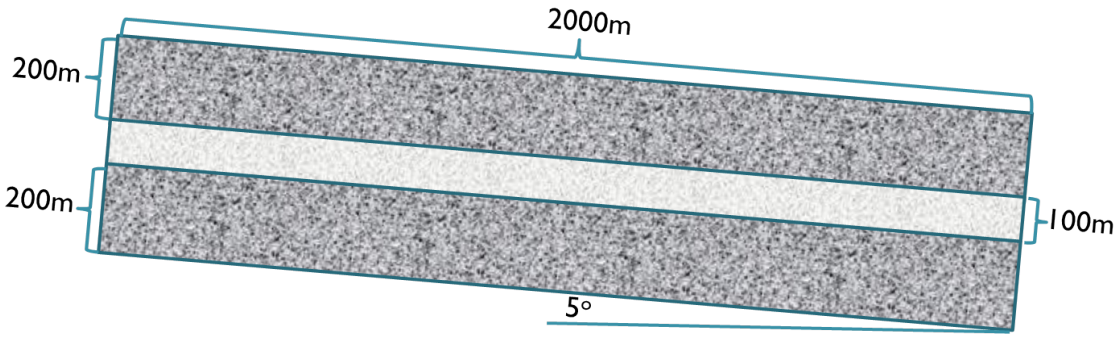

Figure 4.6: Sketch of x-z plane of computational Camerina A model.

As suggested by Gray (2010), parameters corresponding to Camerina A are summarized in Table 4.1.

Table 4.1: Parameters corresponding to field case study-Camerina A.

Formation Parameters	
rock density	$2700 kg/m^3$
heat conductivity	$1.9 W/m^oC$
geothermal gradient	$28^oC/km$
permeability	$200 md$
porosity	20%
dip angle	5^o
thickness	$100 m$
width×length	$2000 m \times 2000 m$
Geofluid	
density	$1000 kg/m^3$
heat conductivity	$0.649 W/m^oC$
specific thermal capacity	$3726/(kg^oC)$
viscosity	$0.3 cp$

Reinjection Distance

Using the second configuration of DHE (WFT), the heat circulating of the geofluid flow in the reservoir can be avoided, and the larger heat sweep volume can be obtained using the strategy of separating the reinjection location further away from the DHE.

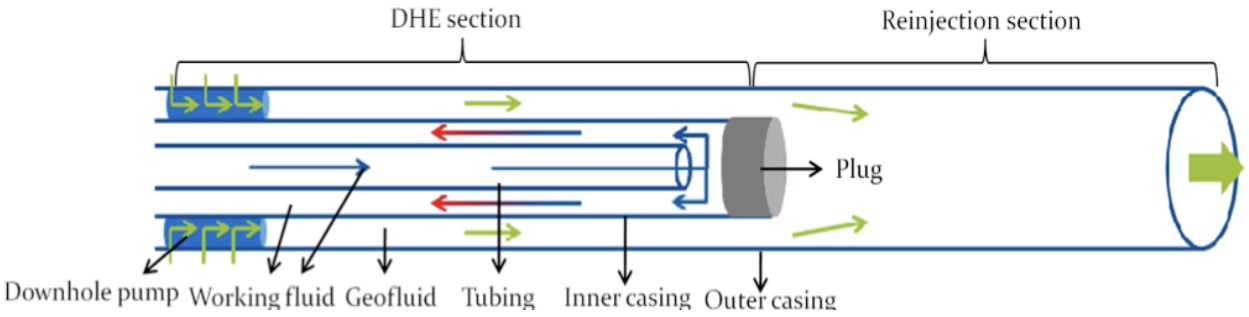

Figure 4.7: Sketch of DHE used in Camerina A geothermal reservoir with an extended reinjection horizontal wellbore section.

Figure 4.8 presents the different working fluid (n-butane) temperatures at the outlet (crossover end) of DHE in the situation of with/without the extended reinjection section. By reinjecting the cold geofluid further away from the DHE (plugged end), the cooling down in the vicinity of the DHE can be improved.

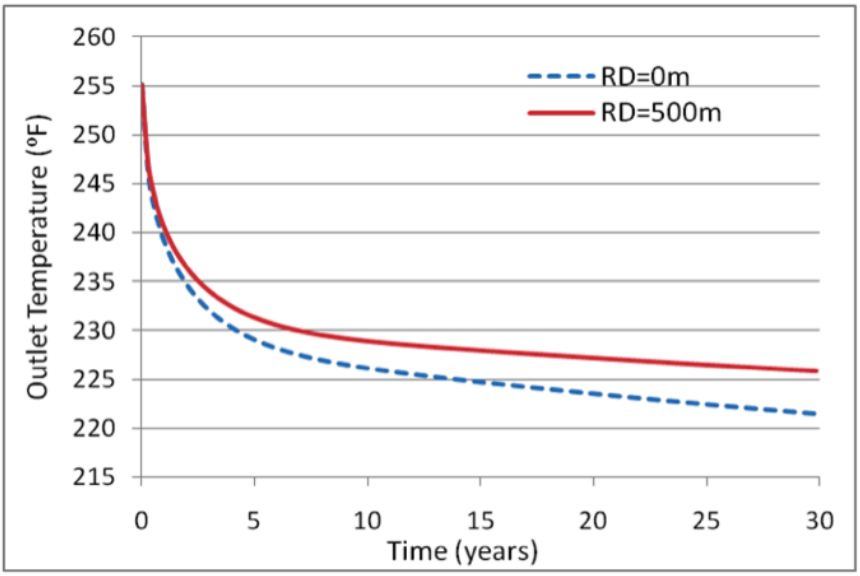

Figure 4.8: Working fluid temperature variation vs. time for different reinjection distance, where RD is defined as reinjection distance.

As noted, after 30 years production, the outlet working fluid temperature for the DHE with 500m reinjection distance is 4.5^{o}F higher compared to the one with no reinjection section. This temperature increase is equivalent to 36kW thermal power and about 11kW electricity

power. In addition, as production goes on, temperature difference between two scenarios tends to be larger.

Dip Angle

The performance of DHE in geothermal reservoirs with different dip angles is studied here. According to Gray (2010), the range of dip angle in Camerina A is from 1.2^o to 28^o. Therefore, the comparison cases include three dip angles of (0^o, 5^o, and 28^o) and two configurations for geofluid reinjection (downdip: deeper reinjection location for cooler geofluid; updip: shallower reinjection location for cooler geofluid). Figure 4.9 shows the comparison of above stated scenarios starting from the same temperature baseline in the permeable layer.

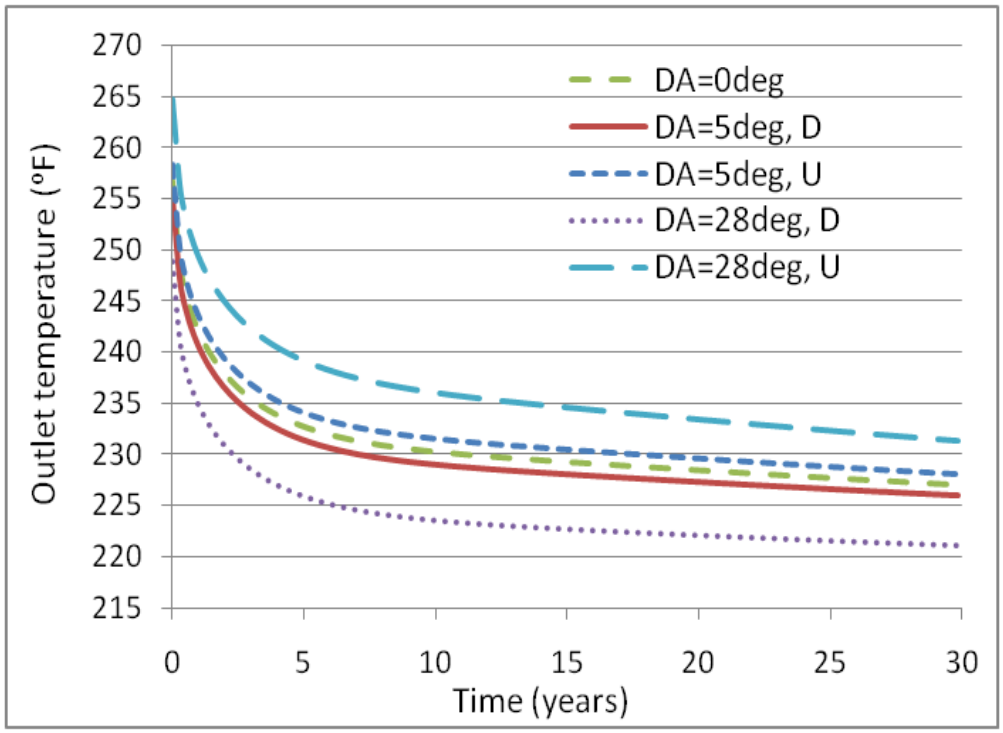

Figure 4.9: Working fluid temperature variation vs. time for different dip angles and geofluid flow directions, where DA represents dip angle; U and D are defined as updip and downdip, respectively.

For the configuration with 0^o dip angle, no difference is observed for shallower and deeper reinjection locations. For the same dip angle, higher heat extraction rate is achieved for

shallower reinjection scenario. That is because DHE is located in a deeper zone with higher temperature geofluid produced. Figure 4.10 shows the temperature contour for each scenario. For the deeper reinjection case, the cold geofluid injected will be store in the bottom layer of the geothermal reservoir. Contrarily, the cold geofluids will flow toward to DHE.

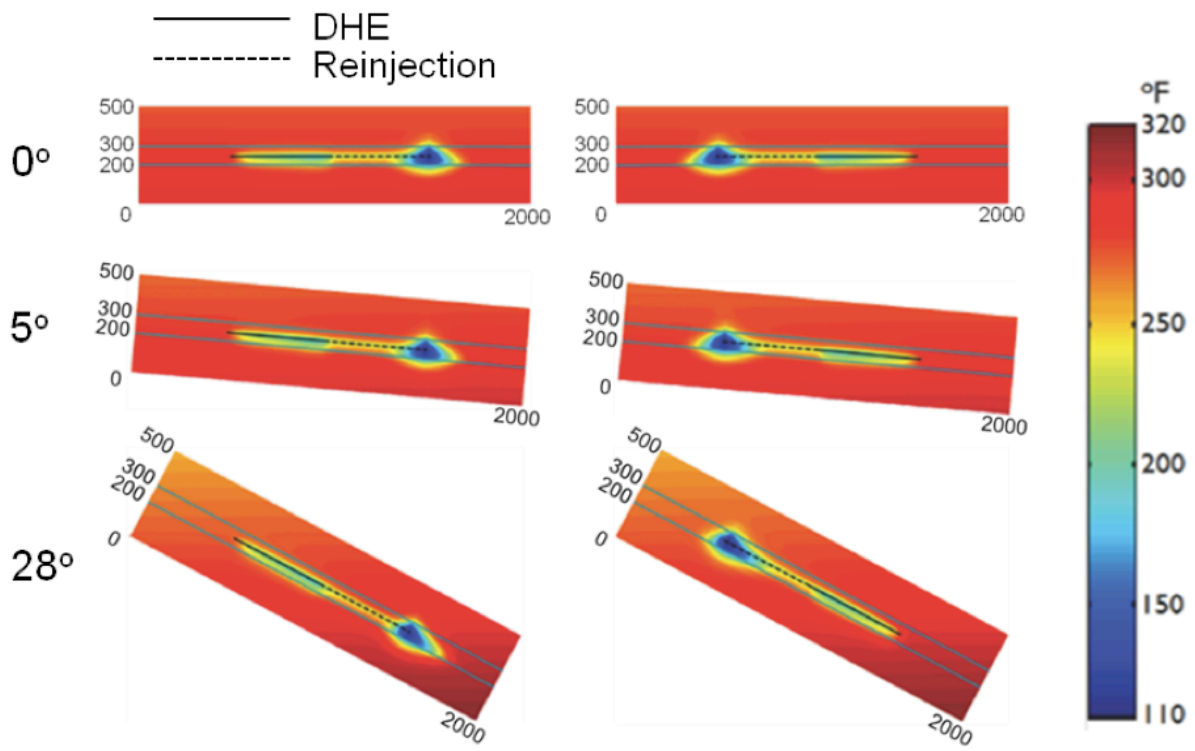

Figure 4.10: Temperature contours in the x-z plane (y=1000m) containing DHE [top: 0^o; middle: 5^o; bottom: 28^o and left: downdip ; right: updip]. The solid line represents DHE section and the geofluid is reinjected through dash line further away.

DHE Length

Additionally, the DHE can be setup along the diagonal of the computational model to allow longer DHE length of 800m and the reinjection distance of 1000m. Figure 4.11 shows the temperature variation vs. time. Average temperature difference of the two configurations is estimated as 14^oF, equivalent to 113kW thermal power and 33kW electricity power. Figure 4.12 shows the temperature contours of the diagonal plane in the presented configuration.

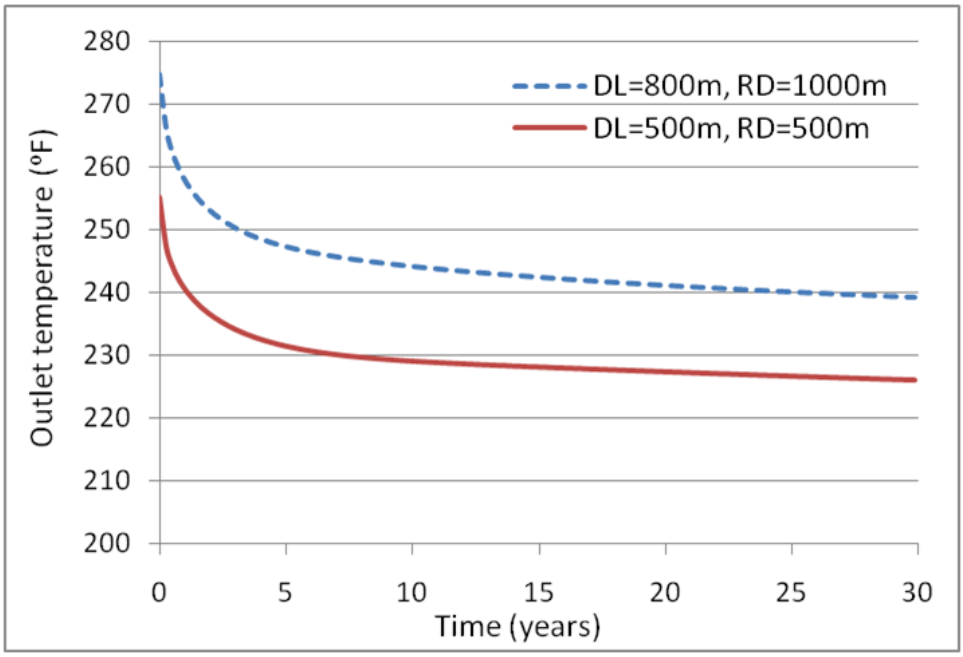

Figure 4.11: Working fluid temperature variation vs. time for longer DHE and reinjection distance, where DL and RD represent DHE length and reinjection distance, respectively.

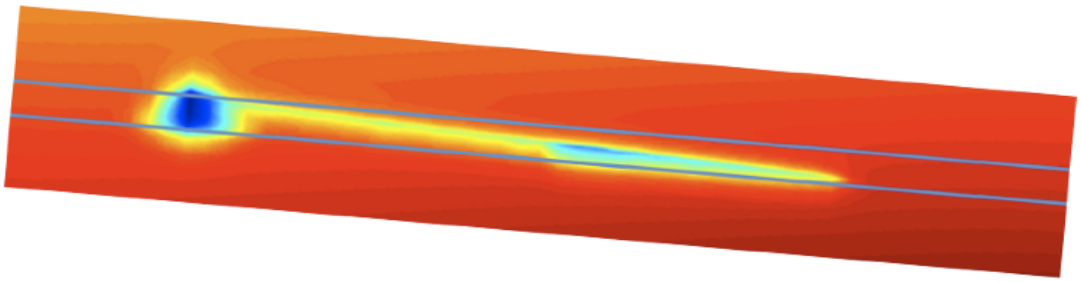

Figure 4.12: Temperature contours on the diagonal plane in the computational model.

Chapter 5
Hot Dry Rock (HDR) Geothermal Reservoirs

In this chapter, we present a few case studies for the geothermal resources lacking natural fluid and/or permeability.

5.1 Conceptual HDR Models

Hot Dry Rock (HDR) is also called Enhanced Geothermal System (EGS) which was determined economically unsuccessful during the early attempts. As of the year 2007, hydrothermal reservoir is the only geothermal system for commercial electricity generation (reported by DOE, 2008). However, there are many geothermal reservoirs containing high temperature that are lacking formation fluid and permeability.

In a HDR project, because of low permeability and the absence of natural fluid, hydraulic fracturing must be carried out to create a large sweep volume of the target reservoir. Once the reservoir reaches desired volume and permeability, multiple wells are drilled to the reservoir and a closed loop well system is constructed whereby cold fluid is pumped down from injectors and returned to the surface through the producers after being heated by the HDR reservoir (Figure 1.2).

In this proposed HDR model, an injector is at lower left corner of the reservoir boundary with injection rate of 2000 bbl/day at a constant temperature of 100^{o}F, and a producer is implemented at the upper right corner of the simulation domain. Dimensions of HDR reservoir are $1000ft \times 1000ft \times 1ft$ and fractures are assumed to be fully penetrated in the reservoir layer (Figure 5.1). Boundary and initial conditions are given below.

BC: No flow boundaries for both flow and heat transport.

IC: A constant temperature of 300^{o}F distributed everywhere, in the simulation domain.

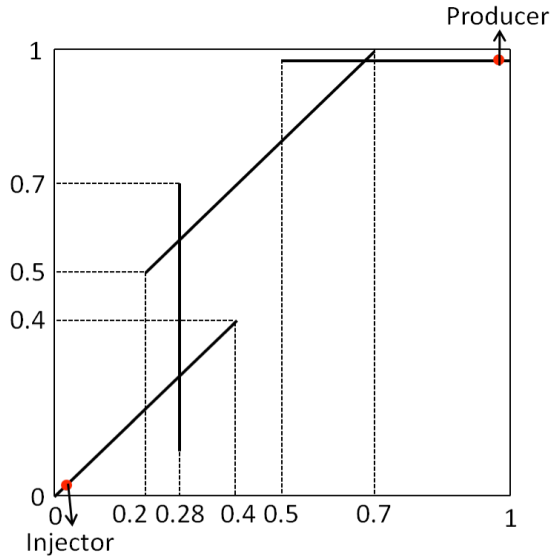

Figure 5.1: Fracture network geometry for a HDR model.

Simulation results for the heat production rates for variable fracture aperture widths (0.05 mm, 0.1 mm and 0.2 mm) are presented in Figure 5.2. The continuum model (CM) results are compared against the DFN simulation results (Svensson, 2001).

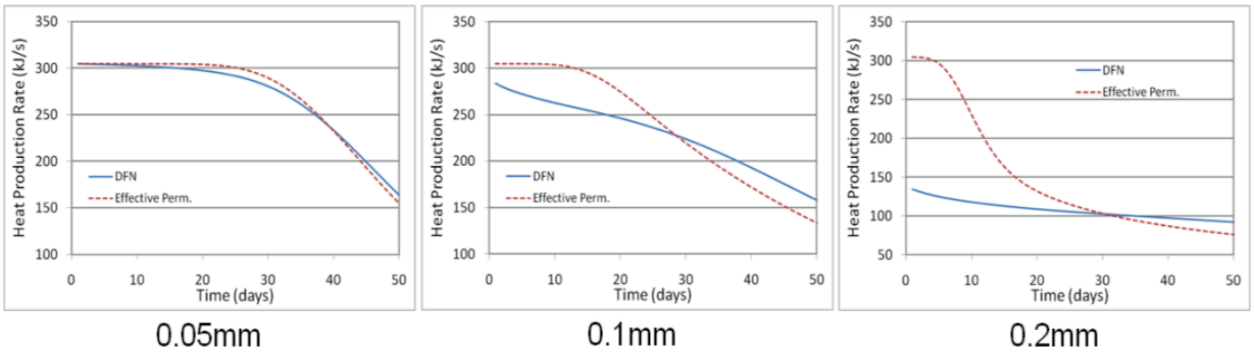

Figure 5.2: Comparison of DFN with CM on heat production rate for the fracture apertures of 0.05 mm, 0.1 mm and 0.2 mm.

For the heat production rate with larger aperture, the CM results are much higher compared to DFN in the initial period. Breakthrough time predicted by CM is also longer than that of DFN. As production goes on, the heat production rates calculated by CM encountered a sharp decrease due to the early breakthrough of the cold fluid. Beyond this time, the production rates predicted by CM is lower than the DFN results, because the formation keeps cooling further in the vicinity of fracture system.

Figure 5.3 shows the temperature contours for aperture widths of 0.05mm, 0.1mm, and 0.2mm, respectively. Top, middle and bottom rows present the simulation results at time interval of 10 days, 30 days, and 50 days, respectively. Comparing the results, it is observed

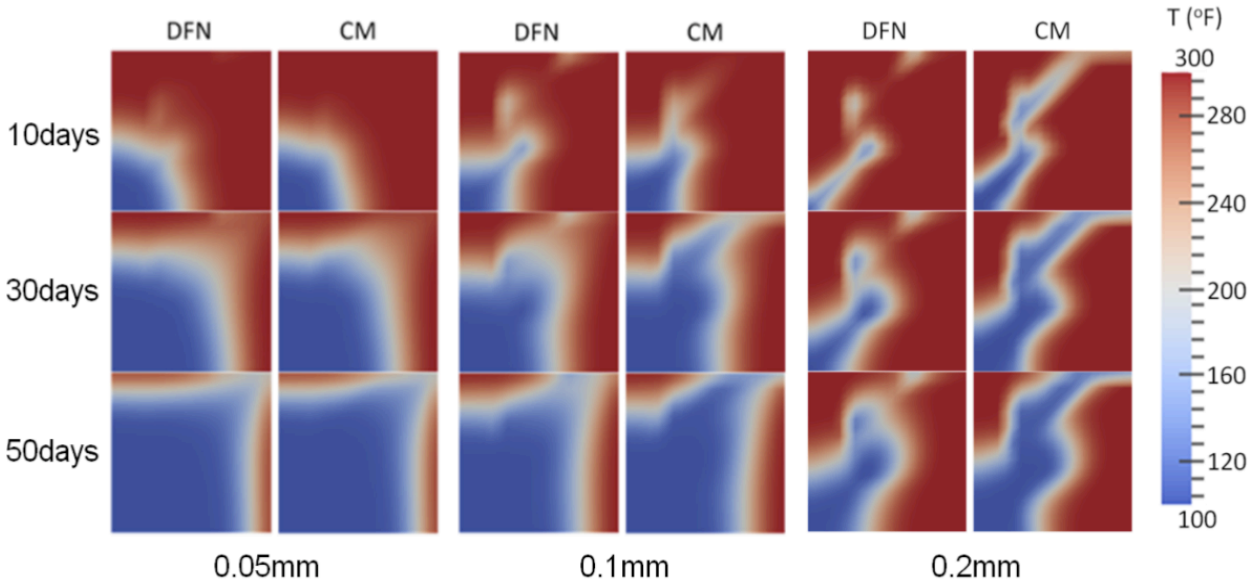

Figure 5.3: Comparison of DFN with CM on temperature pattern for the fracture apertures of 0.05 mm, 0.1 mm and 0.2 mm, after simulation times of 10 days, 30 days and 50 days.

that both methods produce similar results for the smaller aperture width (0.05mm). From temperature contours for larger aperture width (0.2mm), the thermal drainage volume predicted by DFN method is smaller compared to CM results. In addition, DFN temperature values are higher in the region close to the fracture compared to CM values. For fracture system with the large aperture width, the heat transport mechanism is dominated by the

flow path. In another words, most of the fluid flows through the fracture without much interaction with the surrounding porous media. Since DFN method represents fracture geometry explicitly, it can physically represent the above stated phenomena.

5.2 V&V Tests for HDR Modeling

5.2.1 Theoretical Results

For a V&V case of single fracture model, the fracture is modeled long the bottom boundary of the reservoir (Bower et al., 1998). The reservoir is 50m high and 1000m long with a

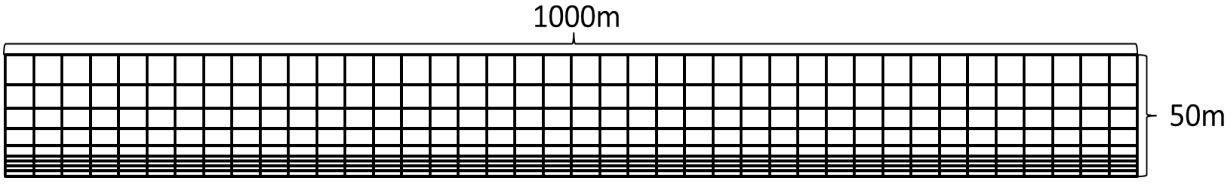

Figure 5.4: Sketch of the computational model (Bower et al., 1998) with vertical exaggeration = 2.

unit thickness, and has an initial temperature of 100^oC. The left boundary of the fracture is subjected to a constant flow rate of 6.152×10^{-3}kg/sec per unit thickness of the reservoir. The initial fracture injection fluid temperature was 90^oC. Calculated results are compared with both analytical solution of Gringarten et al. (1975) and dual porosity finite element solution presented by Bower et al. (1998), and are shown in Figure 5.5. Although both numerical solutions match the analytical solution satisfactorily, the results obtained by our simulator are closer to the analytical solution.

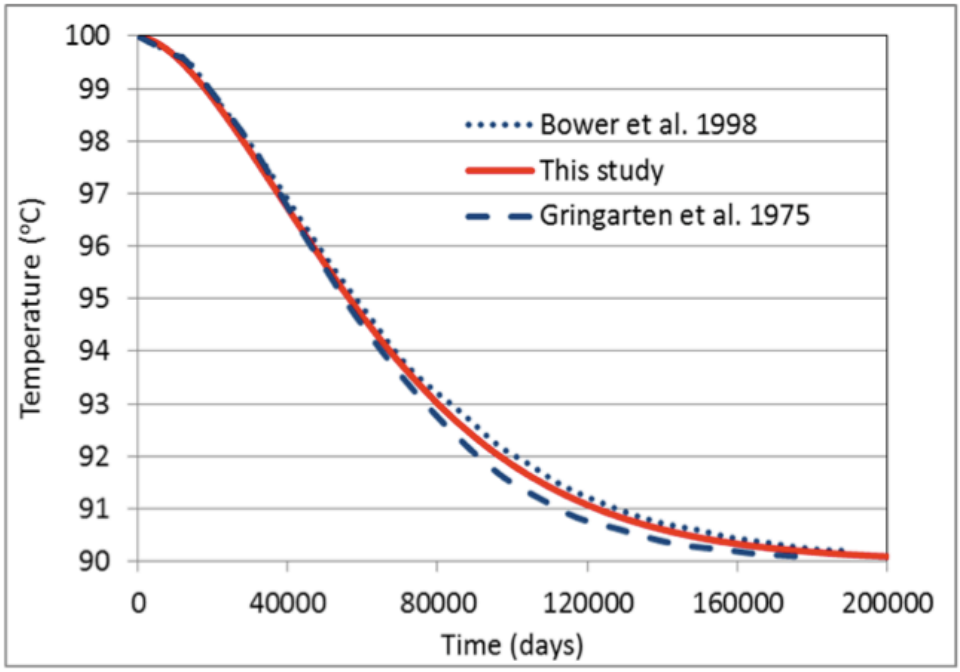

Figure 5.5: Comparison of computed results against analytical and numerical solutions, where analytical solution is introduced by Gringarten et al. (1975) and results are provided by Bower et al. (1998). Larger dash curve is analytical solution; smaller dash curve is finite element results with timestep of 4800 days; solid red curve presents the results in this study with timestep of 5000 days.

5.2.2 Fenton Hill (Phase I)

Phase I of Fenton Hill was a field test case of HDR geothermal reservoir in low permeability crystalline rock. The site is located on the edge of the Valles Caldera at the northern end of the Rio Grande rift zone in north-central New Mexico (Tester et al., 1979).

Figure 5.6 shows a simplified sketch of the fracture connection of Fenton Hill, where, the whole system consists of a main vertical fracture connected with injector and several small fractures connecting main fracture to the producer. It was interpreted that a connection was made at the depth of 2673m with average distance of 100m between the two wells. In this study, one connecting fracture is modeled between the major fracture and producer. Tester and Albright (1979) suggested an effective heat exchange area of $8000m^2$. On the 24th day,

the injection rate is doubled, from 8×10^{-3} to $1.6 \times 10^{-2} m^3/sec$.

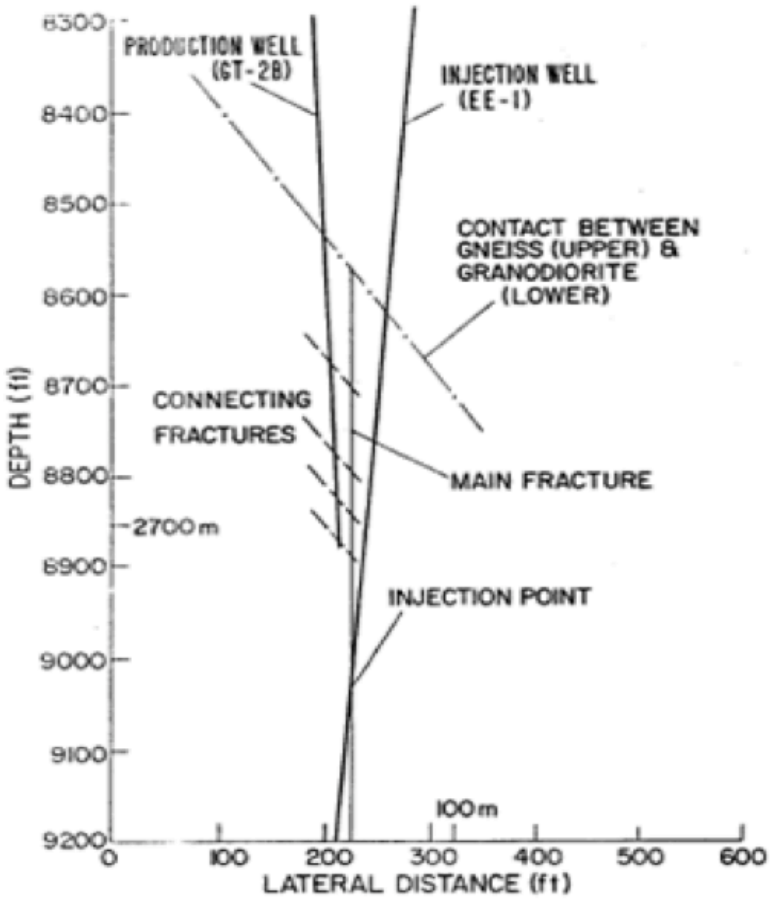

Figure 5.6: Schematic of connected fracture system in Fenton Hill (Tester et al., 1979).

Our simplified model simulation results can predict the degree of thermal drawdown after 80 days (Figure 5.7). However, it underestimates the initial production temperature. The possible explanation for this discrepancy is the fracture system itself could be unstable at beginning. For a HDR reservoir, cold water injected can induce "thermal cracking", that can generate many small fractures that are not modeled.

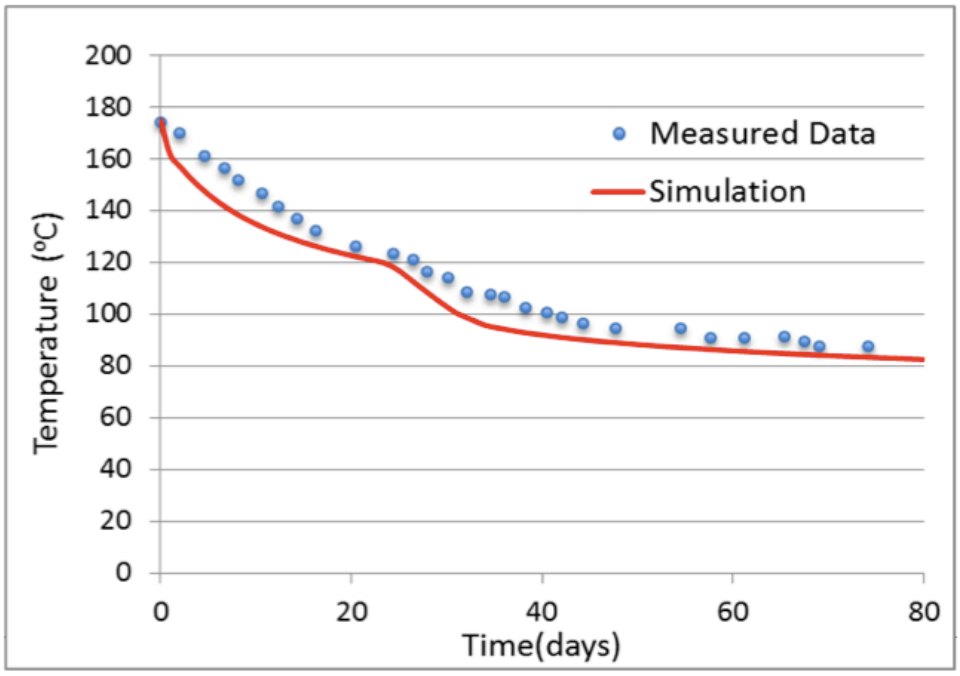

Figure 5.7: Comparison of computed results against measured data.

5.3 Using DHE Concept in EGS Configuration

5.3.1 DHE Modeling

Figure 5.8 shows a schematic for EGS configuration, where the DHE can be implemented in the horizontal section of the producing well. Five parallel evenly spaced fracture systems are shown as green arrows along the injector horizontal well. A downhole pump will be required to maintain the circulation of water to the connected fracture between the pair of the lateral wells. The vertical section of the producer well, a working fluid (n-butane) is circulated through inner annulus and tubing of the DHE. Outer annulus of DHE collects the heated water from the fractures.

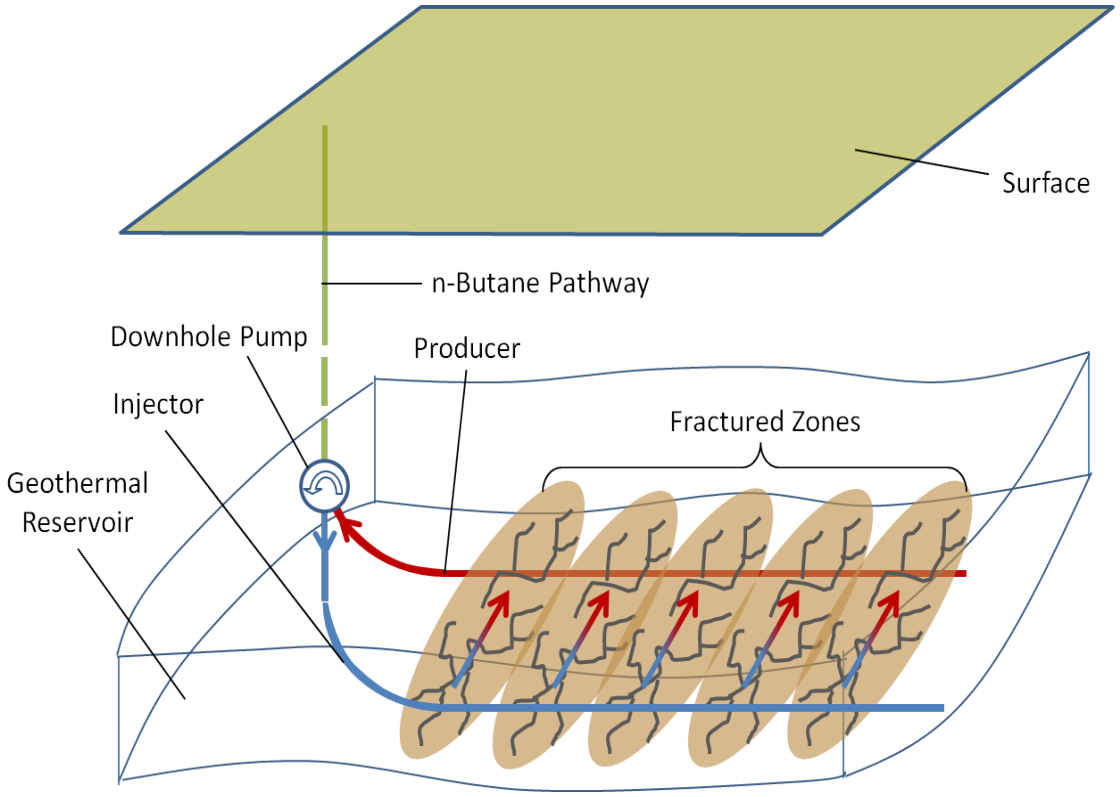

Figure 5.8: Sketch of the DHE concept in horizontal well EGS configuration (Adapted from Macartney (2011)).

DHE (located in producer wellbore, as shown in Figure 5.9) consists of two casings and one tubing to form three fluid pathways (two annuli and one tubing). Cold water is injected into the fracture network through injector horizontal well, and it gains heat from surrounding rock. The heated water is collected in the outer annulus of the producer wellbore through the connected fractures. The working fluid (n-butane) is injected through inner annulus, exchanges heat from water in outer annulus, and returns to surface through the tubing. The "spent" water is pumped back into the fracture network from injector instead of producing it to the surface. Tubing is insulated to avoid any undesired heat loss from working fluid.

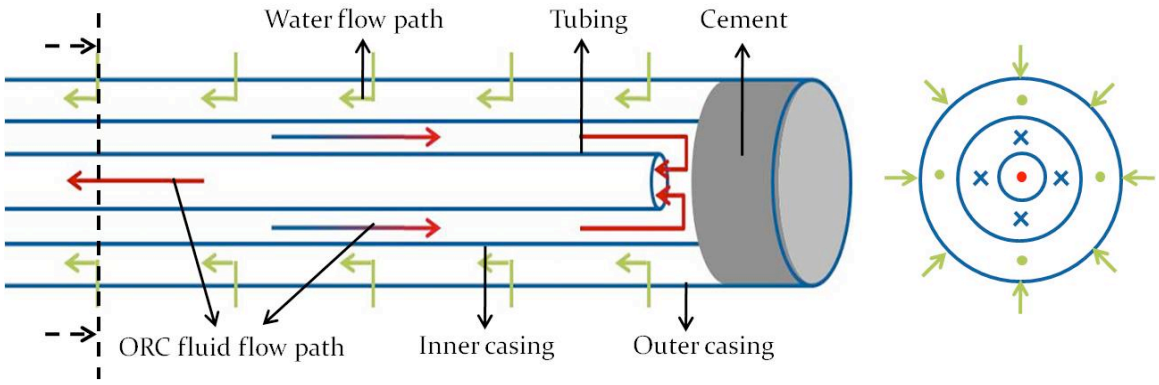

Figure 5.9: Schematic of the DHE flow paths for EGS configuration.

Assuming that the convection effect dominated the heat transfer inside the tubing and annuli, the steady state governing equations could be summarized as:

Tubing:

$$c_{wf}\dot{m}_{wf}\frac{\partial T_t}{\partial x} = -\frac{T_{a1} - T_t}{R_{at}} \tag{5.1}$$

Annulus I:

$$c_{wf}\dot{m}_{wf}\frac{dT_{a1}}{dx} = \frac{T_{a2} - T_{a1}}{R_{aa}} + \frac{T_t - T_{a1}}{R_{at}} \tag{5.2}$$

Annulus II:

$$c_w\dot{m}_w\frac{dT_{a2}}{dx} = -\frac{T_e - T_{a2}}{R_{fa}} - \frac{T_{a1} - T_{a2}}{R_{aa}} \tag{5.3}$$

where, T, c, $\dot{m}$, R, A and ρ stand for temperature, specific thermal capacity, mass flow rate, thermal resistance, cross-section area and density, respectively. Subscripts w, wf, t, a1, and a2 represent water, working fluid (n-butane), tubing, inner annulus, and outer annulus, respectively. See Chapter 3 for the definitions of R_{fa} R_{aa} and R_{at}.

5.3.2 Parametric Sensitivity Study

Several sensitivity studies were carried out to analyze the performance of DHE in the EGS configuration. The baseline parameters used are shown in Table 3.1. Parameters that are varied in this study are: heat exchanger length, working fluid flow rate, water flow rate through connected fractures, and the number of connected fractures.

(1) DHE Length

The working fluid temperature in the DHE is sensitive to the length of DHE (Figure 5.10), because a longer DHE provides a larger heat exchange area. As shown in Figure 5.10, the outlet working fluid temperature is increasing from 213^{o}F to 268^{o}F as the heat exchanger length increased from 500ft to 2000ft.

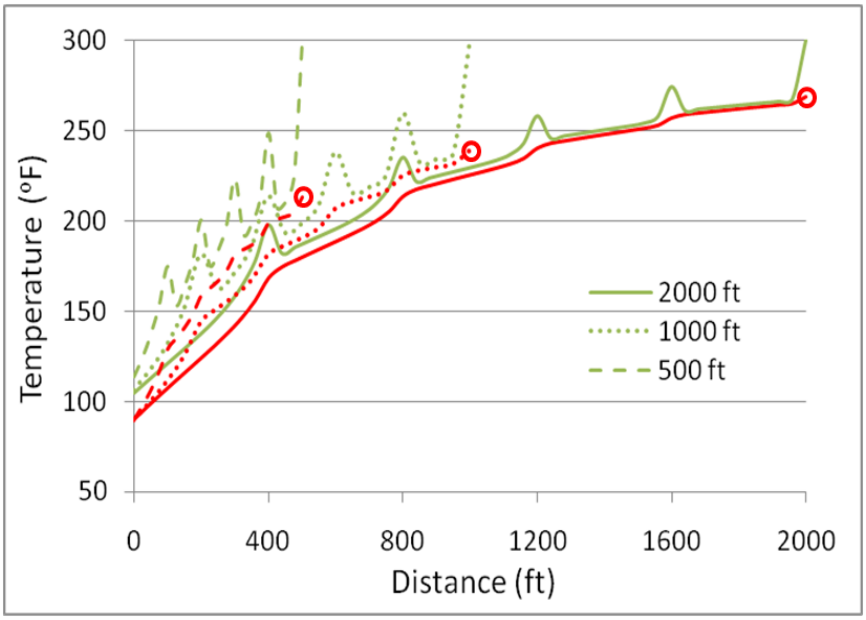

Figure 5.10: Temperature variation along flow path in DHE for different heat exchanger lengths [2000ft, 1000ft and 500ft] (red curve: working fluid (n-butane) in the inner annulus; green curve: water in the outer annulus).

(2) Working Fluid Mass Flow Rate

A decrease in working fluid outlet temperature is observed with increasing mass flow rate. The amount of heat extracted by the working fluid in the DHE can be calculated as $\dot{m}_{wf}c_{wf}(T_{wf}^{out} - T_{wf}^{in})$. For a given injection temperature, outlet temperature alone dose not determine the overall exchanged heat.

As noted in Figure 5.11, the outlet working fluid temperature is decreasing from 291^{o}F to 178^{o}F as mass flow rate increased from 2.63kg/s to 10.5kg/s. However, the amount of

heat extracted by working fluid increased from 0.81MW to 1.41MW with increasing mass flow rate.

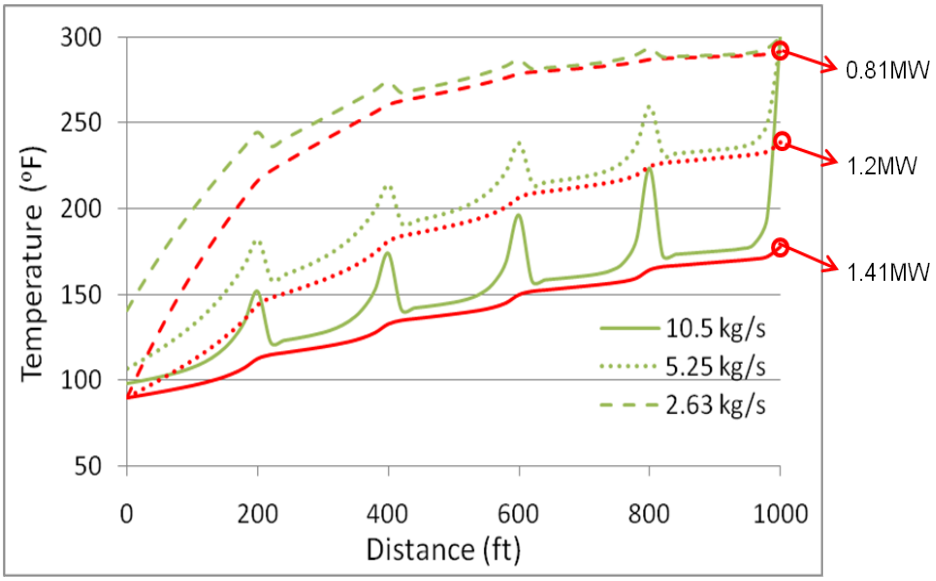

Figure 5.11: Temperature variation along flow path in DHE for different working fluid mass flow rates [10.5kg/s, 5.25kg/s and 2.63kg/s].

(3) Water Mass Flow Rate

Larger water mass flow rate can further enhance heat transfer efficiency and amount of heat in the system, to increase the overall heat extraction rate by DHE. However, the electricity consumed to drive the downhole pump could be a major problem, especially for reservoirs without good fracture connections. Modeling of the injector is out of the scope of this work and therefore, overall heat extraction by DHE is the only objective function.

It is noted in Figure 5.12, the outlet working fluid temperature is increasing from 203^{o}F to 282^{o}F as water mass flow rate increased from 1.17kg/s to 4.68kg/s. And the amount of heat extracted by working fluid increased from 0.92MW to 1.56MW with increasing mass flow rate.

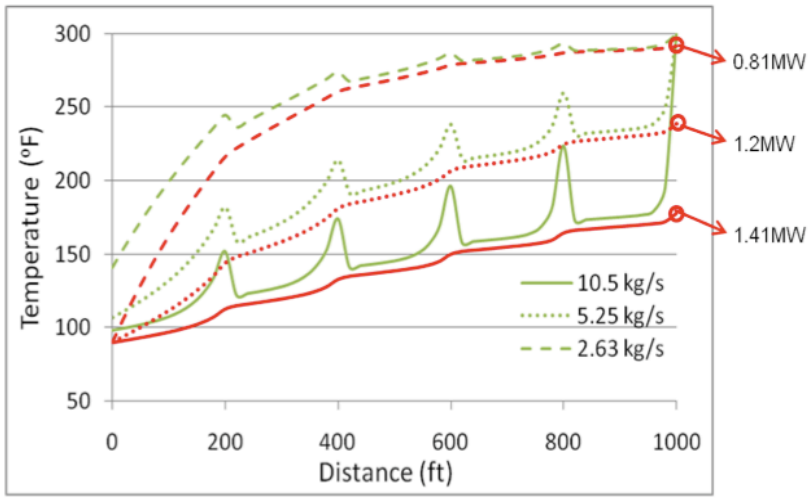

Figure 5.12: Temperature variation along flow path in DHE for different water mass flow rates [4.68kg/s, 2.34kg/s and 1.17kg/s].

(4) Number of Connected Fractures

Water enters into the outer annulus of DHE through connected fractures between the reinjected section of producer and injector wells. Hence, the number of connected fractures implies the number of inflow path for hot water into the outer annulus of the DHE. In this sensitivity study, three scenarios are provided (Figure 5.13). Equal interval is designated between any two fractures. The total water circulation rate is evenly distributed to each fracture.

As shown in Figure 5.14 (red curve), the highest n-butane temperature at the outlet of the DHE can be achieved when only one fracture exists. However, single fracture with high flow rate would apply a lower entry temperature of water in the reinjected section, because the heat exchange surface area between fracture and formation is decreasing proportional to the number of fractures.

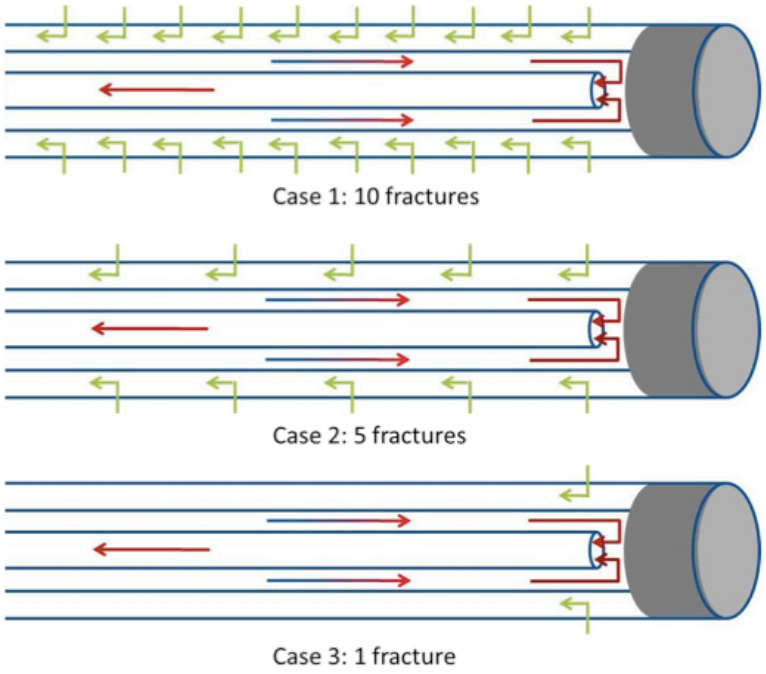

Figure 5.13: Schematic of three fracture connection scenarios.

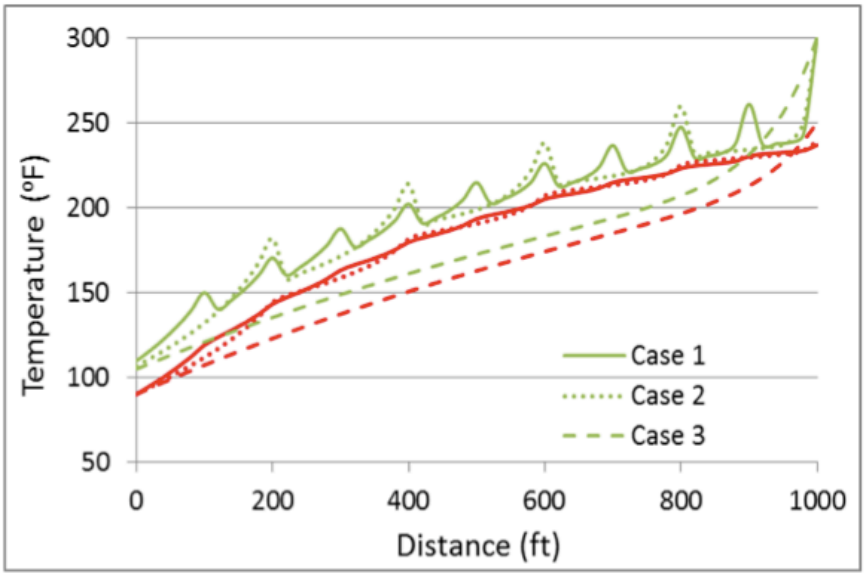

Figure 5.14: Temperature variation along flow paths for different number of connected fractures.

5.4 Thermodynamic Analysis of Producer Well

The thermodynamic study is based on the following assumptions: 1) the power plant is considered under steady state condition. 2) pressure drops through surface pipeline and condenser are negligible. 3) kinetic and potential energy at the surface facilities are negligible. 4) fresh water thermodynamic chart are used for brine properties.

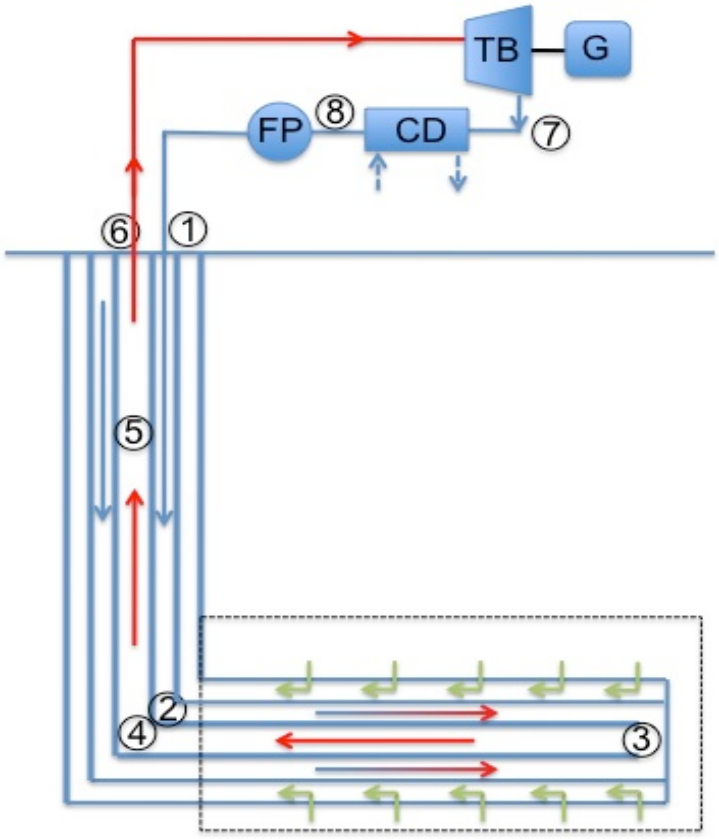

Figure 5.15: Schematic of a binary cycle linked with the presented DHE (FP-feed pump, TB-turbine, CD-condenser, numbers 1-8 represent state numbers).

As shown in Figure 5.15, working fluid is injected through the tubing from the surface in liquid phase (1). From (2) to (3) in DHE, it remains liquid phase due to the high pressure. In the returning path of the annulus, the pressure will decrease. Once the pressure drops below the vapor pressure at a certain depth, phase change will occur and working fluid (n-butane) vapor can then be collected at surface to drive the turbine and generate electricity (6-7).

Next, the working fluid returns back to liquid phase after it passes the condenser (7-8) and then is reinjected into DHE (8-1).

Thermodynamic analysis is conducted on the basis of equations and procedures presented in Chapter 3. The results are summarized in Table 5.1.

Table 5.1: Thermodynamic properties with state numbers referring to Figure 5.15.

State no.	Temperature T (^oF)	Pressure P (MPa)	Enthalpy h (kJ/kg)	Entropy s (kJ/kg^{o}K)	Exergy rate $\dot{E}$ (kW)
0	25	0.1	328	5.32	0
1	32	0.4	-23	4.02	191.1
2	32	13.2	-16	3.97	306.1
3	110	13.1	188	4.57	438.4
4	110	13.1	188	4.57	438.4
5	110	1.85	431	5.27	619
6	110	1.43	453	5.36	593.7
7s	61	0.3	386	5.36	241.9
7	67	0.3	396	5.39	247.8
8	32	0.3	-23.2	4.02	189.9

In the case, the turbine outlet pressure is set at 0.3 MPa to ensure that the fluid remains in vapor phase in, and a pump will be needed to increase pressure at state 8 to state 1. The power generated by turbine is 299kW. Assuming feed pump isentropic efficiency (0.75%) and designed working fluid mass circulating rate of 5.25 kg/s, the electricity required to drive the pump is estimated as 1.1kW. The turbine exergy efficiency is calculated to be 86% and fluid pump efficiency is near 100%. The resulting thermodynamic efficiency of DHE in producer well is 28%.

5.5 Field Case Study for DHE Concept in EGS-Raton Basin

The Raton Basin, located in southern Colorado and northern New Mexico, is recognized as a hot basin at shallow depths (Figure 5.16). According to Morgan (2009), much of the Raton Basin has geothermal gradient in the range of $2.2 - 3.3^oF/100ft$ $(40 - 60^oC/km)$, and local

geothermal gradients can exceed $3.3^oF/100ft$. At the depths of 6500-8200ft (2000-2500m), it appears to be a good candidate for binary power plant for electricity generation. Our

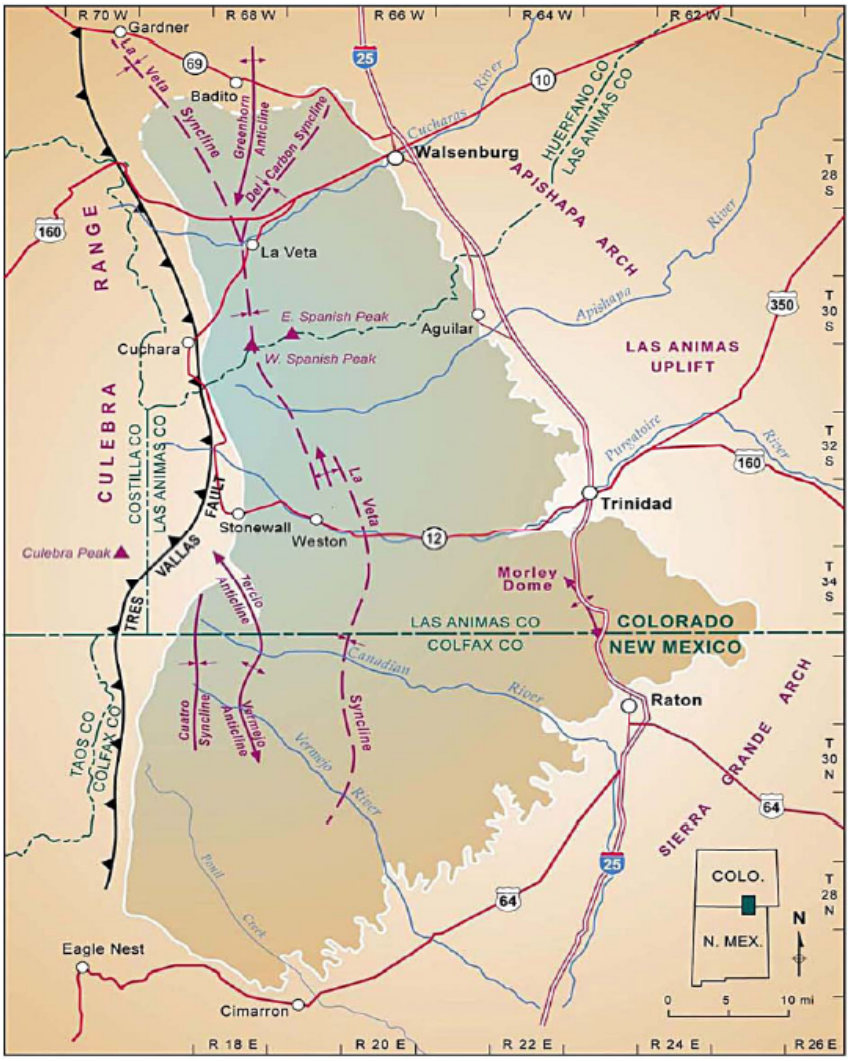

Figure 5.16: Map of the Raton Basin (Morgan, 2009).

computational model is setup according to the pilot project description of Pioneer Natural Resources (Macartney, 2011). The geothermal pilot is located at the depth of 8000ft with reservoir temperature around 300^oF and geothermal gradient of $3.9^oF/100ft$. As shown in Figure 5.17, cold water is injected through injector well, and hot water is produced through connected producer well. In the heat exchanger, the binary fluid is heated and evaporated to generate electricity.

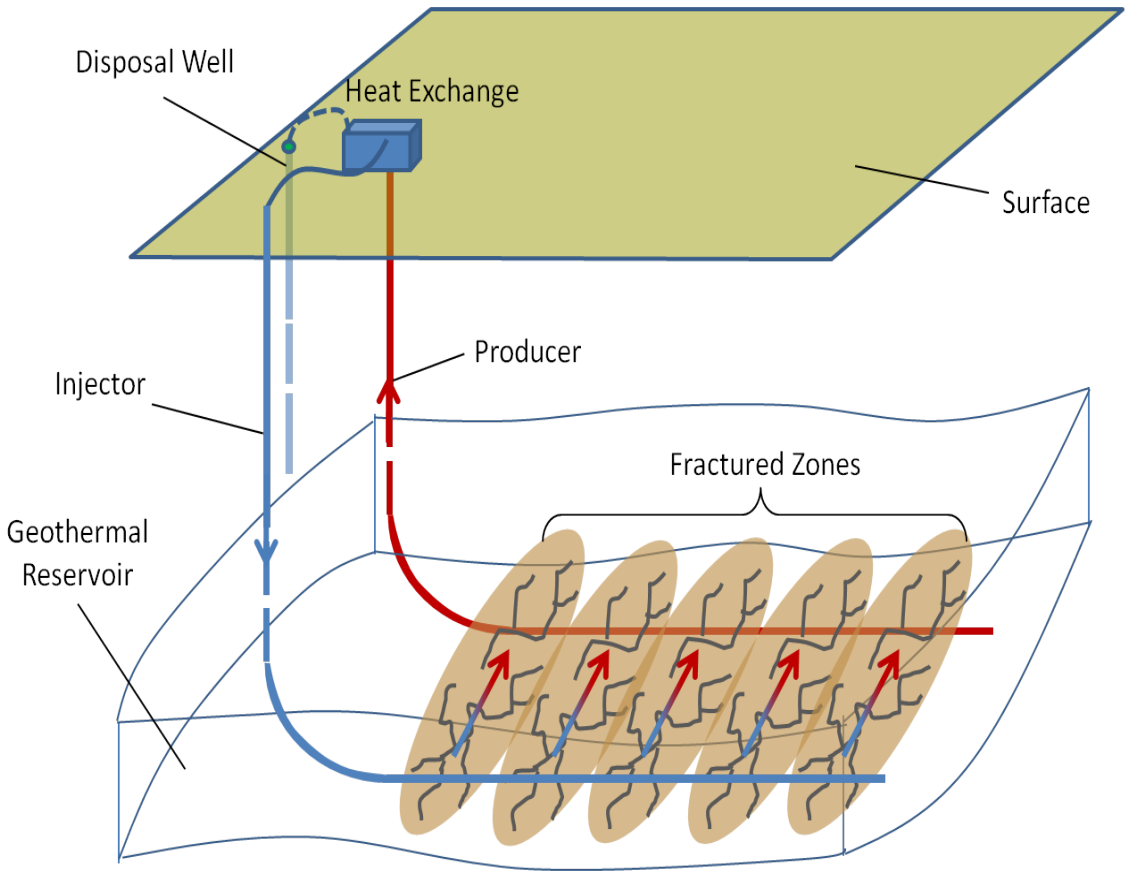

Figure 5.17: Sketch of the Pioneer's pilot project (Adapted from Macartney, 2011).

Similar to the saturated geothermal resources, the DHE presented in previous section is setup in the horizontal well section of producer. This configuration is different from saturated geothermal reservoir case study because the water flux into DHE occurs through connected fractures at possibly different temperatures and flow rates in various sections along this DHE.

In this study, the computational domain, with dimension of $1000m \times 500m \times 500m$, is initialized to $(3.9^oF/100ft$ $(70^oC/km)$ geothermal gradient with top boundary temperature set at 330^oF (166^oC). Water and binary fluid (n-butane), surface injection temperatures are 104^oF (40^oC) and 77^oF (25^oC), respectively.

As shown in Figure 5.18, five connected fractures, with uniform aperture width of 0.000656ft (0.2mm), with even spacing of 328ft (100m) are implemented. and the distance between injector and producer is 328ft (100m). The water injection rate is 10000bbl/day, and the parameters used for working fluid (n-butane) are given in Table 3.1.

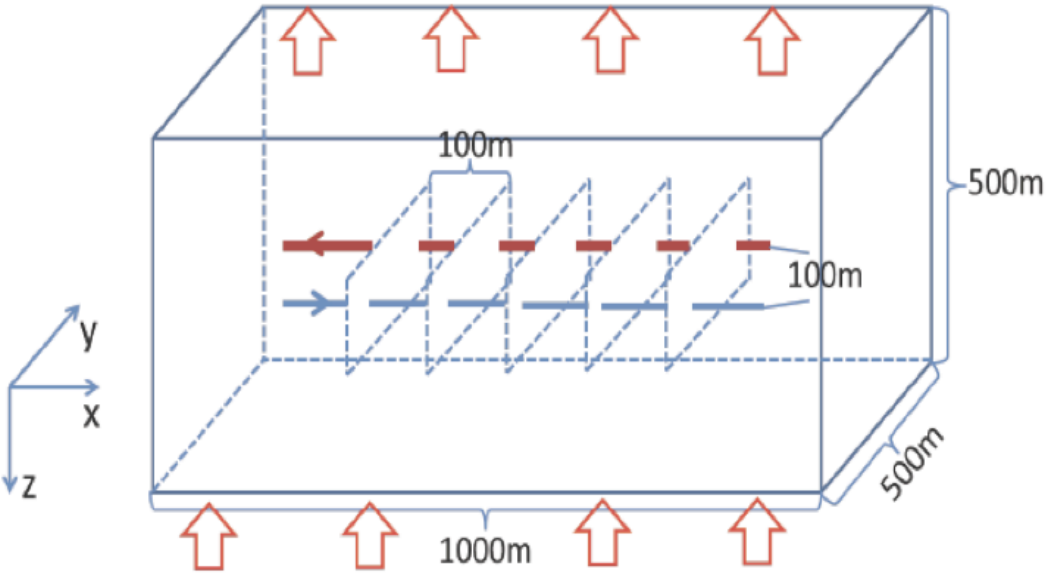

Figure 5.18: Sketch of the computational model for the geothermal pilot project.

According to MIT report (2006), the overall thermal efficiency is:

$$\eta_{th} = 0.0935 T_{in} - 2.3266 \tag{5.4}$$

where, T_{in} is inlet temperature in ^oC and efficiency is in percent. Consequently, for the pilot project, the electricity power output can be calculated from water inlet/outlet temperature and mass fluid rate. Figure 5.19 shows the comparison results of two case in electricity power, which presents an improved sustainability by using DHE in EGS exploration.

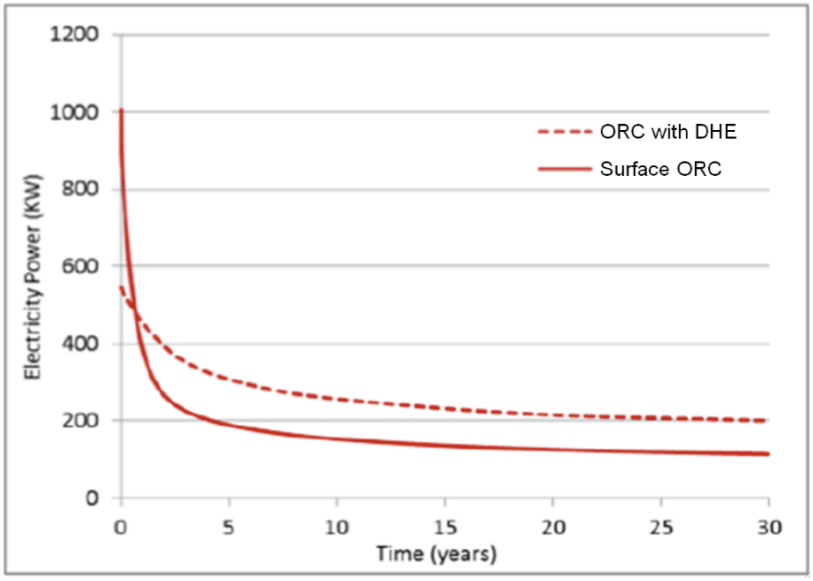

Figure 5.19: Electricity generation v.s. time for full surface ORC and ORC with DHE.

Chapter 6
Discussions

Two waterflooding models were simulated to test the implementation of DFN method for the fracture representation, where the first test was for fracture orientation effects, and the second one was for fracture network connectivity. Extracting heat from geothermal reservoirs is not similar to the fluids displacement process as in oil and gas industry applications in many ways. For a waterflooding problem, water is injected to drive the oil towards the producers to enhance the secondary recovery rate. Based on the material balance, it can be imagined that if water break through at producers is delayed for longer time, more oil will be produced. In geothermal engineering, longer working fluid residual time would correspond to more heat extracted.

During waterflooding, there are many pathways from injector to producer. Based upon the fluid and rock properties, only a few of pathways may dominate the overall fluid transport rates and flood patterns. Fractures are highly conductive pathways with a precise direction along its orientation. When the direction of water front is aligned with the fracture orientation, most of the fluid would flow easily inside the fracture compared to porous rock matrix. In this case fracture works as a shortcut and dramatically reduces the breakthrough time for displacing fluid to reach the producer wells. However, when the direction of water front is perpendicular to the fracture orientation, there is no significant contribution by the fracture and most flow happens inside the porous matrix.

Two configurations of a novel DHE design were introduced in Chapter 3. For the first DHE configuration (geofluid is injected through tubing, hence GFT), the working fluid can possibly be heated in both forward and returning flow paths by the formation and circulation of

the hot geofluid, respectively. It can also potentially gain heat from both sides (formation and tubing). However, the outlet temperature of working fluid was observed to be lower than the second configuration (working fluid is injected through tubing, WFT) which extracts heat only from the outer annulus. Consider the thermal resistance for the given parameters are $R_{fa} = 16R_{at} = 28R_{aa}$, where, R_{fa}, R_{at}, and R_{aa} stand for the thermal resistances between formation and outer annulus, inner annulus and fluid inside tubing, and outer annulus and inner annulus, respectively. However, to avoid heat loss during the working fluid return flow path, inner casing is insulated for the first configuration (large enough R_{aa}), and tubing is insulated for the second configuration which gives a large R_{at}. In the first design, the most conductive component (R_{aa}) is insulated and hence increases the overall thermal resistance. This leads to decrease in the heat extraction rates.

From the results comparison for the two DHE configurations, the geofluid temperatures at DHE exit are 169^{o}F) for the first configuration, and 104^{o}F for the second one. Lower output temperature for the second configuration implies that more heat was exchanged between geofluid and working fluid in this configuration. For the long term development, the residence time of the reinjected geofluid could be a potential issue. However, this can be resolved by extending the reinjection distance of geofluid completion from the DHE.

Parametric studies show the DHE behaviors is sensitive to DHE length, working fluid (n-butane) flow rate and geofluid (brine) flow rate, which provides three controls to improve the DHE performance. Increasing DHE length enhances the heat exchange area and prolong the residence time; higher working fluid flow rate can contribute towards increasing the forced convection heat transfer mode; and higher geofluid flow rate would bring more heat into the system. However, longer DHE would increase capital investment and while higher geofluid flow rates would increase the re-injection pump power consumption.

Based on simulation results for the field case study corresponding to Camerina A geothermal reservoir, the presented DHE design with the extended reinjection section improved the heat extraction rate and sustainability over the life cycle of 30 years. However, the scenarios that place DHE at a deeper zone with cold geofluid reinjected to the shallower zone performs better on heat extraction rate because of the higher inlet temperature of the produced brine. However, the re-injected cold geofluid is heavier and sinks due to gravity along the slope in the dipping system.

A conceptual HDR model is studied in Chapter 5.1 to compare results produced by different fracture representation method (Continuum Method vs. DFN). Simulated results for flow patterns are sensitive to fracture aperture widths. From the comparative study, continuum model (CM) and DFN produce significantly different results for a larger fracture aperture width due to flow channelling effect instead of diffusion in porous media. Similar results were observed for smaller fracture aperture (0.05 mm) for both continuum and DFN methods implying that the continuum method can handle the system with a large number of small fractures, for example, natural fractures. For EGS, the fracture apertures considered are larger than natural fractures, and therefore, the fluid flow path were determined by these engineered fracture networks.

Two verification and validation tests were conducted to exam the capability of developed simulator for solving EGS applications. DHE with multiple inlets in the outer annulus is designed for EGS development. Each inlet connects with a fracture intersecting the wellbore containing the DHE. The water flows into the fractures and gains heat from the rock matrix. It enters DHE through inlets on the outer casing. Effect of the number of inlets on the working fluid exit temperature is also studied.

The DHE concept is introduced for an EGS development of a tight sedimentary geothermal reservoir (Raton Basin) and the preliminary results obtained for electricity generation capacity look promising. However, the circulation of water in the fractured reservoir is driven by a down hole pump that could possibly limit the DHE efficiency. As an example, for a small fracture aperture system (0.1mm), and a higher water circulation rate, the pumping costs are expected to increase dramatically.

Developed simulator has several limitations. Darcy's law and cubic law were employed for porous media and fractures, respectively. However, high flow rate as expected in the near wellbore region is not considered in this study. Inertial flows are expected to increase the downhole pump power consumption and should not be neglected. To further improve the performance of this simulator for complex DHE completions, the implementations of Forchheimer flow in fractures and non-Darcy effect in the near wellbore regions are recommended.

Chapter 7
Conclusions

A geothermal reservoir simulator is developed to solve for fluid/heat transport processes in fractured porous media: fluid flow solution in fracture and porous media is fully coupled and implicit, energy conservation equation is explicit in time using the calculated velocity field. Several verification and validation cases are presented to test the predictive capability of the simulator for the problems involving natural convection in porous media (Costa, 2006; Sathiyamoorthy et al., 2007), effect of dip angle (Baez and Nicolas, 2007), fracture orientation and network representation (Karimi-Fard and Firoozabadi, 2003; Karimi-Fard and Durlofsky, 2004). All cases showed satisfactory comparison of simulated results against the corresponding published results. Further capabilities of this simulator such as parallel code performance and incorporation of capillary forces are also reported in Appendix A.

A novel downhole heat exchanger (DHE) is proposed to address the issues of handling produced geofluids, the associated cost of reinjection, and the potential risks of induced seismicity. With the advances in directional drilling technology and improvements in the tubular metallurgy, a coaxial long tubular heat exchange can be placed in the horizontal part of the well. Taking heat exchange process nearest to the reservoir improves heat exchange efficiency as well as minimizes the loss of extracted heat back to the formation. Between the two configurations of this DHE considered, the flowpath of the working fluid (n-butane) injected through tubing with return path to the surface yielded higher heat extraction rate compared to the configuration with produced geofluid flowing through the tubing and then reinjected in a farther away section of the same reservoir.

Saturated geothermal resources such as geothermal geopressured brine (GGB) and hot saline aquifers (HSA) present an opportunity to exploit low-enthalpy power generation systems provided the heat exchangers can efficiently extract the heat from formation at a sustained economic rate over the entire project life without adding any environmental risks. A conceptual HSA model is simulated to understand the natural convection effect on the thermal drainage pattern. Parametric studies are carried out to understand the sensitivity of heat extraction rate to DHE length, n-butane flow rate and brine flow rate. A field case study corresponding to Camerina A geothermal resource is presented to demonstrate the sustainability of heat extraction using DHE. Locating spent geofluid reinjection completion farther away from heat exchanger region improved the heat extraction rate and sustainability over the designated life cycle of 30 years.

Lastly, the concept of placing DHE in geothermal reservoir is extended for enhanced geothermal systems (EGS). Typical EGS would be challenging for directional drilling. However, a tight sandstone reservoir (Raton Basin) could be exploited using heat exchangers in long horizontal wellbores. To address the issues of low permeability and no geofluid, a horizontal injector with hydraulic fractures connecting to the horizontal producer is proposed. Simulated results indicated that heat extraction sustainability can be achieved by using DHE due to its higher heat exchange efficiency (in reservoir condition) and larger heat exchange area (long horizontal wellbore).

Geomechanical equilibrium equations, phase change of the geofluid/working fluid, high rate flow effects in complex completions, as well as brine geochemistry (precipitation/dissolution reactions) should be developed further in the future extensions of the developed geothermal reservoir simulator.

Bibliography

Alkhasov, A.B., Aliyev, R.M., Ramazanov, M.M. and Abasov, G.M., Study of complex heat exchange with account for phase transitions in secondary contour of the geothermal power plant, Renewable Energy 19, 155-161 (2000)

Aziz, K. and Swttari, A., Petroleum Reservoir Simulation, Society of Petroleum Engineers, (1979)

Baez, E. and Nicolas, A., Natural convection fluid flow and heat transfer in porous media, Journal of Mechanics of Materials and Structures, 2, (2007)

Barbier, E., Nature and technology of geothermal energy: A review, Renewable and Sustainable Energy Reviews, Elsevier, (1998)

Barbier, E., Geothermal energy technology and current status: an overview, Renewable and Sustainable Energy Reviews, Elsevier, (2002)

Barbosa, R., Discrete element models for granular materials and rock masses, Ph.D. thesis, Department of Civil Engineering, The University of Illinois at Urbana-Chamagn, (1990)

Barenblatt, G.I., Zheltov, I.P., and Kochina, I.N., Basic concepts in the theory of seepage of homogeneous liquid in fissured rock, J. Appl. Math. Mech., 24, 1286-1303 (1960)

Batzle, M. and Wang, Z., Seismic properties of pore fluids, Geophysics, 57, 1396-1408 (1992)

Bear, J., Tsang, C.F. and Marsily, G., Modeling flow and contaminant transport in fractured rock, Academic Press, New York, 1-37 (1993)

Bloomfield, K., Moore, J.N., and Neilson, R.M., Geothermal energy reduces greenhouse gases, Geothermal Research Council, GRC Bulletin, (2003)

Bower, K.M. and Zyvoloski, G., A numerical model for thermo-hydro-mechanical coupling in fractured rock, Int. J. Rock Mech. Min. Sci., 34, 1201-1211 (1997)

Boyle, G., Renewable Energy: Power for a Sustainable Future, Second Edition, Oxford University Press, (2004)

Chen, N.H., An explicit equation for friction factor in pipe, Ind. Eng. Chem., Fundamentals 18, (1979)

Chen, Z., Reservoir Simulation: Mathematical Techniques in Oil Recovery, Society for Industrial and Applied Mathematics, Philadelphia (2007)

Christie, M.A. and Blunt, M.J., Tenth SPE comparative solution project: a comparison of upscaling techniques, SPE 66599, (2001)

Costa, V.A.F., Unified streamline, heatline and massline methods for the visualization of two-dimensional heat and mass transfer in anisotropic media, International Journal of Heat and Mass Trans., 46, 1309-1320 (2003)

Costa, V.A.F., Bejans heatlines and masslines for convection visualization and analysis, Appl. Mech. Rev., 59, 126-145 (2006)

Cringarten, A.C., Witherspoon, P.A., and Ohnishi, Y., Theory of heat extraction from fractured hot dry rock, Journal of Geophysical Research, 80, (1975)

Cutright, B.L., The potential of geothermal energy, Geothermal Energy Utilization Associated with Oil & Gas Development (2009)

Dershowitz, B., LaPointe, P., Eiben, T., and Wei, L., Integration of discrete feature network methods with conventional simulator approaches, SPEREE, 165 (2000)

Dipippo, R., Geothermal Power Plants: Principles, Applications, Case Studies and Environmental Impact, ELSEVIER, (2008)

El-Khamra, Y., Real-time reservoir characterization and beyond: cyberinfrastructure tools and technologies, a Master's thesis submitted to the graduate faculty of Louisiana State University (2009).

Feng, Y., Tyagi, M., and White, C.D., Effect of natural convection patterns of optimal locations and size of a heat sink in a geothermal reservoir, Proceedings of Thirty-Sixth Workshop on Geothermal Reservoir Engineering, Stanford, CA, (2011)

Geothermal Technologies Market Report, U.S. DOE (2009)

Ghia, U., Ghia, K.N., and Reynolds, W.C., High-Re solutions for incompressible flow using the Navier-Stokes equations and a multigrid method, J. Comput. Phys. 48, 387 (1982)

Grant, M.A. and Bixley, P.F., Geothermal Reservoir Engineering (the second edition), Elsevier (2011)

Gray, T.A., Geothermal resource assessment of the Gueydan salt dome and the adjacent southeast Gueydan field, Vermilion Parish, Louisiana, a Master's thesis submitted to the graduate faculty of Louisiana State University (2010)

Griggs, J., A re-evaluation of geopressured-geothermal aquifers as an energy resource, a Master's thesis submitted to the graduate faculty of Louisiana State University (2004)

Gringarten, A.C., Witherspoon, P.A., and Ohnishi, Y., Theory of heat extraction from fractured hot dry rock, Journal of Geophysical Research, 80, 1120-1124 (1975)

Huenges, E. and Ledru, P., Geothermal Energy Systems: Exploration, Development, and Utilization, Wiley-VCH (2010)

John, C.J., Maciasz, G., and Harder, B.J., Gulf coast geopressured-geothermal program summary report compilation, work performed under U.S. Department of Energy Contract No. DE-FG07-95ID13366, (1998)

Juliusson, E. and Horne, R.N., Study and simulation of tracer and thermal transport in fractured reservoirs, Proceedings of Thirty-Fifth Workshop on Geothermal Reservoir Engineering, Stanford, CA, (2010)

Kagel, A., Bates, D., and Gawell, K., A guide to geothermal energy and the environment, Geothermal Energy Association (2007)

Karimi-Fard, M. and Firoozabadi, A., Numerical simulation of water injection in fractured media using the discrete-fracture model and the Galerkin method, SPE paper 83633, (2003)

Karimi-Fard, M. and Durlofsky, L.J., An efficient discrete-fracture model applicable for general-purpose reservoir simulators, SPE paper 88812 (2004)

Karimi-Fard, M., Gong, B., and Durlofsky, L.J., Generation of coarse-scale continuum flow models from detailed fracture characterizations, WRR, 42, (2006)

Kay, W.B., Pressure-volume-temperature relations for n-Butane, Ind. Eng. Chem., 32(3), 358-360 (1940)

Kehle, R.O., Geothermal survey of North America, Annual Progress Report, (1972)

Kohl, T. and Hopkirk, R.J., A simulation coede for forced fluid flow and transport in fractured porous rock, Geothermics, 24, 333-343 (1995)

Kolditz, O., Gorke, U., Shao, H., and Wang, W. Thermo-Hydro-Mechanical-Chemical Processes in Fractured Porous Media, Springer, (2012)

Lee, S.H., Jensen, C.L., and Lough, M.F., Efficient finite-difference model for flow in a reservoir with multiple length-scale fractures, SPE paper 65095 (2000)

Lee, S.H., Lough, M.F., and Jensen, C.L., Hierachical modeling of flow in naturally fractured formations with multiple length scales, Water Resources Research, 37, 443 (2001)

Li, L. and Lee, S.H., Efficient field-scale simulation of black oil in a naturally fractured reservoir through discrete fracture networks and homogenized media, SPE paper 103901 (2008)

Lund, J.W., The use of downhole heat exchangers, Geothermics 32, 535-543 (2003)

Macartney, H.H. and O'Farrell, C.R., A Raton Basin geothermal prospect, AAPG, Durango, CO, (2010)

Majer, E., Overview of induced seismicity in geothermal systems, Berkeley Lab (2009)

McCain, W.D., Reservoir fluid property correlations-state of the art, SPE Reservoir Engineering, 6, 266-272 (1991)

Merewether, E.A., Plays for oil and gas in the Raton Basin, south-central Colorado and northeastern New Mexico, report for U.S. Geological Survey, (1987)

McClure, M.W. and Horne, R.N., Discrete fracture modeling of hydraulic stimulation in enhanced geothermal systems, preceedings of thirty-fifth workshop on geothermal reservoir engineering, Stanford, CA, (2010)

An MIT-led interdisciplinary panel, The future of geothermal energy, (2006)

Moinfar, A., Narr, W., Hui, M., Mallison, B., and Lee, S.H., Comparison of discrete-fracture and dual-permeability models for multiphase flow in naturally fractured reservoirs, SPE paper 142295 (2011)

Morgan, P., A preliminary analysis of geothermal resources in the Central Raton Basin, Colorado, from bottom-hole temperature data, AAPG Annual Convention, Denver, Colorado, (2009)

Nalla, G., Shook, G.G., Mines, G.L., and Bloomfield, K., Parametric sensitivity study of operating and design variables in wellbore heat exchangers, Workshop on Geothermal Reservoir Engineering, Stanford University, Stanford, CA (2004)

Nield, D.A. and Bejan, A., Convection in Porous media, second edition., Springer Inc., New York (1998)

Patankar, S.V. and Spalding, D.B., A calculation procedure for heat, mass and momentum transfer in three-dimensional parabolic flows, Int. J. Heat and Mass Transfer (1972)

Patankar, S.V., Numerical Heat Transfer and Fluid Flow, Hemisphere Publishing Corporation, New York (1980)

Peaceman, D.W., Interpretation of well-block pressures in numerical reservoir simulation, SPE J., 18 (3), 183-194 (1978)

Plaksina, T., Modeling effects of coupled convection and CO_2 injection in stimulating geopressured geothermal reservoirs, a Master's thesis submitted to the graduate faculty of Louisiana State University (2011).

Pritchett, J.W., STAR: A geothermal reservoir simulation system, Proceedings: World Geothermal Congress, Florence, (1995)

Pruess, K. and Narasimhan, T.N., A preactical method for modeling fluid and heat flow in a fractured porous media, SPE J., 25, 14-26 (1985)

Pruess, K. and Wang, J.S.Y., Numerical modeling of isothermal and nonisothermal flow in unsaturated fractured rock: a review, AGU, Special Symposium on Flow and Transport through Unsaturated Fractured Rocks, San Francisco, CA, (1986)

Pruess, K., Wang, J.S.Y., and Tsang, Y.W., On thermohyrological conditions near high-level nuclear wastes emplaced in partially saturated fractured tuff. Part 1. Simulation studies with explicit consideration of fracture effects, Water Resources Research, 26, 1235-1248 (1990)

Pruess, K., Wang, J.S.Y., and Tsang, Y.W., On thermohyrological conditions near high-level nuclear wastes emplaced in partially saturated fractured tuff. Part 2. Effective continuum approximation, Water Resources Res., 26, 1249-1261 (1990)

Pruess, K., Oldenburg, C., and Moridis, G., TOUGH2 user's guide, version 2.0, Earth Sciences Division, Lawrence Berkeley National Laboratory, CA (2011)

Ray, C., Boast, C.W., Ellsworth, T.R., and Valocchi, A.J., Simulation of the impact of agricultural management practices on chemical transport in macroporous soils, Tans. of the ASCE., 39(5), 1697-1707 (1996)

Rhie, C.M. and Chow, W.L., A numerical study of the turbulent flow past an isolated airfold with trailing edge separation, AIAA Journal 21 1525-1532 (1983))

Rossen, R.H., Simulation of naturally fractured reservoir with semi-implicit source terms, SPEJ, (1977)

Rowe, A.M. and Chou, J.C.S., Pressure-volume-temperature-concentration relation of aqueous NaCl solutions, Journal of Chemical Engineering Data, 15, (1970)

Rybach, L., How Renewable are geothermal resources?, Geothermal Resources Council Trans., Vol. 23, 563-566, (1999)

Rybach, L., Geothermal sustainability, GHC Bulletin, (2007)

Sanyal, S.K., Butler, S.J., Swenson, D., and Hardeman, B., Review of the state-of-the-art of numerical simulation of enhanced geothermal systems, Proceedings of World Geothermal Congress, Tohoku, Japan, (2000)

Sathiyamoorthy, M., Basak, T., Roy, S., and Pop, I., Steady natural convection flow in a square cavity filled with a porous medium for linearly heated side wall(s), International Journal of Heat and Mass Trans., 50, 1892-1901 (2007)

Svensson, U., A continuum representation of fracture networks. Part I: Method and basic test cases, journal of Hydrology, 250, 170-186 (2001)

Sybach, L., Megel, T., and Eugster, W.J., How renewable are geothermal resources?, Geothermal Resources Council Transactions, Vol. 23, 563-566 (1999)

Szalkowski, S.D. and Hanor, J.S., Spatial variations in the Salinity of produced waters from southwstern Louisiana, GCAGS/GCSSEPM Trans., Vol. 53, 798-806 (2003)

Tester, J.W. and Albright, J.N., Hot dry rock energy extraction field test: first 75 days of operation of a prototype reservoir at Fenton Hill, Los Alamos Scientific Laboratory Report, (1979)

Thomas, L.K., Dixon, T., and Pierson, R.G., Fractured reservoir simulation, SPEJ, 42-54 (1983)

Touma, J., Comparison of different capillary models to predict the hydraulic conductivity from the water retention curve, ISCO (2008)

U.S. DOE, Renewable energy technology characterizations, EERE (EPRI Topical Report No. TR-109496), (2005)

U.S. DOE, An evaluation of enhanced geothermal systems technology, EERE (2008)

Wang, Z., McClure M.W., and Horne, R.N., A single-well EGS configuration using a thermosiphon, Workshop on Geothermal Reservoir Engineering, Stanford University, Stanford, CA (2009)

Warren, J.E. and Root, P.J., The behavior of naturally fractured reservoirs, Soc. Petrol. Eng. J., 3, 245-255 (1963)

White, D.F. and Williams, D.L., Assessment of geothermal resources of the United States, U.S. Geological Survey Circular 726, (1975)

Witherspoon, P.A, Wang, J.S., Iwai, K., and Gale, E., Validity of cubic law for fluid flow in a deformable rock fracture, Water Resources Res., 16, 1016-1024 (1980)

Yamamoto, T., Kitano, K., Fujimitsu, Y., and Ohnishi, H., Application of simulation code, GEOTH3D, on the Ogachi HDR site, Proceedings of the 22rd Annual Workshop on Geothermal Reservoir Engineering, Stanford University, (1997)

Appendix A: Simulator Capabilities

Waterfooding Model

In the waterflooding case, the test results are demonstrated by comparing our blackoil simulator results against the Buckley-Leverett analytical solution. The relevant parameters are listed in Table A.1. Figure A.1 shows a satisfactory comparison between computed results and the analytical solution.

Table A.1: Parameters used for the waterflooding model.

S_{or}	0.2		μ_o	1	cp
S_{wc}	0.2		μ_w	1	cp
m	2		A	300	ft^2
n	2		L	1000	ft
ϕ	0.2		q_t	100	stb/days

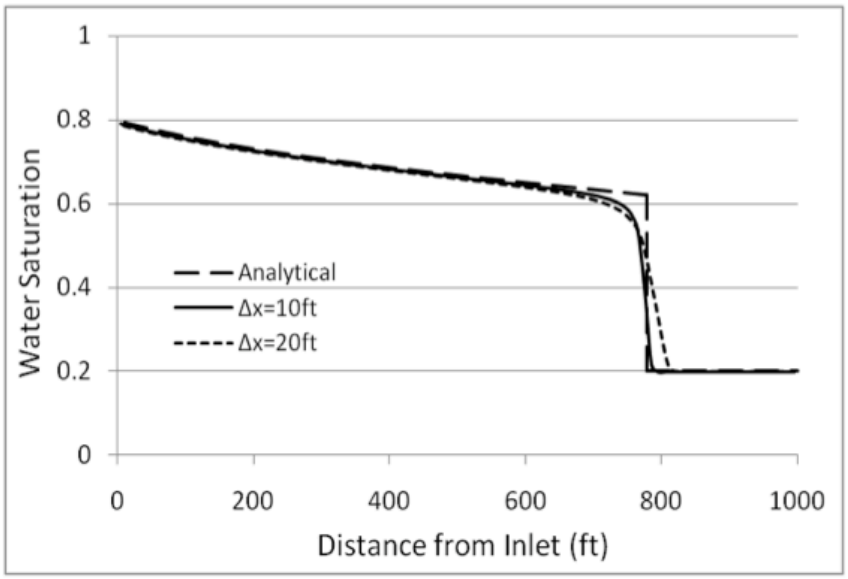

Figure A.1: Comparison of computed results against Buckley-Leverett analytical solution for water saturation after 40 days.

Gravity & Capillary Effect

This case study verifies the gravity and capillary force balance calculations in a vertical 1-D 2-Phase system. The water saturation in the system initially distributes evenly at 0.5 (half water and half air). Assuming a negligible compressibility, the water-air interface should be stable at half of the total depth due to equilibrium. Figure A.2 and Figure A.3 present the simulation results of water saturation at different grid resolutions and times. Table A.2 states the P_c-S_w relation. Using Table A.2 as input, when the system reaches equilibrium, the water saturation distribution should match the data from Table A.2, and Figure A.4 indicates the excellent simulation results.

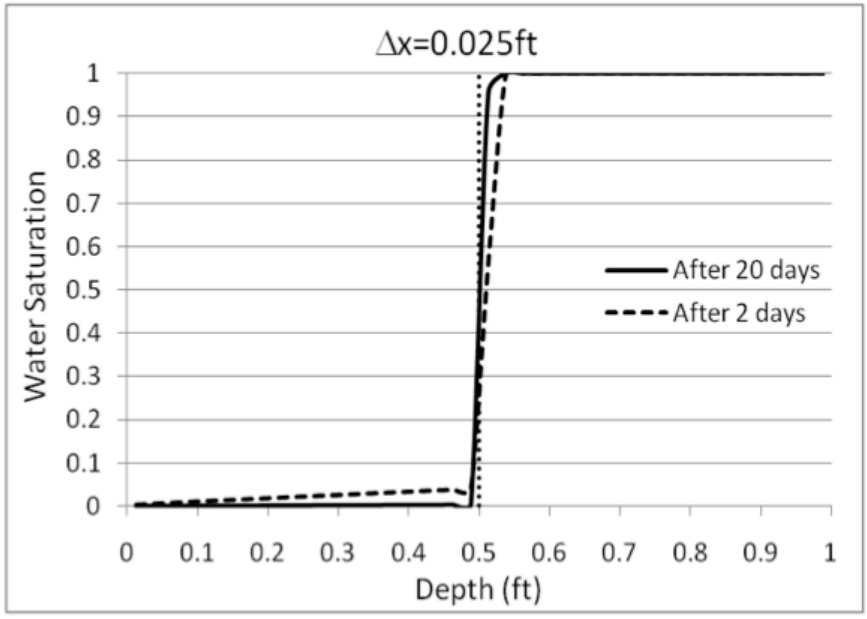

Figure A.2: Gravity induced water saturation distributions after 2 days and 20 days for the grid resolution of Δx=0.025ft.

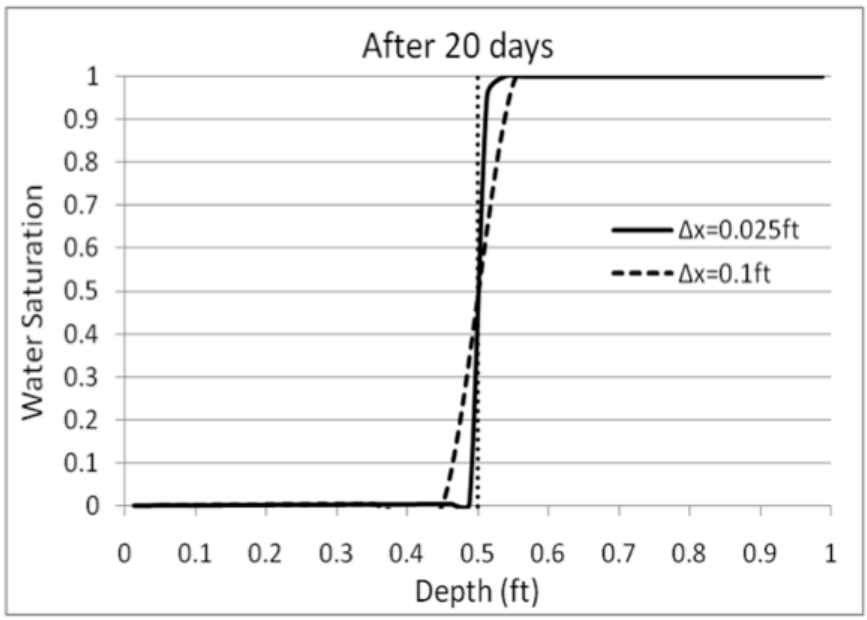

Figure A.3: Gravity induced water saturation for different grid resolutions.

Table A.2: Pc-Sw relation (Touma, 2008).

Sw	Pc
0.06	1.45
0.07	1.16
0.075	1.015
0.08	0.87
0.09	0.58
0.1	0.435
0.3875	0.29
0.642	0.2175
0.974	0.145
0.983	0.0725

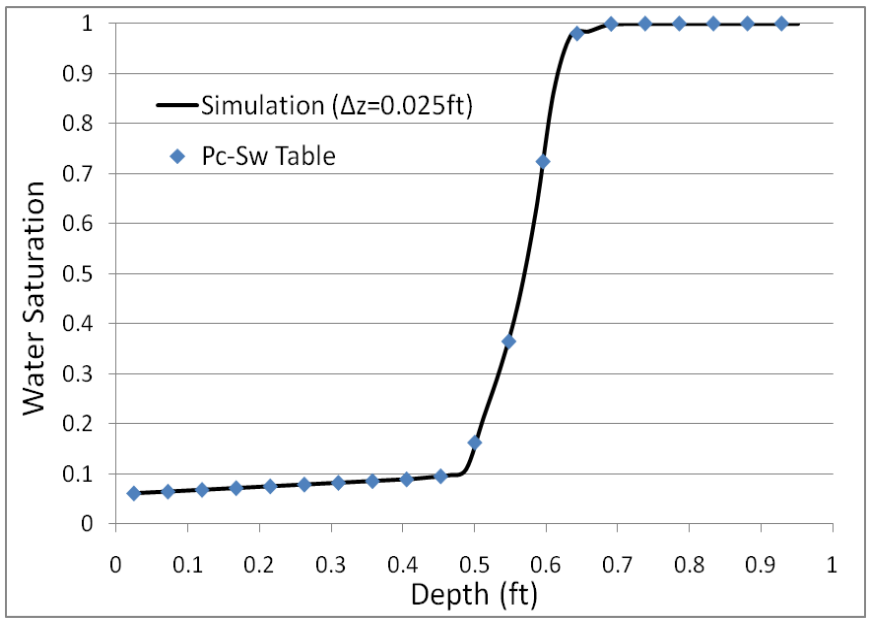

Figure A.4: Comparison results of simulation to P_c-S_w table.

SPE 10 (Comparative Solution Project)

SPE 10 is one of the serial comparative solution projects organized by Society of Petroleum Engineers (SPE), which aims to compare upgridding and upscaling approaches and the ability to predict performance of a waterflooding problem (http://www.spe.org/web/scp).

A SPE10 (Christie et al., 2001) model contains four producers in the corns with bottom-hole pressure of 4000 psia and one injector in the center of the gridblocks with a constant injection rate of 5000 stb/day. All wells were vertical and completed throughout the formation. The model dimensions are $1,200 \times 2,200 \times 170$ ft. The top 70 ft represent the Tarbert formation, and the bottom 100 ft represents Upper Ness. Figure A.5 shows the comparison results on oil production rate.

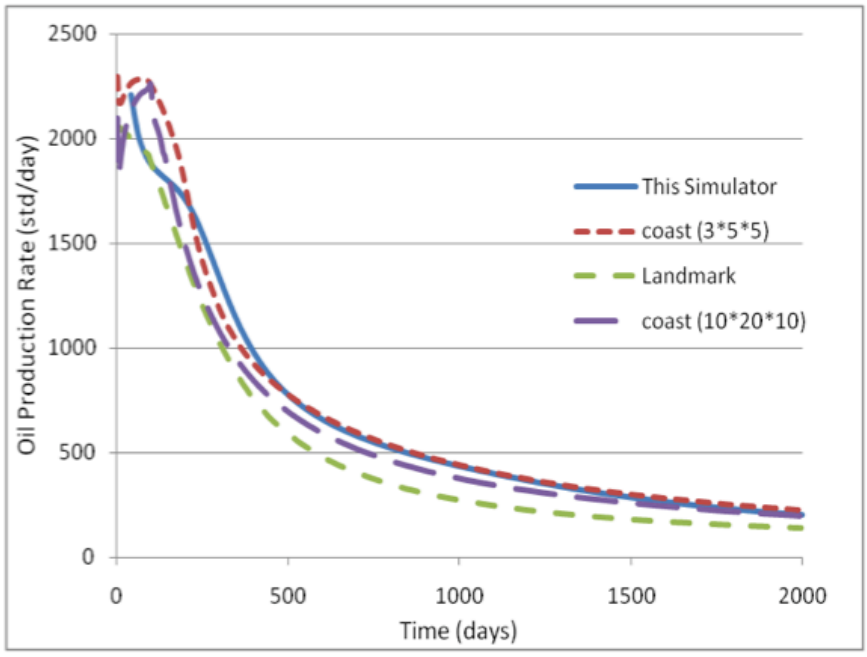

Figure A.5: Comparing oil production rates with other simulation results (Christie et al., 2001).

Parallel Performance

The following tests were conducted to show the parallel performance of the code and two types of scaling tests were conducted.

a) Strong scaling

A Strong scaling is used to show the ability of parallel computation to decrease the over all run time for a particular problem. This test was carried out on a supercomputer, Queenbee, over LONI resources, using 32, 64, 128, 256 and 512 cores and problem size is kept fixed at 4.8×10^6 gridblocks. Figure A.6 shows the result of strong scaling performance on log-log plot.

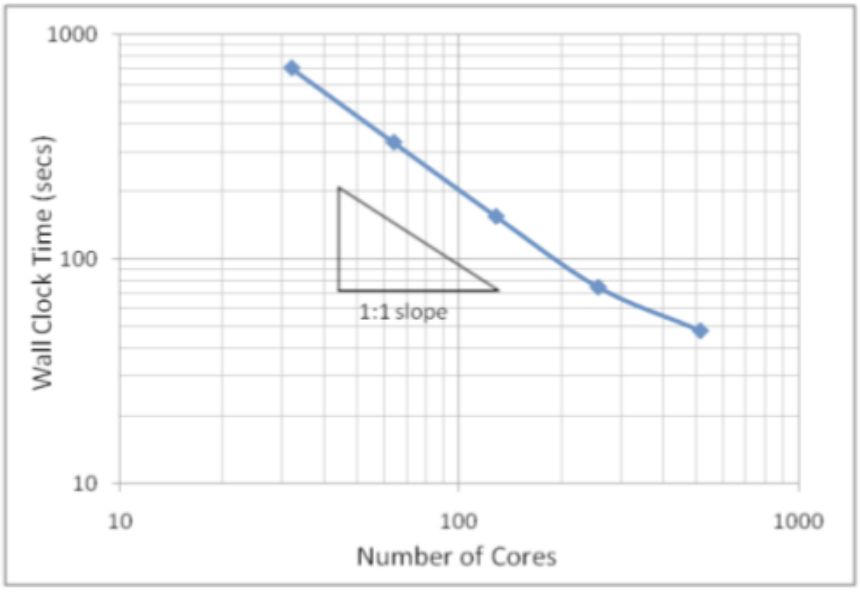

Figure A.6: Log-log plot to strong scaling performance.

b) Weak scaling

A weak scaling test is used to show the ability of parallel computation scale up a problem on more cores. Consequently, problem complexity is increased while increasing the number of cores. Table A.3 indicates the number of gridblocks for its corresponding number of cores and Figure A.7 presents the result of weak scaling performance on a log-log plot.

Table A.3: Computational cores vs. problem size.

Number of Cores	Gridblocks ($*10^3$)
32	150
128	600
512	2400
1024	4800
2048	9600

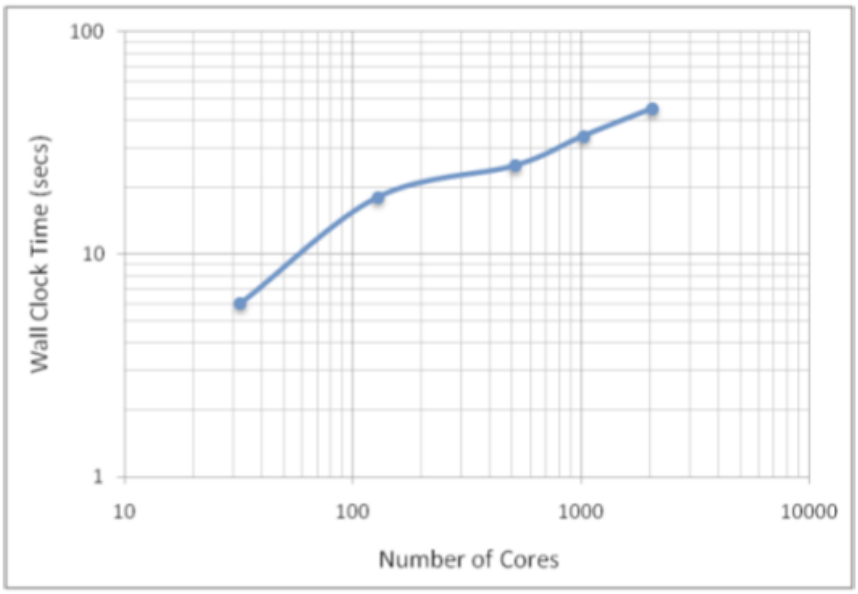

Figure A.7: Log-log plot for weak scaling performance.

Appendix B: Discretization of Transport Equation

Eq. (B.1) presents a generalized form of transport equation which can stand for both fluid flow and heat transfer equations.

$$\rho\frac{\partial\phi}{\partial t} + \rho(\nabla \cdot u\phi) - \mu\nabla^2\phi = S_\phi \tag{B.1}$$

where, ρ is the fluid density, ϕ is general variable and u stands for velocity vector. There are four terms in above equation, from left to right, they are: transient term, convection/advection term, diffusion term and source term, respectively. By droping convection term, flowing equation can be expressed. To represent energy transport, scalar variable temperature is used as general variable, and for Navier-Stokes Equations, the source term is represented as $-\nabla P$.

Finite Volume Discretization

Similar to the finite difference method for porous media, finite volume method is used to evaluate partial differential equations in the form of algebraic equations for fracture, based on which, values can be calculated at discrete places on a meshed geometry. However, one advantage of the finite volume method over finite difference method is that it supports unstructured mesh.

The governing equation for the flow in an arbitrary volume ΔV bounded by a closed surface ΔS can be described by taking integration of Navier-Stoke's Equation.

$$\frac{\partial}{\partial t}\int_{\Delta V}\rho\phi\, dV + \int_{\Delta V}(\rho(\nabla \cdot u\phi) - \mu\nabla^2\phi)\, dV = -\int_{\Delta V} S_\phi\, dV \tag{B.2}$$

By applying the divergence theorem in above equation, we have:

$$\frac{\partial}{\partial t}\int_{\Delta V}\rho\phi\,dV+\int_{\Delta S}\rho u\phi\,dS-\int_{\Delta S}\mu\nabla\phi\,dS=-\int_{\Delta V}S_{\phi}\,dV \tag{B.3}$$

where dS is the surface vector.

The transient and source therms are integrated over the cell volume, whereas, the convection and diffusion therms sum the fluxes through the control volume faces.

Transient term

$$\frac{\partial}{\partial t}\int_{\Delta V}\rho\phi\,dV=\rho\Delta V_C\frac{\phi_C^{n+1}-\phi_C^n}{\Delta t} \tag{B.4}$$

where, the subscript C represents the cell centroid.

Convection term

$$\int_{\Delta S}\rho u\phi\,dS=\int_{\Delta S}\rho u_f\phi_f\cdot n_f\,dA_f=\sum_f F_f\phi_f \tag{B.5}$$

where, subscript f means cell face, n is normal vector, A represents face area and F is the mass flux.

Diffusion term

$$-\int_{\Delta S}\mu\nabla\phi\,dS=-\sum_f\mu A_f(\nabla\phi)_f\cdot n_f \tag{B.6}$$

Source term

In the Navier-Stoke's Equation, the source term or pressure gradient term can be approximated by Green-Gauss theorem which states that the volume integral of the gradient of the

scalar function is equal to the surface integral of a scalar function.

$$-\int_{\Delta V} \nabla P \, dV = -\int_{\Delta S} P \, dS = -\sum_f P_f^{n+1} A_f n_f \tag{B.7}$$

Otherwise, the source term can be simply estimated as:

$$\int_{\Delta V} S_\phi dV = S_\phi \Delta V \tag{B.8}$$

Interpolation Schemes

From above discretization, a lot variables on surface which need to be evaluated by variables on other computational nodes. Thus, several interpolation schemes are introduced, although only upwind scheme is employed in this study.

Upwind Differencing Scheme (UDS)

Upwind scheme approximates variable at surface using the value at the node upstream. Technically, it uses a backward or forward difference approximation on the basis of flow direction. This scheme can not yield oscillation numerical diffusion will occur.

Taking Eq. (B.5) for example, using UDS, we have:

$$F_f u_f = \begin{cases} F_f u_{nb} & if \quad F_f < 0 \\ F_f u_C & if \quad F_f > 0 \end{cases} \tag{B.9}$$

Taylor series expansion gives:

$$u_f = u_C + (x_f - x_C) \left(\frac{\partial u}{\partial x}\right)_C + \frac{(x_f - x_C)^2}{2} \left(\frac{\partial^2 u}{\partial x^2}\right)_C + H \tag{B.10}$$

where, H denotes higher-order terms.

From above equation, we can see UDS is a first order scheme and the leading truncation error term $\left(\frac{\partial u}{\partial x}\right)_C$ is diffusive.

Central Difference Scheme (CDS)

CDS approximates variable at surface by linear interpolation between two neighbor nodes. For Eq. (B.5), we have:

$$u_f = (1-\lambda)u_C + \lambda u_{nb} \tag{B.11}$$

where, λ is the weigh coefficient which can be defined as $\frac{x_f - x_C}{x_{nb} - x_C}$.

Taylor series expansion gives:

$$u_f = u_{nb}\lambda + u_C(1-\lambda) - \frac{(x_f - x_C)(x_{nb} - x_f)}{2}\left(\frac{\partial^2 u}{\partial x^2}\right)_C + H \tag{B.12}$$

The CDS is a simple second order scheme and may produce oscillatory solutions. The leading truncation error term is proportional to the square of the grid spacing. According to the nature of convection, the one more point required is on the upstream side.

Quadratic Upstream Interpolation for Convective Kinematics (QUICK)

Leonard (1979) made this scheme popular and named it as QUICK which approximates variables by a parabola instead of a straight line. The general form of QUICK scheme is shown as following expressions.

$$\phi_e = \begin{cases} g_1\phi_E - g_2\phi_W + (1 - g_1 + g_2)\phi_P & for \quad u_x < 0 \\ g_3\phi_P - g_4\phi_{EE} + (1 - g_3 + g_4)\phi_E & for \quad u_x > 0 \end{cases} \tag{B.13}$$

where,

$$g_1 = \frac{(2 - \lambda_{e,W})\lambda_{e,P}^2}{1 + \lambda_{e,P} - \lambda_{e,W}} \tag{B.14}$$

$$g_2 = \frac{(1 - \lambda_{e,P})(1 - \lambda_{e,W})^2}{1 + \lambda_{e,P} - \lambda_{e,W}} \tag{B.15}$$

$$g_3 = \frac{(1 + \lambda_{e,W})(1 - \lambda_{e,P})^2}{1 + \lambda_{e,E} - \lambda_{e,P}} \tag{B.16}$$

$$g_4 = \frac{\lambda_{e,P}\lambda_{e,E}^2}{1 + \lambda_{e,E} - \lambda_{e,P}} \tag{B.17}$$

For uniform grid with $u_x > 0$, the coefficients can be calculated and the Taylor series expansion gives:

$$\phi_e = \frac{6}{8}\phi_P + \frac{3}{8}\phi_E - \frac{1}{8}\phi_W - \frac{3(\Delta x)^3}{48}\left(\frac{\partial^3\phi}{\partial x^3}\right)_P + H \tag{B.18}$$

The above expression indicates the QUICK scheme has a third order truncation error. However, the overall approximation will still be the second order accuracy when this scheme is used with midpoint rule approximation of surface intergral.

Navier-Stokes Equations Solver

This section presents the solution to the Navier-Stokes euqations with Re=1000. SIMPLE (Semi-Implicit Method for Pressure-Linked Equations) algorithm, developed by Spalding and Patankar (1972), is used for pressure-velocity coupling. The momentum interpolation presented by Rhie and Chow (1983) is employed for calculating the cell-face mass fluxes to avoid the pressure oscillation. The boundary condition of driven cavity system is shown in Figure B.1, Figure B.2 and Figure B.3 are the simulation results compared to the results presented by Ghia et al. (1982).

The solution procedures are summarized as followings.

1. Guess pressure field and flux.

2. Solve velocities on the basis of assumed pressure field and flux.

3. Calculate coefficients for pressure correlation and assemble coefficient matrix.

4. Solve the discretized pressure correlation equation.

5. Correct pressure, velocities and fluxes.

6. Calculate temperature field and update related properties.

7. Repeat steps 2-6.

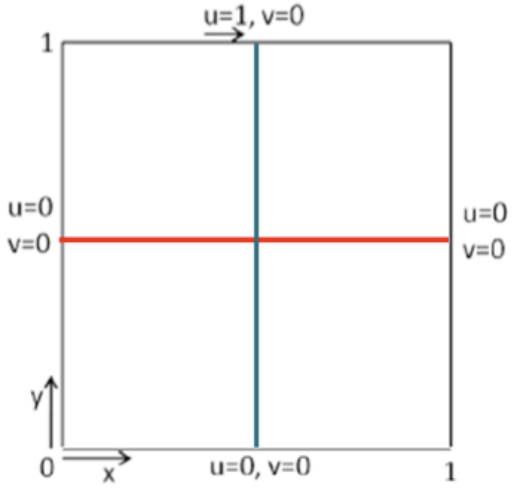

Figure B.1: Boundary condition of driven cavity system.

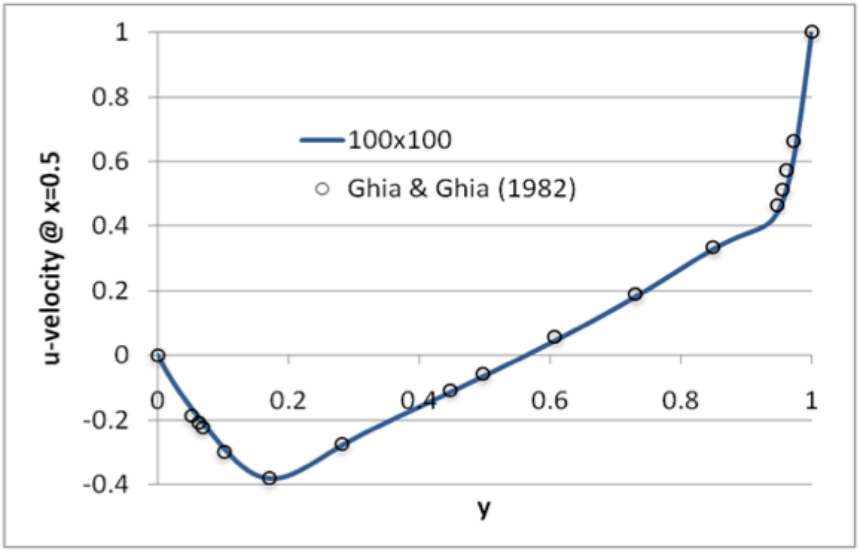

Figure B.2: U velocity profile at x=0.5.

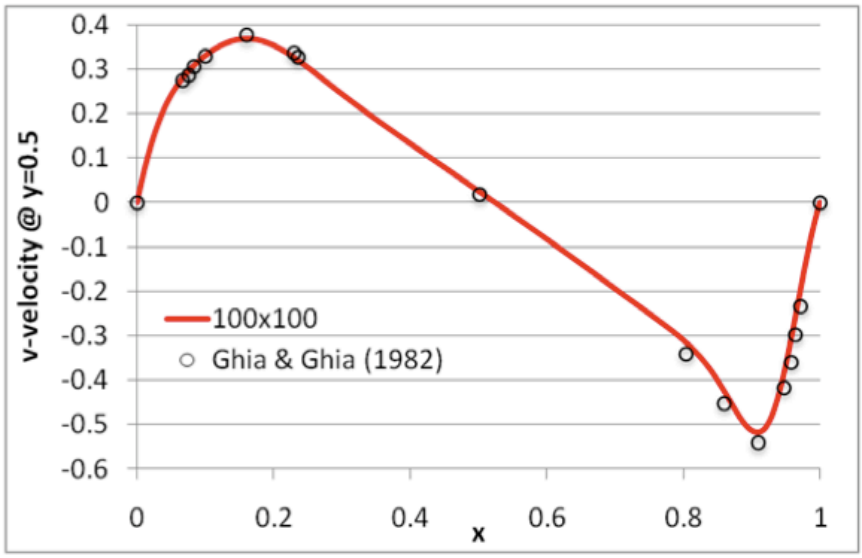

Figure B.3: V velocity profile at y=0.5.

The coupling of Navier-Stokes equations with porous media flow is defined as a further work.

Appendix C: User's Manual

Simulator Installation

The presented geothermal simulator is built based upon the Cactus framework which is designed for developing portable, modular applications. A Cactus code consists of a core part "Flesh" and a set of modules called "thorns". The Flesh works as a utility and service library providing thorns with information or action. In contrast, thorns are the modules containing different functionalities. Several steps can be follow to build up the geothermal simulator.

Getting the Code

One way to download Cactus is to use the "GetComponents" script which takes an argument the name of a file containing a ThornList. The script is available at:
https://raw.github.com/gridaphobe/CRL/ET_2011_10/GetComponents

Alternatively, svn is also applicable to check out Cactus. The main Cactus Subversion Server (svn.cactuscode.org) hosts several different repositories including different branches for the stable and development versions of Cactus. Check out the Cactus flesh:
svn co http://svn.cactuscode.org/flesh/trunk Cactus

Configuring

The purpose of configuration is to determine compilers and compilation ags suitable for the current architecture. The general command is shown as:
gmake <config name>-config <option name>=<chosen value> , ...

Since the presented geothermal simulator includes several external softwares (OpenMPI, HDF5, PETSc and ParMetis), the full configuration command using in this study is:

gmake thermal-config LIB=parmetis, HDF5=yes, MPI=OpenMPI, PETSC=yes

However, Cactus cannot setup or locate the installed external softwares. Before running configuration command, the softwares should be installed properly, and all the corresponding environmental variables (PATH, LD_LIBRARY_PATH, LIBDIRS, PETSC_DIR, HDF5_DIR, OPENMPI_DIR, PETSC_ARCH) have to be specified, for example
export PETSC_ARCH="linux-gnu-c".

Compiling

Once the new configuration ("thermal") has been successfully created, the corresponding executable can be built using following command:
gmake thernal SILENT=no
The default executable will be stored in the folder called "./exe" with the default name of "cactus_thermal". "SILENT=no" is a compilation option to make the compiler output more details during compiling.

Running

Cactus executables always run from a parameter le which species which thorns to use and sets the values of each thorns parameters. The command line used in this study is:
cactus_thermal thermal.par

The name of parameter file is "thermal.par", although there is no restriction on it. A parameter le is a text le whose lines are either comments (begin with '#' or '!') or parameter statements (parameter names followed by an '=', followed by the value for these parameters).

The first parameter statement in any parameter file is ActiveThorns, which is a special

parameter that tells the program which thorns are to be activated. And only parameters from active thorns can be set, since all thorns are set to be inactive by default.

Example: Saturated Geothermal Reservoirs

To run a case which can achieve the same result as shown in Figure 4.12, several thorns need to be checked out first and the thornlist is as follows.

CactusBase/Boundary

CactusBase/CartGrid3D

CactusBase/CoordBase

CactusBase/IOASCII

CactusBase/IOBasic

CactusBase/IOUtil

CactusBase/LocalInterp

CactusBase/LocalReduce

CactusBase/SymBase

CactusBase/Time

CactusConnect/HTTPD

CactusConnect/HTTPDExtra

CactusConnect/Socket

CactusExternal/FlexIO

CactusExternal/jpeg6b

CactusIO/IOJpeg

CactusPUGH/PUGH

CactusPUGH/PUGHInterp

CactusPUGH/PUGHReduce

CactusPUGH/PUGHSlab

CactusPUGHIO/IOHDF5

CactusPUGHIO/IOHDF5Util

CactusUtils/NaNChecker

CactusUtils/TimerReport

ResSim/BlackOilBase

ResSim/BlackOilEvolve

ResSim/GeoThermal

ResSim/IDBlackOil

ResSimExamples/GeoT

Sandbox/LocalToGlobal

where, BlackOilBase, IDBlackOil contain variable definitions and data initialization; BlackOilEvolve and Geothermal thorns solve mass and heat transport equations, respectively.

The parameter file is attached as follows to demonstrate how to setup the above problem.

ActiveThorns="geot localtoglobal coordbase cartgrid3d pugh blackoilbase blackoilevolve geothermal idblackoil boundary symbase timerreport ioascii iobasic ioutil pughslab iohdf5 iohdf5util httpd httpdextra socket iojpeg localreduce pughreduce Time"

cactus::terminate = "time"

cactus::cctk_final_time = 13000

cactus::cctk_timer_output = "full"

Time::timestep_method = "given"

Time::timestep = 5

driver::global_nx=57

driver::global_ny=57

driver::global_nz=37

driver::ghost_size=1

driver::padding_active = "no"

driver::enable_all_storage = ”yes”

domain size

grid::domain = ”full”

grid::type =”coordbase”

coordbase::xmin= 0

coordbase::xmax= 6679.3

coordbase::ymin= 0

coordbase::ymax= 6679.3

coordbase::zmin= 0

coordbase::zmax= 472.3

coordbase::ncells_x=56

coordbase::ncells_y=56

coordbase::ncells_z=36

coordbase::spacing=”numcells”

Above statements describe the simulation setting include simulation time, domain size, timestep, mesh generation and etc.

setting up IDblackoil parameters

idblackoil::InitializePressureFromOWC = ”no”

idblackoil::DefaultPorosity = 0.2

idblackoil::DefaultPermXX = 200

idblackoil::DefaultPermYY = 200

idblackoil::DefaultPermZZ = 200

idblackoil::DefaultPw = 13200

blackoilbase::DipAngleX=5

blackoilbase::DipAngleY=5

geothermal::TGrad=0.0154

geothermal::Tsur=275.6

geothermal::DHE_Length=2624

geothermal::DHE_Reinjection=3280

geothermal::DHE_I=44

geothermal::DHE_J=44

geothermal::DHE_K=25

geothermal::DHE_Projection_I=-0.706665

geothermal::DHE_Projection_J=-0.706665

geothermal::DHE_Projection_K=-0.035333

Geothermal reservoir properties are setup, including dip angle along x and y axis (DipAngleX and DipAngleY), thermal gradient (TGrad), temperature at top surface (Tsur). DHE configurations are also covered: length, reinjection distance, DHE starting point in reservoir (DHE_I, DHE_J, DHE_K), and direction vector along x, y, z (DHE_Projection_I, DHE_Projection_J, DHE_Projection_K).

setting up solver

BlackOilEvolve::absTol = 1e-8

BlackOilEvolve::relTol = 1e-9

BlackOilEvolve::imp_tolerance = 1e-8

BlackOilEvolve::max_imp_counter = 800

BlackOilEvolve::BlackOilStepKSPType = "bcgs"

BlackOilEvolve::BOPCType = "bjacobi"

Convergence tolerance, linear equation solver and preconditioner are specified as above.

setup output

IO::out_mode = "onefile"

IO::out_unchunked = "yes"

IO::out_dir = "Geothermal"

IOBASIC::outScalar_criterion = "iteration"

IOBasic::outInfo_every = 1

IOBasic::outInfo_vars = "BlackOilBase::Pw BlackOilBase::Tt"

iohdf5::out_every = 6

iohdf5::out_dir = "Geothermal"

iohdf5::out_vars = "blackoilbase::Pw blackoilbase::Tt"

Screen and HDF5 output options are selected.

Vita

Yin Feng was born in December, 1981, in Daqing, Heilongjiang, China. He finished his undergraduate studies at Dalian University of Technology, Dalian, in June 2004. He earned a master of science degree in petroleum engineering from the University of Louisiana at Lafayette in December 2007. He is currently a candidate for the degree of Doctor of Philosophy in petroleum engineering, to be awarded in August 2012.